

CONVECTIVE INSTABILITY IN ANNULAR SYSTEMS

By

DARREN MCDUFF

A DISSERTATION PRESENTED TO THE GRADUATE SCHOOL  
OF THE UNIVERSITY OF FLORIDA IN PARTIAL FULFILLMENT  
OF THE REQUIREMENTS FOR THE DEGREE OF  
DOCTOR OF PHILOSOPHY

UNIVERSITY OF FLORIDA

2006

Copyright © 2006

By

Darren McDuff

## ACKNOWLEDGMENTS

I begin by thanking my advisor, Dr. Ranga Narayanan, whose great ideas, support, and motivation have guided me through this work.

I thank my mom, dad, and sister. They have always been the best of friends to me and been there for me during any difficult times in my life. On the subject of family, I should point out here that I first considered the idea of graduate school as a result of my dad suggesting it.

I am also grateful to those on my advisory board. These include Dr. Martin Volz, Dr. James Klausner, Dr. Dmitry Kopelevich, and Dr. Mark Orazem. Their different viewpoints and ideas about my research have helped me to improve my work and avoid potential mistakes. Dr. Volz is my mentor in the N.A.S.A. Graduate Student Researchers Program, and traveled from Marshall Space Flight Center in Huntsville, Alabama, to be here for my presentations. Dr. Klausner comes from the Department of Mechanical and Aerospace Engineering at this university. Dr. Kopelevich and Dr. Orazem are from my own department.

I must express my gratitude to Ken Reed. Ken is a talented machinist with T.M.R. Engineering. High-quality components made by T.M.R. were essential to the design of my experimental apparatus, and it was great to work with someone as helpful, knowledgeable, and professional as Ken throughout the project.

Additionally, I thank Gérard Labrosse, a professor from L.I.M.S.I. in Orsay, France. During visits with our research group here at the University of Florida, he has spent a great deal of time sharing his knowledge on computational fluid dynamics (in particular, spectral methods) and providing helpful answers to questions from my research group.

I would also like to thank a couple of undergraduates who have worked with me on this project, particularly in the design of my experimental apparatus and the process control program

for it. Joe Cianfrone helped me to understand the computer software, LabVIEW™, and with that software, we designed a very effective process control program for my experiment. Joe also helped me to design a large electrical circuit to send data from my experiment into a process control computer, and send process control signals from that computer to components of my experiment. Scott Suozzo helped me with the design and re-design of several parts of my experimental apparatus, which helped the experiment to run well enough to produce results that match theoretical predictions.

Of course, I thank my research group and the other graduate students in this department whose advice and ideas have helped me get past difficult parts of my project and helped me in my on-going education in this field. In particular, I thank Dr. Weidong Guo, of my research group, for spending a good deal of time discussing computational issues with me during the last couple of years.

Lastly, I am deeply grateful to N.A.S.A. for supporting this work through a fellowship from the N.A.S.A. Graduate Student Researchers Program (grant number NGT852941).

## TABLE OF CONTENTS

ACKNOWLEDGMENTS.....	3
LIST OF TABLES.....	8
LIST OF FIGURES.....	9
LIST OF ABBREVIATIONS AND SYMBOLS.....	13
ABSTRACT.....	16
CHAPTER	
1 INTRODUCTION.....	18
1.1 Physics of Convection.....	18
1.1.1 Rayleigh Convection.....	19
1.1.2 Marangoni Convection.....	21
1.2 Rayleigh Number.....	24
1.3 Physical Explanation: Pattern Selection.....	25
1.3.1 Laterally Unbounded System.....	25
1.3.2 Rectangular System, Laterally Bounded, Periodic Lateral Boundary Conditions.....	28
1.3.3 Rectangular System, Laterally Bounded, Non-Periodic Lateral Boundary Conditions.....	31
1.3.4 Cylindrical System.....	33
1.3.5 Annular System.....	36
1.4 Annulus vs. Cylinder.....	37
1.5 Application.....	40
2 LITERATURE REVIEW.....	50
2.1 Single Fluid Layers.....	50
2.2 Multiple Fluid Layers.....	56
3 MODELING EQUATIONS.....	61
3.1 Nonlinear Equations.....	61
3.2 Scaling.....	66
4 LINEARIZED EQUATIONS.....	70
4.1 Linearization.....	70
4.2 Expansion into Normal Modes.....	75

5	SPECTRAL SOLUTION METHOD.....	80
5.1	Explanation of the Method.....	82
5.2	Application of the Method.....	89
6	EXPERIMENTAL DESIGN.....	98
6.1	Goals in Experimental Design.....	98
6.2	Experimental Apparatus.....	98
6.2.1	Test Section.....	99
6.2.2	Bottom Temperature Bath.....	101
6.2.3	Top Temperature Bath.....	102
6.2.4	Insulation.....	103
6.2.5	Flow Visualization.....	103
6.3	Process Control System.....	104
6.4	Typical Experimental Procedure.....	106
7	RESULTS AND DISCUSSION.....	111
7.1	Cylindrical Systems.....	111
7.1.1	Constant Viscosity Computations: Cylinder.....	111
7.1.2	Non-Constant Viscosity Computations: Cylinder.....	113
7.1.3	Experiments: Cylinder.....	114
7.1.4	Comparison of Results: Cylinder.....	115
7.2	Annular Systems.....	116
7.2.1	Constant Viscosity Computations: Annulus.....	117
7.2.2	Non-Constant Viscosity Computations: Annulus.....	121
7.2.3	Experiments: Annulus.....	121
7.2.4	Comparison of Results: Annulus.....	122
7.3	Error Analysis.....	125
8	CONCLUSIONS AND POSSIBLE FUTURE STUDIES.....	159
8.1	Summary.....	159
8.2	Future Studies.....	161
APPENDIX		
A	THERMOPHYSICAL PROPERTIES.....	163
B	ADDITIONAL EXPLANATION OF EQUATIONS.....	165
B.1	Boussinesq Approximation.....	165
B.2	Nonlinearities in the Governing Equations.....	166
B.3	Characteristic Velocity and Characteristic Time.....	167

C	DEVELOPMENT OF MATHEMATICAL MODEL FOR THE CONSTANT VISCOSITY CASE.....	168
	C.1 Nonlinear Equations.....	168
	C.2 Scaling.....	170
	C.3 Linearization.....	172
	C.4 Expansion into Normal Modes.....	174
D	MATLAB <sup>®</sup> PROGRAM GENERAL FLOW-DIAGRAM.....	177
E	EXAMPLE MATLAB <sup>®</sup> PROGRAMS.....	178
	E.1 Physical Properties.....	178
	E.2 Depths for Annular System.....	179
	E.3 Main Program: Annular System with Temperature-Dependent Viscosity.....	179
F	LABVIEW <sup>™</sup> PROGRAM GENERAL FLOW-DIAGRAM.....	191
	REFERENCES.....	192
	BIOGRAPHICAL SKETCH.....	194

## LIST OF TABLES

<u>Table</u>	<u>Page</u>
5-1	Example of convergence of computed result with $N_r$ and $N_z$ ..... 94
5-2	Comparison of rectangular, 2-D, no-stress results with rectangular 1-D results..... 94
5-3	Comparison of calculated cylindrical results with results of Hardin et al..... 94
7-1	Constant viscosity computational results: critical temperature difference and onset flow pattern for sets of cylindrical dimensions considered in experiments..... 129
7-2	Non-constant viscosity computational results: critical temperature difference and onset flow pattern for sets of cylindrical dimensions considered in experiments..... 129
7-3	Experimental results: critical temperature difference and onset flow pattern for sets of cylindrical dimensions..... 129
7-4	Summary of computational and experimental results for cylindrical systems..... 130
7-5	Constant viscosity computational results: critical temperature difference and onset flow pattern for sets of annular dimensions considered in experiments..... 130
7-6	Non-constant viscosity computational results: critical temperature difference and onset flow pattern for sets of annular dimensions considered in experiments..... 130
7-7	Experimental results: critical temperature difference and onset flow pattern for sets of annular dimensions..... 131
7-8	Summary of computational and experimental results for annular systems..... 131
A-1	Thermophysical properties..... 164

## LIST OF FIGURES

<u>Figure</u>	<u>Page</u>
1-1 Simplified system diagram: heated from below.....	43
1-2 Rayleigh convection.....	43
1-3 Marangoni convection.....	44
1-4 General diagram: critical Rayleigh number vs. disturbance wavelength.....	44
1-5 Cross-sectional velocity profiles of flow patterns with different numbers of convective rolls.....	45
1-6 General stability diagram for buoyancy-driven convection in a rectangular, laterally bounded system, with periodic boundary conditions at lateral walls, for varying aspect ratio.....	45
1-7 Cross-sectional velocity profiles of four-roll flow patterns with non-uniform roll size...46	46
1-8 General stability diagram for buoyancy-driven convection in a rectangular, laterally bounded system, with non-periodic boundary conditions at lateral walls, for varying aspect ratio.....	46
1-9 Diagrams of $m = 0, 1, 2, 3$ flow patterns: “U”: upward flow, “D”: downward flow... 47	47
1-10 General stability diagram for buoyancy-driven convection in a cylindrical container, for varying aspect ratio.....	48
1-11 Convective flow pattern in an annulus (Stork & Müller 1974).....	48
1-12 Example: computed flow profile for annular system, cross-sectional view.....	49
1-13 Diagram of crystal growth system.....	49
3-1 System diagram: cylindrical and annular systems.....	69
5-1 Discretization nodes in a cylinder.....	95
5-2 Example: grid point spacing.....	95
5-3 Diagram of matrix/vector arrangement of discretized problem.....	96
5-4 Examples of flow patterns and parenthetical notation for cylindrical systems.....	97

6-1	Simple experiment diagram.....	108
6-2	Photograph of experimental apparatus.....	108
6-3	Photograph of flow-through top water bath of experimental apparatus.....	109
6-4	Cross-sectional diagram of test section.....	109
6-5	Process control system layout.....	110
7-1	Constant viscosity computational results: $Ra_{crit}$ vs. $A$ for cylindrical systems.....	132
7-2	Constant viscosity computational results: $Ra_{crit}$ vs. $A$ for cylindrical systems, close-up view.....	133
7-3	Computed velocity profile, cross-sectional view, $L_z = 6.85$ mm, $L_r = 8.75$ mm, $m = 0:(0,2)$ , $[\Delta T]_{crit} = 5.80$ °C.....	134
7-4	Computed velocity profile, cross-sectional View, $L_z = 7.18$ mm, $L_r = 11.51$ mm, $m = 1:(1,3)$ , $[\Delta T]_{crit} = 5.04$ °C.....	135
7-5	Computed velocity profile, cross-sectional view, $L_z = 6.53$ mm, $L_r = 11.28$ mm, $m = 1:(1,3)$ , $[\Delta T]_{crit} = 6.43$ °C.....	136
7-6	Photo of onset flow pattern, $L_z = 6.85$ mm, $L_r = 8.75$ mm, $m = 0:(0,2)$ .....	136
7-7	Photo of onset flow pattern, $L_z = 7.18$ mm, $L_r = 11.51$ mm, $m = 1:(1,3)$ .....	137
7-8	Photo of onset flow pattern, $L_z = 6.53$ mm, $L_r = 11.28$ mm, $m = 1:(1,3)$ .....	137
7-9	Constant viscosity computational results: $Ra_{crit}$ vs. $S$ for annular systems with $A = .75$ .....	138
7-10	Constant viscosity computational results: $Ra_{crit}$ vs. $S$ for annular systems with $A = 1.28$ .....	139
7-11	Constant viscosity computational results: $Ra_{crit}$ vs. $S$ for annular systems with $A = 1.28$ , close-up view.....	140
7-12	Constant viscosity computational results: $Ra_{crit}$ vs. $S$ for annular systems with $A = 1.60$ .....	141
7-13	Constant viscosity computational results: $Ra_{crit}$ vs. $S$ for annular systems with $A = 1.60$ , close-up view.....	142

7-14	Constant viscosity computational results: $Ra_{crit}$ vs. $S$ for annular systems with $A = 1.73$ .....	143
7-15	Constant viscosity computational results: $Ra_{crit}$ vs. $S$ for annular systems with $A = 1.73$ , close-up view.....	144
7-16	Constant viscosity computational results: $Ra_{crit}$ vs. $S$ for annular systems with $A = 2.90$ .....	145
7-17	Constant viscosity computational results: $Ra_{crit}$ vs. $S$ for annular systems with $A = 2.90$ , close-up view.....	146
7-18	Constant viscosity computational results: $Ra_{crit}$ vs. $S$ for annular systems with $A = 3.40$ .....	147
7-19	Constant viscosity computational results: $Ra_{crit}$ vs. $S$ for annular systems with $A = 3.40$ , close-up view 1.....	148
7-20	Constant viscosity computational results: $Ra_{crit}$ vs. $S$ for annular systems with $A = 3.40$ , close-up view 2.....	149
7-21	Computed velocity profile, cross-sectional view, $L_z = 6.85$ mm, $R_o = 8.75$ mm, $S = .16$ , $m = 0:(0,1)$ , $[\Delta T]_{crit} = 7.08$ °C.....	150
7-22	Computed velocity profile, cross-sectional view, $L_z = 6.85$ mm, $R_o = 8.75$ mm, $S = .30$ , $m = 3:(3,0)$ , $[\Delta T]_{crit} = 7.67$ °C.....	151
7-23	Computed velocity profile, cross-sectional view, $L_z = 7.18$ mm, $R_o = 11.51$ mm, $S = .12$ , $m = 0:(0,1)$ , $[\Delta T]_{crit} = 5.57$ °C.....	152
7-24	Computed velocity profile, cross-sectional view, $L_z = 7.18$ mm, $R_o = 11.51$ mm, $S = .50$ , $m = 4:(4,0)$ , $[\Delta T]_{crit} = 7.09$ °C.....	153
7-25	Computed velocity profile, cross-sectional view, $L_z = 6.53$ mm, $R_o = 11.28$ mm, $S = .10$ , $m = 2:(2,1)$ , $[\Delta T]_{crit} = 7.21$ °C.....	154
7-26	Computed velocity profile, cross-sectional view, $L_z = 6.53$ mm, $R_o = 11.28$ mm, $S = .40$ , $m = 4:(4,0)$ , $[\Delta T]_{crit} = 8.07$ °C.....	155
7-27	Photo of onset flow pattern, $L_z = 6.85$ mm, $R_o = 8.75$ mm, $S = .16$ , $m = 0:(0,1)$ .....	155
7-28	Photo of onset flow pattern, $L_z = 6.85$ mm, $R_o = 8.75$ mm, $S = .30$ , $m = 3:(3,0)$ .....	156
7-29	Photo of onset flow pattern, $L_z = 7.18$ mm, $R_o = 11.51$ mm, $S = .12$ , $m = 2:(2,1)$ .....	156
7-30	Photo of onset flow pattern, $L_z = 7.18$ mm, $R_o = 11.51$ mm, $S = .50$ , $m = 4:(4,0)$ .....	157

7-31	Photo of onset flow pattern, $L_z = 6.53$ mm, $R_o = 11.28$ mm, $S = .10$ , $m = 2:(2,1)$ .....	157
7-32	Photo of onset flow pattern, $L_z = 6.53$ mm, $R_o = 11.28$ mm, $S = .40$ , $m = 4:(4,0)$ .....	158
D-1	MATLAB <sup>®</sup> program general flow-diagram.....	177
F-1	LabVIEW <sup>™</sup> program general flow-diagram.....	191

## LIST OF ABBREVIATIONS AND SYMBOLS

$\alpha$	volumetric thermal expansion coefficient ( $^{\circ}\text{C}^{-1}$ )
$\bar{\delta}_z$	unit vector in z-direction
$\varepsilon$	amplitude of small perturbation
$\kappa$	thermal diffusivity ( $\text{m}^2/\text{s}$ )
$\lambda$	eigenvalue of the eigenvalue form of the problem shown in Chapter 5
$\mu$	dynamic viscosity ( $\text{kg}/(\text{m}^*\text{s})$ )
$\mu_R$	reference dynamic viscosity ( $\text{kg}/(\text{m}^*\text{s})$ )
$\nu$	kinematic viscosity ( $\text{m}^2/\text{s}$ )
$\rho$	density ( $\text{kg}/\text{m}^3$ )
$\rho_R$	reference density ( $\text{kg}/\text{m}^3$ )
$\sigma$	dimensionless inverse time constant
$\tau$	transpose symbol for a matrix
$\psi$	form of the x-direction dependence in a laterally bounded, rectangular system with periodic lateral boundary conditions
$\Omega$	dimensionless group which appears in the motion equation when considering the dependence of viscosity on temperature
$A$	aspect ratio for cylindrical and annular systems
$A_{xz}$	aspect ratio for rectangular systems
$\bar{A}$	left-hand-side matrix of the eigenvalue form of the problem shown in Chapter 5
$B$	a constant related to the dependence of viscosity on temperature ( $^{\circ}\text{C}^{-1}$ )
$\bar{B}$	right-hand-side matrix of the eigenvalue form of the problem shown in Chapter 5
$C_p$	constant-pressure heat capacity ( $\text{J}/(\text{kg}^*\text{^{\circ}\text{C}})$ )

$C_V$	constant-volume heat capacity (J/(kg*°C))
$D$	differentiation matrix
$f$	function representing the temperature dependence of viscosity
$F$	function representing the temperature dependence of viscosity, in terms of dimensionless temperature
$g$	magnitude of gravity (m/s <sup>2</sup> )
$\bar{g}$	gravity, in vector form (m/s <sup>2</sup> )
$k$	thermal conductivity (W/(m*°C))
L.I.M.S.I.	Laboratoire d'Informatique pour la Mécanique et les Sciences de l'Ingénieur
$L_r$	radius in a cylindrical system, or annular gap width in an annular system (m)
$L_x$	horizontal depth of fluid layer (m)
$L_z$	vertical depth of fluid layer (m)
$m$	azimuthal wave number
$N_{Pr}$	Prandtl number
$N_r$	parameter setting the number of discretization nodes in the r-direction
$N_x$	parameter setting the number of discretization nodes in the x-direction
$N_z$	parameter setting the number of discretization nodes in the z-direction
N.A.S.A.	National Aeronautics and Space Administration
$p$	modified pressure (Pa)
$\bar{p}$	characteristic pressure (Pa)
$P$	pressure (Pa)
$Ra$	Rayleigh number
$Ra_{crit}$	critical Rayleigh number
$R_o$	outer radius of annular system

$R_i$	inner radius of annular system
$S$	radius ratio for annular system
$\bar{\bar{S}}$	stress tensor
$t$	time (s)
$\bar{t}$	characteristic time (s)
$t_{el}$	time elapsed (s) (Appendix F)
$t_{seg,T}$	time segment that each $T_b$ set-point remains in effect for (s) (Appendix F)
$t_{seg,VCR}$	time interval between repetitions of the video cassette recorder's recording cycle (s) (Appendix F)
$T$	temperature ( $^{\circ}\text{C}$ )
$T_b$	temperature at bottom wall of system ( $^{\circ}\text{C}$ )
$T_{b,sp}$	set-point value for $T_b$ ( $^{\circ}\text{C}$ ) (Appendix F)
$T_{b,sp,j}$	for $j = (1, 2, 3, \dots)$ , series of set-point values input for $T_b$ ( $^{\circ}\text{C}$ ) (Appendix F)
$T_R$	reference temperature ( $^{\circ}\text{C}$ )
$T_t$	temperature at top wall of system ( $^{\circ}\text{C}$ )
$\Delta T$	vertical temperature difference in fluid layer ( $^{\circ}\text{C}$ )
$[\Delta T]_{crit}$	critical vertical temperature difference for convection ( $^{\circ}\text{C}$ )
$[\Delta T]_{guess}$	guess-value for critical vertical temperature difference for convection ( $^{\circ}\text{C}$ )
$v_j$	component of velocity in the $j$ -direction
$\bar{v}$	velocity (m/s)
$\bar{v}$	characteristic velocity (m/s)
$\bar{X}$	eigenvector of the eigenvalue form of the problem shown in Chapter 5

Abstract of Dissertation Presented to the Graduate School  
of the University of Florida in Partial Fulfillment of the  
Requirements for the Degree of Doctor of Philosophy

## CONVECTIVE INSTABILITY IN ANNULAR SYSTEMS

By

Darren McDuff

December 2006

Chair: Ranga Narayanan  
Major Department: Chemical Engineering

Since natural convection can occur in such a wide range of systems and circumstances, much remains to be learned about the convective behaviors that appear in some systems. For example, convection in fluid layers of shapes other than cylinders or rectangles can be quite interesting, and it is this which is investigated in this research.

This study focuses on Rayleigh convection, which is natural convection caused by buoyancy forces. The convective behavior of a system (referring to a fluid layer as the “system”) depends upon the shape and dimensions of the system, the vertical temperature difference across the system, the thermophysical properties of the fluid comprising the system, and the characteristics of the disturbance given to the system. In particular, this research is concerned with the effects of the size and shape of the system.

One important application of this study is in semi-conductor crystal growth processes, such as the vertical Bridgman growth method. This growth method is commonly used, for example, in growing the semi-conductor crystal, lead-tin-telluride. Crystal growth is usually thought of as a process in a cylindrical container. It is of interest to learn how the convective behavior of the system would differ if annular fluid layers were employed.

The onset conditions for buoyancy-driven convection (critical vertical temperature difference and flow pattern) in bounded, vertical, cylindrical systems and vertical, annular systems were determined both experimentally and theoretically. In the experiments, onset conditions were determined by flow visualization with tracer particles. The theoretical analysis involves bifurcation theory and computations using spectral methods.

Computations show that the physics of the annular system are similar to those of the cylindrical system. More rolls of convecting fluid are included as the container is widened, and rolls may exist with either an azimuthal or radial alignment. The relations between the annular container dimensions and the onset conditions for convection are determined and shown. The agreement between computations and experiments is generally good. Some discrepancy in this agreement arises in cases in which the annular gap width is small, and a likely reason for this is explained.

## CHAPTER 1 INTRODUCTION

This chapter provides an introduction to the physics of the convective phenomena investigated in this research. It then proceeds to a brief explanation of the dimensionless Rayleigh number which is very meaningful in regard to buoyancy-driven convection. After this, an explanation is given regarding the competing physical phenomena which determine the number of convective cells that appear at the onset of convection and their sizes. Next, an explanation of why it is interesting to study the behavior of an annular system as compared to a cylindrical one is given. Lastly, an example of an industrial application to which this study has relevance is discussed.

### **1.1 Physics of Convection**

Many types of convective flows are possible, and many of them have been well studied. Convection can be classified as either forced or natural. In forced convection, flow is caused by external means. Flow of a liquid being pumped across a flat plate, for example, is forced convection. The flow that will be considered in this study, however, is of the other variety. Natural convection is convection in which flows are caused by forces that interact with thermophysical property variations. For example, natural convection in a system can be caused by buoyancy, interfacial tension gradients, or a combination of the two. When buoyancy is the cause of flow, this is called Rayleigh convection; if interfacial tension gradients cause flow, this is called Marangoni convection.

If a system (here, “system” refers to a fluid layer) is going to convect, then the temperature difference corresponding to the onset of convection is determined by the direction from which the system is heated, the shape and dimensions of the system, the thermophysical properties of the fluid, and the characteristics of the disturbance given to the system. Regarding

these factors, it is noteworthy that the fluid's thermophysical properties themselves may change significantly across the fluid layer depending on the magnitude of the vertical temperature difference to which fluid layer is subjected. This research focuses on the effects of the shape and dimensions of the system on convective behavior. Unless otherwise noted, the heating of the system referred to is uniform on the top and bottom surfaces. Also, for the physical explanations that follow, until otherwise noted, the systems discussed may be assumed unbounded in the lateral direction.

### **1.1.1 Rayleigh Convection**

A system capable of convection, in general, could be heated from below or above and include any number of liquid and vapor phases. For a physical explanation of Rayleigh convection, though, all that need be considered is a single layer of fluid, unbounded in the horizontal direction, heated from below, with the top and bottom walls held at constant temperatures. Understanding the origin of convection in this system will be sufficient to predict what is likely to happen in more complex systems. More importantly, a single fluid layer, heated from below, is precisely the system examined in this research.

Generally, the density of a fluid decreases as temperature is increased. This means that the density at the top of the fluid would be higher than that at the bottom of the phase. Consider a z-axis along the vertical direction in the fluid layer, with the top surface at  $z = L_z$ , and the bottom surface at  $z = 0$ . This simple system is shown as Figure 1-1.

This top-heavy fluid layer is potentially unstable to gravity (shown in many figures as  $\bar{g}$ ) if subjected to a perturbation. If a particular disturbance to the system causes an element of fluid near the top of the layer to be displaced downward, then it will have a tendency to continue moving downward toward its gravitationally appropriate resting place. As this element of fluid

moves downward, it displaces the lighter fluid surrounding it upward due to mass conservation. The downward-moving fluid elements are heated once they reach the bottom of the system, and the upward-moving fluid elements are cooled once they reach the top of the system, and so the process repeats. This process results in rolls of circulating fluid, or convective “cells,” that form cellular flow patterns. Since the lowest density in the phase is at the bottom, a fluid element displaced downward would continue to move downward to  $z = 0$  if its motion were not resisted in any way. Flow is resisted, however, by the dynamic viscosity of the fluid. Additionally, if the kinematic viscosity and thermal diffusivity of the fluid are sufficiently high, then the mechanical and thermal perturbations may quickly die out. It is when the vertical temperature difference across the system is increased beyond a certain critical value that this convection–Rayleigh convection–will occur; at that point, gravitational instability overcomes the damping effects of kinematic viscosity and thermal diffusivity. Rayleigh convection is stronger in a phase with lower kinematic viscosity and lower thermal diffusivity; this is because mechanical and thermal disturbances are damped out less quickly in a phase having lower values for those properties. Now, it might appear that Rayleigh convection results simply from large enough vertical temperature gradients. In truth, however, even with a sufficiently large vertical temperature gradient present, Rayleigh convection can begin only if disturbances with transverse (horizontal) variation are imposed on the system. A fluid element displaced by a disturbance must “feel” a relative difference in the density of the fluid horizontally neighboring it, and this can occur only as a result of disturbances with transverse variation. Note that the disturbance which causes the onset of convection need not necessarily be a mechanical one. A thermal disturbance with transverse variation could just as easily cause convection to begin by making a certain fluid

element warmer or cooler than the fluid horizontally adjacent to it. Figure 1-2 shows a buoyancy-driven convective flow pattern occurring in a fluid phase.

### **1.1.2 Marangoni Convection**

Convection can occur in another way, as well. The flow can be driven by interfacial tension gradients rather than buoyancy forces. This type of flow is called Marangoni convection. Since Marangoni convection is driven by gradients in interfacial tension, it is a phenomenon that can occur only in systems possessing multiple fluid phases which contact each other at interfaces. This research is concerned with the simpler case of a single fluid layer confined in all directions by solid walls. Thus, Marangoni convection could not occur in the system being researched. Still, a brief explanation of Marangoni convection will now be given for the sake of giving a more complete explanation of the physics of convection.

To this end, consider a system of two vertically stacked fluids, in which one vertical boundary is heated so as to subject the system to a vertical temperature gradient. Again, assume the system is unbounded in the horizontal direction. In this hypothetical system, both the top and bottom walls are kept at constant temperatures and Marangoni convection can occur in this system regardless of which vertical boundary of the system is warmer. For the sake of making an explanation by example, assume that the bottom wall of the system is warmer than the top. Like Rayleigh convection, Marangoni convection results from perturbations with transverse variation. If the interface between the fluids is perturbed, then some interfacial regions could be pushed upward and some downward. This gives rise to a transverse temperature gradient along the interface. Consider an interfacial region pushed upward. The fact that the system is heated from below means that this region now experiences a lower temperature than the regions of the interface adjacent to it. Typically, surface tension, like density, increases with decreasing

temperature. Thus, the interfacial region that has been pushed upward has an increased interfacial tension and pulls fluid at the interface toward it. When this happens, fluid from the bulk phases must move in to replace fluid being pulled away from regions of the interface that lowered in interfacial tension (when the system is heated from below, these regions are the troughs of the wavy interface). The flow patterns in Marangoni convection, like those in Rayleigh convection, are cellular. Since the interfacial tension gradients are generated by temperature differences along the interface, a higher vertical temperature difference across the system favors Marangoni convection. Figure 1-3 is a simple illustration of Marangoni convection.

The replacement fluid arriving from the bulk phases is warm in the case of the lower fluid, and cool in the case of the upper fluid; this supply of replacement fluids can either strengthen or weaken the temperature gradient which fuels Marangoni convection. The effect that the fluid moving to the hot regions of the interface from the bulk phases has on this temperature gradient is dependent upon the amount of fluid from each phase that arrives at those locations and on the thermophysical properties of each phase.

As with Rayleigh convection, dynamic viscosity resists flow and can damp the process. Marangoni convection, like Rayleigh convection, is stronger in a phase with lower kinematic viscosity and lower thermal diffusivity because a phase having lower values for those properties damps out disturbances less quickly. On the other hand, if these two properties have high enough values, a disturbance at the interface will die out rather than amplify to cause convection. Of course, the phase with a lower kinematic viscosity is not necessarily the phase that has a lower thermal diffusivity. Thus, the combination of these two properties determines which phase will convect more strongly. The phase which has a kinematic viscosity-thermal diffusivity

combination more favorable to convection is the phase from which it will be easiest for fluid to move in and replace that which is lost at hot interfacial regions during Marangoni convection; it is primarily from this phase that fluid is supplied to the hot regions of the interface. If this more strongly convecting phase is the warmer phase, then the fluid it supplies to the hot interfacial regions is even warmer than what was originally present, and Marangoni convection is reinforced. In the opposite scenario, cold fluid moves in to the hot regions of the interface; this cools those regions down and counteracts Marangoni convection. In the case where system of two stacked fluids is comprised of a vapor-liquid bilayer, rather than a liquid-liquid bilayer, it should be noted that a liquid can generally transport more heat by convection than can a vapor. This is quantitatively shown when a comparison is made between the product of density and heat capacity ( $\rho * C_p$ ) for liquids and vapors. Though the thermal conductivities of vapors and liquids may differ, this difference may be considered less significant. The reason for this is that the fluids are already conducting heat in the motionless initial state of the system (base state). While the effect of the difference in density multiplied by heat capacity becomes important once convection begins, the effect of the difference in thermal conductivity is relatively unchanged. By this line of reasoning, replacement fluid arriving to troughs on the interface from the liquid phase of a vapor-liquid bilayer system is likely to have more of an effect on the temperature gradient along the interface than replacement fluid arriving from the vapor phase of the bilayer. The same reasoning (involving the product of density and heat capacity) also can be used in deciding which fluid will more strongly affect the interfacial temperature gradient in a liquid-liquid bilayer system.

It is also very interesting to note that Marangoni convection can occur in the system even if the interface remains flat. If a non-mechanical, thermal perturbation is given to the interface,

then some regions become hot and some cold. Fluid from the hot regions is pulled toward the cold regions by interfacial tension, and fluid at the cold regions is displaced. As this happens, fluid from the bulk must move in to replace that lost at the hot interfacial regions – this marks the start of convection.

## 1.2 Rayleigh Number

The focus of this explanation will get back on its main course and address Rayleigh convection once again. Scaling of the equations that model a fluid layer heated from below leads to the following definition of the dimensionless Rayleigh number, which is shown as Equation 1.1. The Rayleigh ( $Ra$ ) number is a quantity that relates the factors determining whether or not buoyancy-driven convection occurs.

$$Ra = \frac{\alpha * g * L_z^3 * \Delta T}{\nu * \kappa} \quad (1.1)$$

The length scale associated with Rayleigh convection is the vertical phase depth, shown as  $L_z$ . In this definition,  $\alpha$  is a volumetric thermal expansion coefficient,  $g$  is the magnitude of gravity,  $\Delta T$  is the vertical temperature difference across the layer,  $\nu$  is the kinematic viscosity of the fluid, and  $\kappa$  is the thermal diffusivity of the fluid (which is equal to the thermal conductivity divided by the product of the density and heat capacity).

A higher Rayleigh number corresponds to a system that is more susceptible to buoyancy-driven convection. Notice that the factors which favor buoyancy-driven convection are all grouped in the numerator, while those which oppose the flow form the denominator. The thermal expansion coefficient represents the degree to which the density of the fluid changes when it is heated, so of course a higher value for this works in the favor of convection. Gravity and the vertical temperature difference are the most obvious of the two components needed to drive Rayleigh convection. A larger vertical temperature difference makes the system more

unstable to Rayleigh convection. Having a larger vertical phase depth means that the fluid feels a weaker effect from the no-slip conditions at the top and bottom walls, and thus is less mechanically constricted, and can more easily flow in a convective pattern. This effect is quite strong, and accordingly, the Rayleigh number is proportional to the vertical phase depth raised to the third power. Kinematic viscosity and thermal diffusivity act to dissipate any disturbances given to the system and prevent convection. Thus, these two thermophysical properties are located together in the denominator of the Rayleigh number.

### **1.3 Physical Explanation: Pattern Selection**

Some of the most interesting facets of the convective behavior studied in this research relate to the competition of certain physical phenomena to determine precisely which convective flow patterns arise at the onset of convection.

#### **1.3.1 Laterally Unbounded System**

Imagine, once again, the system shown in Figure 1-1. The system is constantly subjected to small mechanical and thermal disturbances. As mentioned earlier, only disturbances with transverse variation can cause the onset of convection. The disturbances that the system receives are of an extremely large range of wavelengths, especially considering the case in which the system is laterally unbounded. Still, only one of these many disturbances actually causes the onset of convection. It is this disturbance to which the system is most unstable. It is the wavelength of this disturbance which determines the wavelength of the onset convective flow pattern. It is interesting to ask what makes disturbance of one wavelength more stabilizing or destabilizing to the system than another.

For the moment, consider two possibilities in terms of the wavelength of a periodic, wave-shaped disturbance. One possibility is that the disturbance is of very short wavelength,

meaning that it is quite jagged and choppy in appearance. The second possibility is that the disturbance is of very long wavelength, and so it is very gently, gradually sloping, with its minimum-points and maximum-points spread far apart from one another. The disturbance of very short wavelength possesses a great deal of transverse variation, since it repeats its lateral oscillations so frequently; this high degree of transverse variation favors convection. However, since the adjacent peaks and troughs of the wave-shaped disturbance are so close to one another, they easily diffuse their momentum and thermal energy into the horizontally neighboring fluid, which dissipates the disturbance and stabilizes the system to convection. For example, a fluid element which initially was heated and lowered in density relative to the fluid laterally adjacent to it, as a result of a disturbance of very short wavelength, would quickly match the density of the laterally adjacent fluid due to rapid diffusion of heat from the fluid element. Thus, insofar as diffusion of heat and momentum is concerned, the system is quite stable to disturbances which are of very short wavelength. The system reacts to a disturbance of very long wavelength a bit differently. A disturbance of very long wavelength is so laterally spread out that the sort of rapid diffusive stabilization just described does not play a role. Consequently, the lateral density differences generated by a disturbance of very long wavelength remain present rather than dissipating into uniformity, which is a condition that favors buoyancy-driven convection. However, when the disturbance is of very long wavelength, the adjacent peaks and troughs of the wave-shaped disturbance are so far apart from one another that the local density differences between adjacent fluid elements (the transverse variations which are needed to drive buoyancy-driven convection) are too weak to cause and sustain buoyancy-driven convection. If a disturbance of very long wavelength were able to form a corresponding cellular, convective flow pattern of a very long wavelength, the flow pattern would not be able to be sustained; this is

because it would simply require too much energy to drive the fluid in the convective cells across the very long, nearly horizontal paths which would need to be traveled within each convective flow cell. So, in summary, short-wavelength disturbances are not very destabilizing because they rapidly degrade by diffusion, and long-wavelength disturbances are not very destabilizing because they are spread out so widely in the lateral direction that the variations they induce in the thermophysical properties of the fluid are not strong enough to drive flow. Thus, of the wide range of disturbances to which the system is subjected, the one disturbance which is most destabilizing to the system and causes the onset of convection will possess some intermediate wavelength, which is determined by the competing physical behaviors associated with short-wavelength and long-wavelength disturbances. The vertical phase depth, of course, plays a large role in governing which disturbances are most unstable, as well. At this point, one could imagine the appearance of a simple graph relating the stability of the system, in terms of the critical Rayleigh number (Rayleigh number corresponding to the critical vertical temperature difference at which convection begins), to disturbances of different wavelengths. The graph (Figure 1-4) can be drawn using a general, dimensionless wavelength and the dimensionless critical Rayleigh number, which is  $Ra_{crit}$ ; numerical values for either quantity are not necessary at this point.

Once the system is at or above the critical vertical temperature difference and is subjected to the right disturbance, buoyancy-driven convection begins. Still considering a one-dimensional system, unbounded in the lateral direction, the flow pattern at the onset of convection possesses the wavelength of the disturbance which caused convection.

### 1.3.2 Rectangular System, Laterally Bounded, Periodic Lateral Boundary Conditions

Now, consider a two-dimensional system. The two-dimensional system to be considered is the system that would be obtained if two lateral walls were simply added to the left and right sides of the system of Figure 1-1, with a no-stress condition on velocity and an insulating condition on temperature imposed on each lateral wall. The horizontal width of this new system is called  $L_x$  and the vertical depth is called  $L_z$ . This system can be examined to understand the interesting physics governing convective pattern selection.

Due to the stress-free conditions on velocity and the insulating conditions on temperature at the lateral walls, the x-direction dependence of the velocities and temperatures in the system, which shall be called  $\psi$ , could be expressed in terms of cosines, in the form

$$\psi = \cos \frac{n \pi x}{L_x}, n = 0, 1, 2, 3, \dots \quad (1.2)$$

The number of convective cells which may form in the system, then, is related to  $L_x$  through this form of x-direction dependence, as is the size of the cells which form. Notice that  $n$  is an integer, so not just any pattern may arise in a laterally bounded system. Only those patterns which can be physically accommodated by the lateral width of the system may form, and so only disturbances with those shapes are physically admissible to the system. Of the set of disturbances that are physically admissible to the system, only one will be the most destabilizing and, when the critical vertical temperature difference has been exceeded, cause the onset of convection.

In a laterally bounded system, for the same reasons as in a system without side walls, disturbances that are laterally very short or very long are not very destabilizing. Thus, again the shape of the most destabilizing disturbance and onset flow pattern is determined by competition

between physical behaviors like those that were explained for short-wavelength and long-wavelength disturbances.

The size and shape of the onset flow pattern, of course, are heavily dependent on the dimensions of the system. In a system that is laterally very wide, the onset flow pattern would likely not be, for example, one very wide flow cell. A flow pattern such as that would not be sustainable for the physical reasons like those explained for disturbances of very long wavelength, which were already explained. The size of the system is typically described using the dimensionless aspect ratio. For a rectangular system, the aspect ratio is the ratio of the width of the system to the vertical height of the system, and it may be called  $A_{xz}$ . For a cylindrical system, the aspect ratio is the ratio of the radius of the system to the vertical height of the system, and it may simply be called  $A$ . For an annular system, the aspect ratio may also be called  $A$ , and it is the ratio of the outer annular radius ( $R_o$ ) to the vertical height of the system.

As the aspect ratio is varied, obviously the stability of the system to any given disturbance is varied with it. For example, a wave-shaped disturbance which induces a convective flow pattern consisting of two rolls of convecting fluid would be most destabilizing at some particular value of  $A_{xz}$ , but if the aspect ratio were slightly increased (making the container laterally wider or vertically shorter) or decreased, then that same disturbance would not be as well accommodated by the lateral width of the system, and consequently would not be as well suited to destabilize the system. The reason for this is related to physical behaviors like those described for disturbances of very short and very long wavelengths, as described for the laterally unbounded system. What is meant by a convective pattern consisting of two rolls of convecting fluid is clarified in the following cross-sectional velocity profiles of a convecting, laterally bounded system (Figure 1-5).

Continuing with the example, continuously increasing the aspect ratio would make the two-convective-roll-inducing disturbance less and less destabilizing to the system, and thus make the corresponding two-convective-roll onset flow pattern more and more difficult for the system to form and maintain; as an onset flow pattern becomes more and more difficult to form and maintain, the critical vertical temperature difference corresponding to it increases, as does the corresponding critical Rayleigh number. At some sufficiently large aspect ratio, the system would find a disturbance that induces more than two convective rolls to be more destabilizing, and the corresponding onset flow pattern to be more energetically favorable. Supposing that increasing the  $A_{xz}$  value caused the example system to become more unstable to a disturbance with that induced four convective rolls rather than two, the corresponding onset flow pattern would consist of four rolls of convecting fluid.

The stability of the system to the four-convective-roll-inducing disturbance, and the degree of difficulty that the system would have in maintaining its corresponding onset flow pattern, are again dependent on physical behaviors like the short-wavelength and long-wavelength behaviors described for laterally unbounded systems. As the  $A_{xz}$  value is further and further increased, this type of pattern-switching continues. If the  $A_{xz}$  value of the example system were further increased, the system would eventually reach an  $A_{xz}$  value at which it would be more favorable for the system to form and maintain an onset flow pattern with more than four rolls of convecting fluid. Supposing that the next flow pattern in the example consists of six rolls of convecting fluid rather than four, then difficulty that the system has in forming and maintaining this six-roll-pattern would once again be determined by physical behaviors like the short-wavelength and long-wavelength behaviors that have been explained earlier. Resulting from these physical behaviors, which correspond to the size and shape of an imposed

disturbance, the exact critical temperature difference, and critical Rayleigh number, corresponding to each different flow pattern is dependent on the  $A_{xz}$  value and has a minimum at some certain  $A_{xz}$  value that is optimal in terms of how well a system with that aspect ratio physically accommodates the flow pattern. When a system is laterally unbounded, or a system has lateral walls that are stress-free and insulated (which means the system behaves essentially like a laterally unbounded system), then the minimum possible critical Rayleigh number for any possible flow pattern is the same. Based on all of this, a graph showing the relation between the critical Rayleigh number and the value of  $A_{xz}$  is given below as Figure 1-6. Note that in a laterally unbounded system, or in a laterally bounded system with periodic lateral boundary conditions, the convective patterns that can form are comprised of convective rolls which are all of equal lateral width. As an example of what is meant by this, see the flow pattern diagrams in Figure 1-5.

In this figure, the roman numerals represent flow patterns with different numbers of convective rolls. Flow pattern “III” includes more convective rolls than “II” and flow pattern “II” includes more convective rolls than “I” does. Basically, aspect ratios at which the slope of the curve changes from positive to negative are aspect ratios at which there is a transition to a higher number of convective rolls being present in the onset flow pattern.

### **1.3.3 Rectangular System, Laterally Bounded, Non-Periodic Lateral Boundary Conditions**

When running experiments or considering practical applications, one does not encounter systems with periodic boundary conditions at their lateral walls. The more realistic case of a laterally bounded, rectangular system with non-periodic lateral boundary conditions will now be detailed.

The behavior in this system is essentially the same as what was just explained for the rectangular system with periodic lateral boundary conditions, but there are a couple of key differences: the convective rolls which form at the onset of convection are not necessarily of identical size to one another, and the minimum critical Rayleigh number for each possible flow pattern (considering different values of  $A_{xz}$ ) decreases as  $A_{xz}$  increases rather than maintaining a constant value.

Since the convective rolls which form at onset are not necessarily of identical size to one another, the flow pattern with four convective rolls in Figure 1-5 could instead appear as shown in Figure 1-7.

The second key difference of this case from the case in which the lateral boundary conditions are periodic is that for higher and higher  $A_{xz}$  values, the minimum critical temperature difference values become lower and lower. The reason for this is that the no-slip effects of the side walls do less to stabilize the system as the aspect ratio is increased. As  $A_{xz}$  approaches infinity, the critical temperature difference values for the flow patterns approach values corresponding to the well known critical Rayleigh number of 1708 that is associated with the onset of buoyancy-driven convection in laterally unbounded systems (Davis 1967). For the two-dimensional, laterally bounded system, no-slip conditions at the lateral walls, here is a general plot of the stability of the system, in terms of the critical Rayleigh number, to disturbances corresponding to different onset flow patterns; the plot is simply based on the reasoning explained above.

Again, in this figure, the roman numerals represent flow patterns with different numbers of convective rolls, where pattern “III” includes more convective rolls than “II” and pattern “II” includes more convective rolls than “I.” Recall that aspect ratios at which the slope of the curve

changes from positive to negative indicate transitions to onset flow patterns with higher numbers of convective rolls being present.

#### **1.3.4 Cylindrical System**

So far, the example systems discussed have been assumed to be laterally bounded, rectangular systems or laterally unbounded systems. Radial walls in cylindrical and annular systems significantly affect the critical conditions for the onset of convection. This research addresses primarily cylindrical and annular systems. To prevent any possible confusion, note that throughout this dissertation, “cylindrical system” (or sometimes the term “open cylindrical system” may be used) refers to a fluid system bounded by a cylindrical container, in which the entire container is filled only with fluid, and does not include a center-piece as an annular container does. From this point onward, unless otherwise noted, the systems discussed will be within vertical, cylindrical containers (meaning that the direction of gravity is parallel to the axis cutting through the radial center of the cylinder) with finite outer radii or within vertical, annular containers. To be completely clear, a vertical, annular container is one which has an annular cross-section when viewed from above.

Increasing the aspect ratio,  $A$ , in a cylindrical system has the effects on pattern selection which were just explained for the laterally bounded, rectangular system. As  $A$  is increased, the onset flow patterns include more and more convective rolls, so as to occupy the system in a more energetically favorable fashion. Also, as  $A$  approaches infinity, the value of the critical Rayleigh number approaches the value of 1708, which is well-known to be associated with laterally unbounded systems. There is, however, another aspect to pattern selection in cylindrical systems, and it will be explained now.

In a rectangular system, the number of convective rolls which form can be related to the imposed disturbance's size and shape in the x-direction. For rectangular, laterally unbounded systems, the corresponding onset flow pattern can then be described by a wave number in the x-direction, inversely proportional to the wavelength of the flow pattern in the x-direction. In all systems considered in this research, whether rectangular, cylindrical, or annular, it is most energetically favorable for the system to form onset flow patterns with only one convective roll in the vertical direction; thus, there is no need to consider a z-direction wave number, z-direction wavelength, or the size and shape of a disturbance in the z-direction for this research. The flow pattern in a rectangular system, then, can be described simply by describing its size and shape in the x-direction.

In a cylindrical system, flow patterns may have different numbers of convective rolls in the radial direction, like the patterns in rectangular systems could have different numbers of convective rolls in the x-direction. However, flow patterns in cylindrical systems may also have differing numbers of convective rolls in the azimuthal direction. The flow patterns in a cylindrical system must, of course, be periodic. The periodicity of the flow patterns in the azimuthal direction, and thus how many convective rolls exist along the azimuthal direction, is characterized by an azimuthal wave number, called  $m$ . For example, the flow pattern described by the wave number  $m = 2$  is one which repeats twice as one progresses once through the fluid layer in the azimuthal direction. For an  $m = 2$  flow pattern, progressing  $90^\circ$  around the system in the azimuthal direction, from an arbitrary starting point, leads to a point that has the opposite vertical velocity of the starting point. Likewise, for an  $m = 1$  flow pattern, progressing  $180^\circ$  around the system in the azimuthal direction, from an arbitrary starting point, leads to a point that has the opposite vertical velocity of the starting point. An  $m = 0$  flow pattern, though, is

axisymmetric in the azimuthal direction. Figure 1-9 gives examples of flow patterns possessing some of the lowest  $m$  values. In these diagrams, the letter “U” indicates upward velocities and the letter “D” indicates downward velocities. The intensity of the shading indicates the magnitude of the velocities, with darker shades representing higher velocities.

At certain aspect ratios, the a cylindrical system favors certain azimuthal periodicities, and thus, certain  $m$  values. For each  $m$  value, the system may have a differing number of convective rolls in the r-direction, and how many there are depends once again upon physical behaviors like the short-wavelength and long-wavelength behaviors that have already been explained. The relation, for each  $m$  value, between the number of convective rolls, the critical Rayleigh number needed to obtain a particular number of rolls, and the aspect ratio appears much like what is shown in Figure 1-8. Generally, in the cylindrical cases, only  $m = 0, 1, \text{ or } 2$  patterns were favored as onset patterns; this means that in most cases, the critical vertical temperature difference corresponding to the onset of convection was lower for  $m = 0, 1, \text{ or } 2$  patterns than for patterns with other azimuthal wave numbers. As the aspect ratio approaches infinity, the critical Rayleigh numbers for flow patterns of all  $m$  values approach the unbounded-system-value of 1708. A general graph showing the relation of flow patterns and their critical Rayleigh numbers to the aspect ratio in a cylindrical system is given as Figure 1-10. This graph was obtained by performing a series of computations, to determine the critical Rayleigh number corresponding to several values of the aspect ratio, using the computational program developed for obtaining computational results in this research. The computational solution method is detailed in Chapter 5, and the computational results are shown extensively in Chapter 7.

On this diagram, starting from a given aspect ratio and moving upward along the graph is analogous to increasing the vertical temperature difference across the system. Once the first of

the  $m = 0, 1, 2,$  or  $3$  curves has been reached, then this is the critical Rayleigh number corresponding to the critical vertical temperature difference. The  $m$  value of the bottom-most curve at a given aspect ratio is the  $m$  value for the onset flow pattern at that aspect ratio; this azimuthal wave number, since the critical temperature difference and critical Rayleigh number corresponding to it are lowest, is the azimuthal wave number of disturbances to which the system is most unstable. Notice that the curve for each particular  $m$  value looks much like the one in Figure 1-8, which reflects the effects of physics related to the sizes and shapes of different disturbances on the stability of the system.

Graphs like Figure 1-10 are extremely helpful in research on buoyancy-driven convection. The reader is asked to notice that the graphs presenting computational results for buoyancy-driven instability in cylindrical systems in Chapter 7 are just like the one shown in Figure 1-10. Figure 1-10, interestingly, is the correct graph for cylindrical systems of any dimensions, and it holds true regardless of the set of thermophysical properties possessed by the fluid in the system. This will be further explained at the end of Chapter 4. Note that the stability diagrams in this research would, however, differ very slightly depending on whether or not the variation of viscosity with temperature is being considered.

### **1.3.5 Annular System**

Nearly everything that was just said for cylindrical systems in Section 1.3.4 applies for annular systems, as well. An exception is that as the outer radius of the system approaches infinity (and thus, the  $A$  value approaches infinity), one would expect the critical Rayleigh number to approach a value other than 1708, which corresponds to a laterally unbounded system, since an inner radial wall is present. Patterns in annular systems are described primarily by their azimuthal wave number,  $m$ . The patterns in annular systems may also include more than one

convective roll in the radial direction, but this tends to happen only when the ratio of the inner annular radius ( $R_i$ ) to the outer annular radius ( $R_o$ ) is quite small. This ratio of radii is a new dimensionless parameter affecting pattern selection which was not present in the consideration of cylindrical systems. The radius ratio shall be called “ $S$ ” and will be given by Equation 1.3.

$$S = \frac{R_i}{R_o} \quad (1.3)$$

The effect of the radius ratio is the key difference between the annular system and the cylindrical system in terms of the formation and selection of flow patterns. Stability diagrams of the relations between  $Ra_{crit}$ , the aspect ratio, and the radius ratio ( $S$ ) for different wave numbers, and valid for systems with any set of thermophysical properties, could be made for the annular system, as well; they would appear somewhat like the one for the cylindrical system, shown as Figure 1-10. Such diagrams are shown in Chapter 7. As annular systems are the main focus of this research, they will be explained much more thoroughly in the following pages.

#### **1.4 Annulus vs. Cylinder**

Certainly, there has been a good deal of research already done on natural convection in annular systems (Stork & Müller 1972, and Littlefield & Desai 1990). However, much of that work is considerably different from the current research. For example, many of those studies involve horizontal annuli rather than the vertical annuli addressed in the current study. Secondly, of those past works which do address convection in vertical annuli, many consider the case in which heat is supplied to the system from the inner rod of the annulus rather than the case considered in this study, which is that heat is supplied to the system from its bottom wall. The case in which heat is supplied from the bottom wall is highly relevant to industrial processes, and this will soon be discussed further.

The radial walls of all cylindrical and annular systems considered in this research are assumed to be insulating. This assumption shall be maintained throughout this paper, as the radial walls in the experiments conducted for this research were made to be insulating. Whether the radial wall is treated as conducting or insulating does have an effect on what the critical vertical temperature difference is for the onset of convection. Generally, the system becomes unstable at a lower vertical temperature difference if the radial walls are insulating. This makes sense because insulating radial walls do not allow a system to dissipate thermal disturbances as easily as conducting radial walls would, and making the dissipation of thermal disturbances more difficult makes the system more unstable to convection. As one might expect, the difference between the insulating and conducting cases is more pronounced in systems that span a smaller distance in the radial direction. In such systems, the radial walls are closer to the interior of the system and so they have a relatively stronger effect on the behavior of the system. Also, whether the radial walls are insulating or conducting, it is obvious that if the system is of smaller radial extent, then the system will be more stable to convection than a wider system of matching vertical depth; this is because of the relatively larger effect of the no-slip condition on velocity imposed at the radial walls.

The addition of an inner block of circular cross-section to the center of a cylindrical system transforms the cylindrical system into an annular system. The inner block of the annular system is insulating, just like the outer radial wall, and varying the radius of this circular inner block changes the gap width occupied by fluid within the annular system. Changes in this gap width cause significant changes in the critical vertical temperature difference and flow pattern at the onset of convection in the annular system. Primary goals of this research were to better understand the phenomenon of buoyancy-driven convection in terms of how it differs in an

annular system compared to a cylindrical system, and how the onset conditions for convection in the annular system differ as the annular gap width varies.

As one may expect, the addition of a circular inner block to the cylindrical system does, because of the additional radial wall and corresponding no-slip condition on velocity that it introduces, impart to the system a higher stability to convection. That is to say, a cylindrical system of a certain vertical depth, which requires a certain vertical temperature difference for the onset of Rayleigh convection, would require a higher vertical temperature difference to convect if some small, circular block were introduced to the center of the system, converting it to an annular system. The circular center-block present in an annular system also affects the flow patterns which may appear at the onset of convection. Stork and Müller (1974) have shown experimentally that in a one-fluid annular system, heated from below, convective cells can form such that they fill the annular gap in an azimuthally aligned arrangement that is rather reminiscent of the arrangement of spokes on a bicycle tire. An example of this type of pattern presented in the work of Stork and Müller is shown as Figure 1-11. In this photograph of one of their experiments, the fluid convecting is a silicone oil, and the flow is visible due to the presence of aluminum tracer powder in the oil. When the flow is horizontal, the aluminum particles align in such a way as to reflect more light, making those sections of the oil appear lighter in color; regions of the oil which are flowing vertically appear darker in color.

As the radius of the center-block in the annulus is increased, the system becomes more stable to buoyancy-driven convection, meaning that a higher vertical temperature difference across the system is needed for convection to begin; this makes sense because as the radius of the center-block is further and further increased, there is more and more wall-surface area (and more of its accompanying no-slip effect) compared to the amount of fluid in the system. Also, as the

radius of the center-block in the annulus is changed, the number of azimuthally aligned cells changes. Generally, a greater number of azimuthally aligned cells form at the onset of convection as the radius of the center-block approaches the outer wall of the annulus, and a smaller number of azimuthally aligned cells form at the onset of convection as the radius of the center-block is decreased. This research has shown that once the radius of the center-block decreases past a certain value, new rolls of convecting fluid at the onset form in radial alignment (meaning that they span the entirety of the azimuthal direction and that they are concentric to the center-block of the annular container) in addition to the original azimuthal arrangement. An example of this, generated by the computations done for this research, is shown in Figure 1-12. In this flow profile, the velocity is scaled, negative velocities represent downward flow in the z-direction (which extends into and out of the plane of the diagram), and positive velocities represent upward flow in the z-direction. This cross-sectional velocity profile represents a cross-sectional region approximately half of the distance along the vertical depth of the system that it is computed for.

If the radius of the center-block of the annular system is further and further decreased, the radial alignment of the convective cells becomes more prominent compared to the azimuthal alignment of the cells, and the flow patterns become progressively more like those seen at the onset of convection in open, cylindrical systems. This transition in onset flow patterns was of great interest in this research.

## **1.5 Application**

Aside from its applications to the regular appearances of Rayleigh convection in nature, this study finds application in the drying of paint films, in small-scale fluidics, and notably, in semi-conductor crystal growth. The vertical Bridgman crystal growth method is commonly used

for growing semi-conductor crystals such as lead-tin-telluride. Vertical Bridgman growth involves a liquid semi-conductor melt layer, which lies atop the solid crystal phase being formed by the solidification of the melt. The arrangement is heated from above so that the crystal at the bottom of the system grows upward (see Figure 1-13). Since solidification is occurring at the liquid-solid interface, the temperature at that location is constant.

Of course, a system that is heated from above, such as this crystal growth system, will not be destabilized by the vertical temperature gradient in the system. Still, buoyancy-driven convection is possible in this system for another reason. As solidification occurs at the solid-liquid interface, some portion of the species that comprise the liquid melt is rejected into the liquid phase, near the interface. The species comprising a liquid melt, such as lead-tin-telluride, are not all equal in weight. If the species rejected the most into the liquid near the interface is relatively light in weight, and makes the liquid region near the interface less dense than the remainder of the liquid melt phase above the interfacial region, then a top-heavy system results. Thus, due to solutal gradients, buoyancy forces can cause convection in the crystal growth system just like the systems previously described in this chapter.

Convection in this system can cause impurities from the ampoule to be transmitted to the solid-liquid interface and this can cause flaws on the face of the forming crystal. Also, convection in the system can cause the heat transfer at the solidification interface to be non-uniform. For these reasons, it is desired to know the conditions corresponding to the onset of convection in this system so that it can be better understood, predicted, controlled, and prevented.

It should be mentioned that, in some cases, convection in a crystal growth system may not be a problem, and may even be desirable. If a crystal is grown at relatively low temperatures

(unlike, for example, the high value of 1250 °C at which gallium arsenide is grown), then convection helps transfer heat near the solidification interface and relieves thermal stresses there, preventing the growing crystal from fracturing. Also, the transport of impurities from the walls of the crystal-growth container to the solidification interface does not tend to become a problem in these lower-temperature systems (in high-temperature crystal growth systems, it can relate to constituents being released from the crystal growth container by the degradation of the container). Thus, in some low-temperature crystal growth systems, convection could clearly be beneficial.

In vertical Bridgman crystal growth, the depth of the liquid phase is continuously changing as the melt solidifies into the growing crystal, consuming a portion of the melt. As the phase depth changes during crystal growth, so does the possible convective flow behavior. Thus, being able to predict the convective behavior of the system at differing fluid depths is important.

Some crystal growth processes, such as the liquid-encapsulated growth of gallium arsenide, require very high temperatures. In this research, convective behavior will be studied at more moderate temperatures, as the physics driving the convection are the same regardless of the temperature of the system.

Typically, crystal growth is conducted using cylindrical fluid layers. It is interesting to ask how the convective behavior of a crystal growth system would differ if annular fluid layers were employed rather than cylindrical layers. One might imagine that the presence of an extra solid wall at the center of the fluid layer would, by means of the no-slip condition it imposes on velocities at that location, impart to the crystal growth system a greater stability to convection. The additional center wall in an annular system would allow the system to suppress more disturbances than a cylindrical system. Furthermore, if the crystal were grown in an annular

container with a sufficiently large annular center-piece (relative to the outer annular radius), then any convective patterns which did arise would be very predictable and uniform sets of only azimuthally aligned cells, which could be easier to work with than the patterns that arise in cylindrical containers.

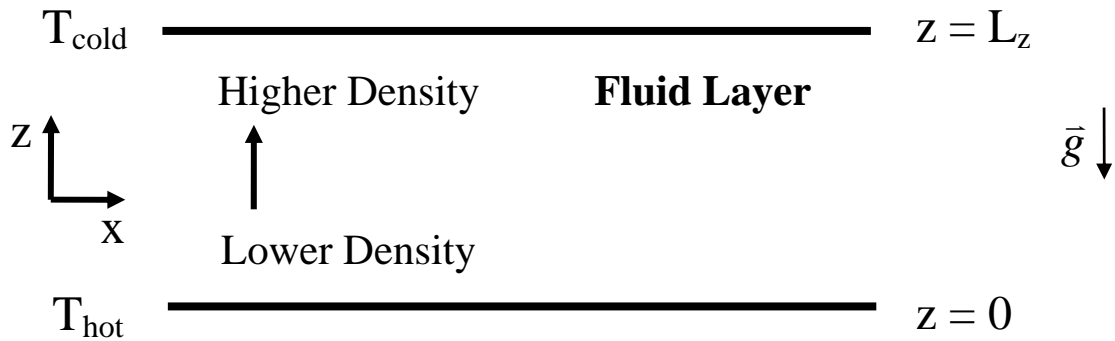


Figure 1-1. Simplified system diagram: heated from below.

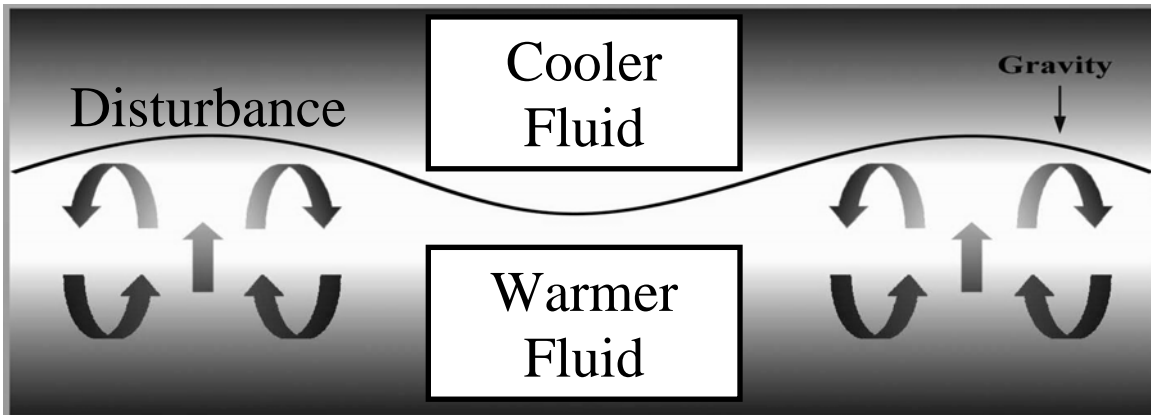


Figure 1-2. Rayleigh convection.

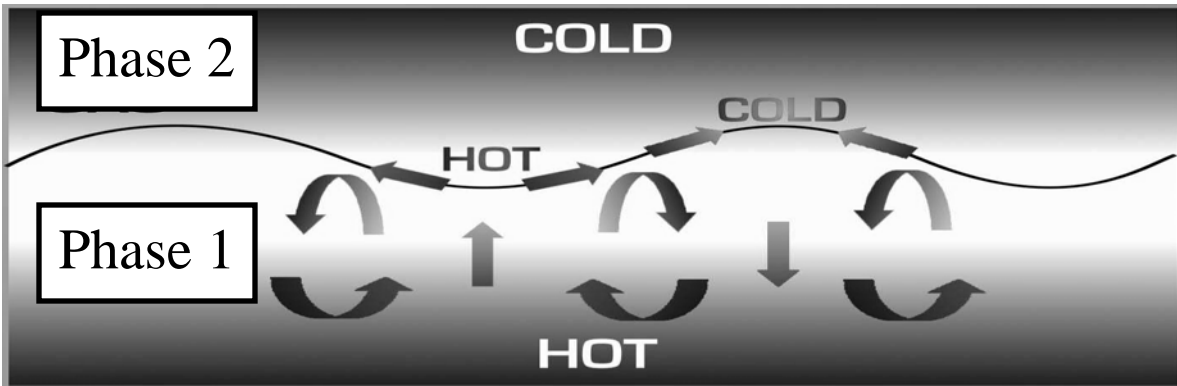


Figure 1-3. Marangoni convection.

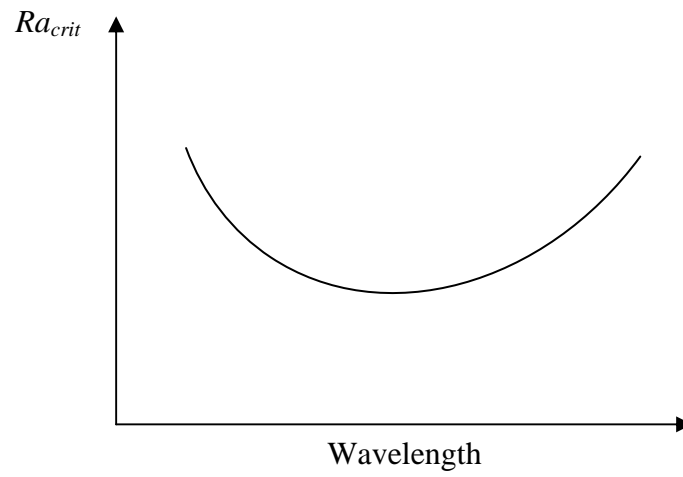


Figure 1-4. General diagram: critical Rayleigh number vs. disturbance wavelength.

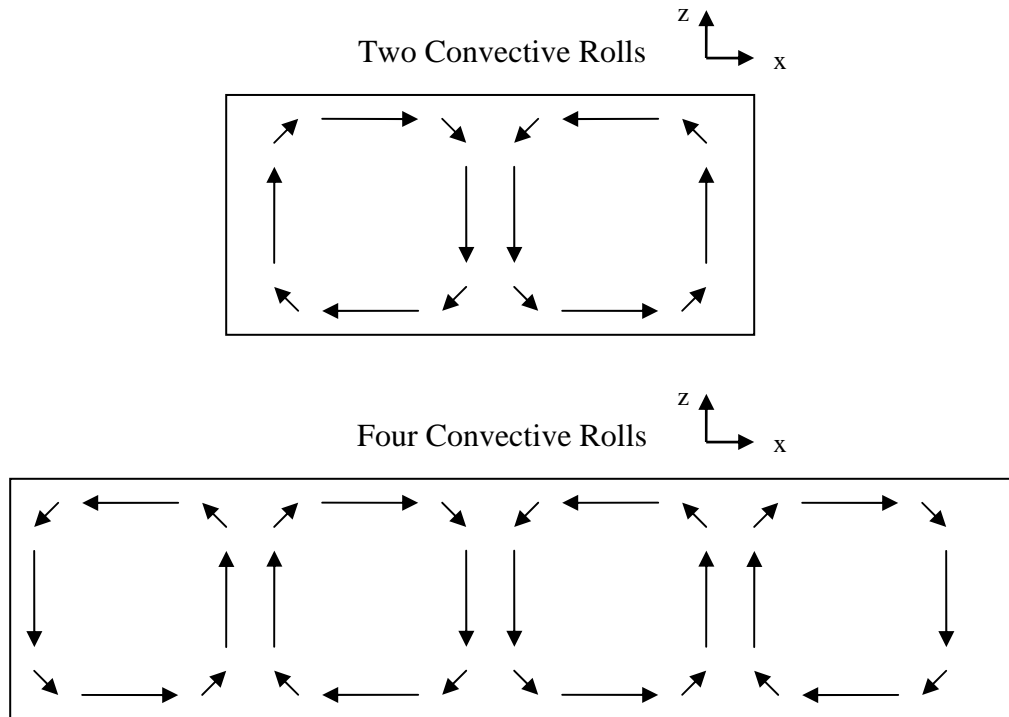


Figure 1-5. Cross-sectional velocity profiles of flow patterns with different numbers of convective rolls.

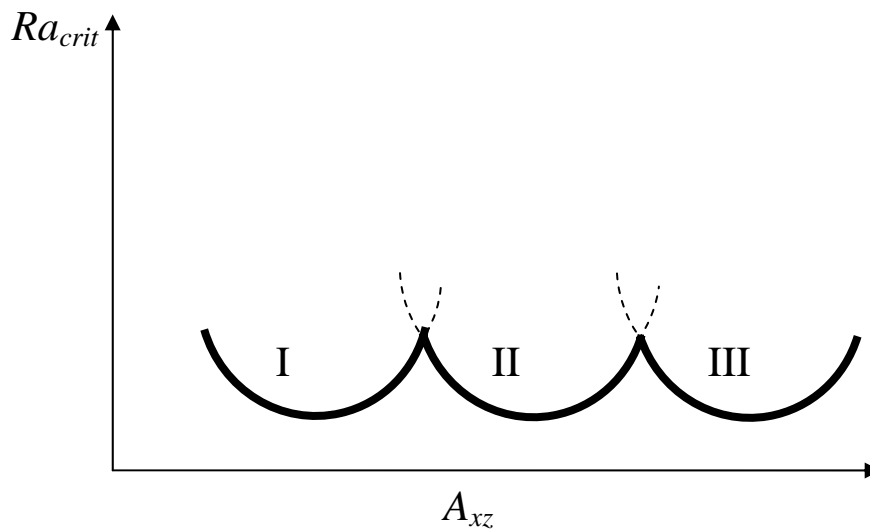


Figure 1-6. General stability diagram for buoyancy-driven convection in a rectangular, laterally bounded system, with periodic boundary conditions at lateral walls, for varying aspect ratio.

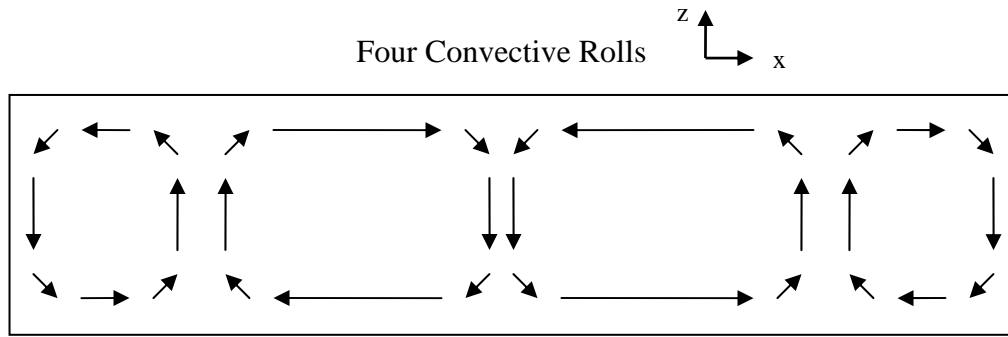


Figure 1-7. Cross-sectional velocity profiles of four-roll flow patterns with non-uniform roll size.

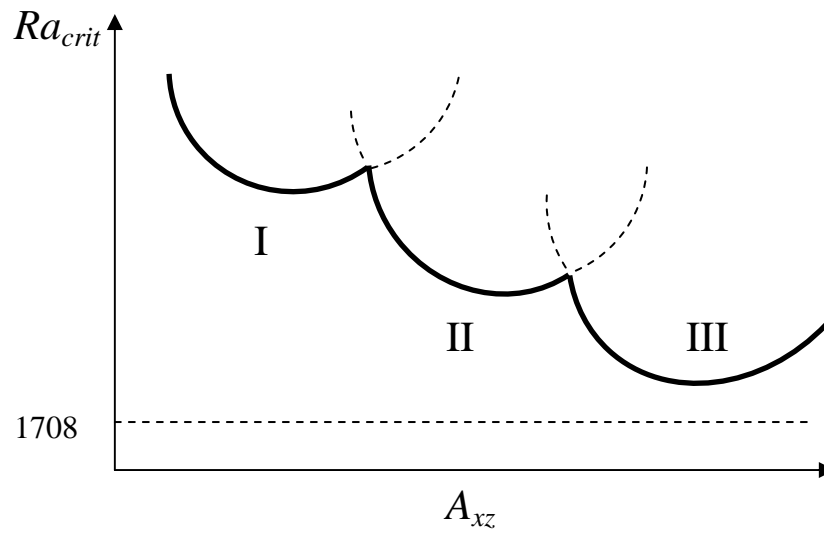


Figure 1-8. General stability diagram for buoyancy-driven convection in a rectangular, laterally bounded system, with non-periodic boundary conditions at lateral walls, for varying aspect ratio.

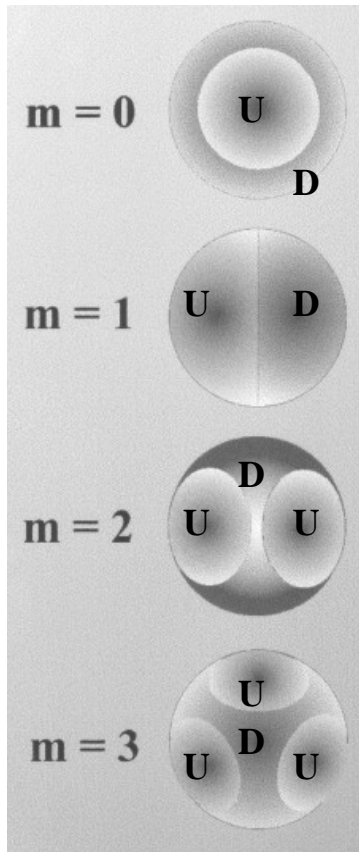


Figure 1-9. Diagrams of  $m = 0, 1, 2, 3$  flow patterns: “U”: upward flow, “D”: downward flow.

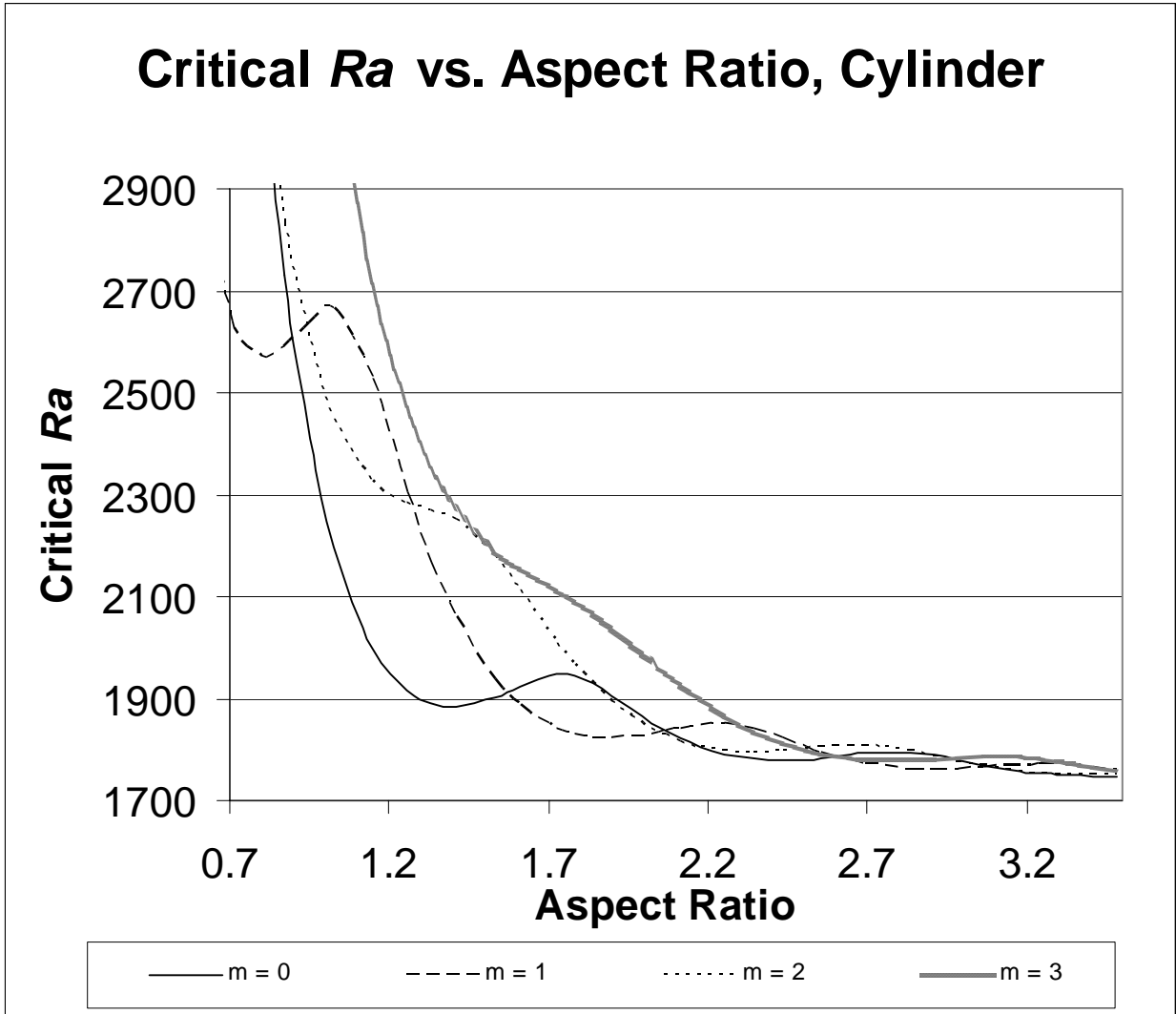


Figure 1-10. General stability diagram for buoyancy-driven convection in a cylindrical container, for varying aspect ratio.

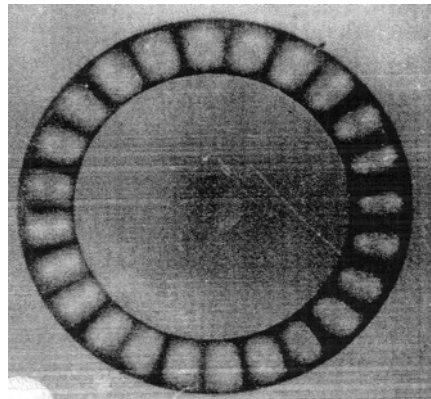


Figure 1-11. Convective flow pattern in an annulus (Stork & Müller 1974).

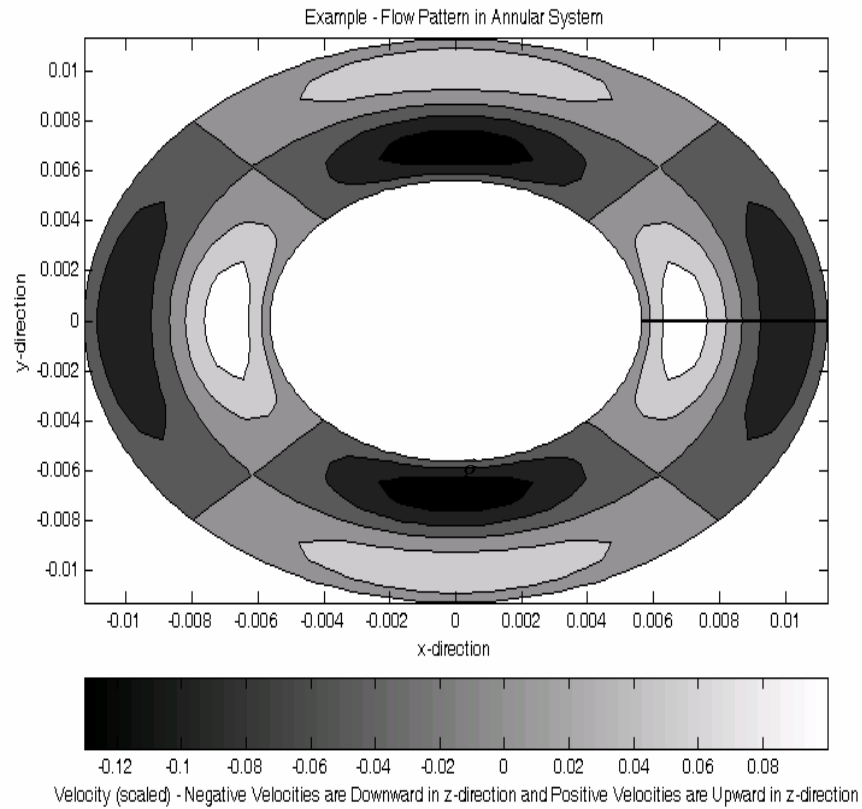


Figure 1-12. Example: computed flow profile for annular system, cross-sectional view.

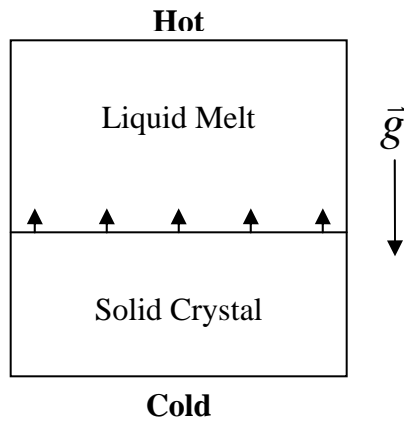


Figure 1-13. Diagram of crystal growth system.

## CHAPTER 2 LITERATURE REVIEW

Rayleigh convection in a single fluid layer has been a well-studied problem in fluid mechanics for many years, and it has branched out into many newer problems over the years. Systems with multiple fluid phases, in which Marangoni convection exists in addition to Rayleigh convection, have been studied, as well. Also, researchers have examined differences in convective behavior seen in systems of differing shapes and sizes. It would be quite difficult to give a complete history of tremendous volume of research that has been done in this general field. In this section, a brief summary of some of the past research that may be considered most relevant to this study will be given.

In Bénard's classic experiments (1900), cellular, hexagonal flow patterns in vertically thin fluid layers (about .5 mm to 1 mm deep), heated from below, and open to air at the top surface were found (Bénard 1900). Inspired by these experiments, about fifteen years later, Rayleigh investigated the instability that arises in a fluid layer heated from below (Rayleigh 1916). Originally, these researchers attributed this flow instability to buoyancy forces – the phenomenon which would be termed Rayleigh convection. However, it turned out that the cells originally observed by Bénard were caused more by surface-tension gradients than buoyancy differences. Also, it was found that the velocity and heat transfer boundary conditions on the fluid layer, as well as the size and shape of the system, had quite a significant impact on the critical conditions for the onset of convection. The early works of Bénard and Rayleigh inspired many more researchers to investigate the convective behaviors of fluid layers.

### **2.1 Single Fluid Layers**

Single fluid layers can be studied in the presence of the Marangoni effect or in its absence. The former is more relevant to the computations and experiments in this thesis. Some

of the earlier works in this area were that of Schmidt and Milverton in 1935 (Schmidt & Milverton 1935) and that of Silveston (Silveston 1958) in 1958. Both of these works involved experiments in which a single layer of liquid was heated from below and the critical vertical temperature difference for the onset of convection was determined. Schmidt and Milverton determined the critical vertical temperature difference corresponding to the onset of convection by measuring the heat transfer through the liquid layer, while increasing the vertical temperature difference, and then noting vertical temperature difference at which the heat transfer increased to a value higher than that of the initial state of pure conduction; this increase indicated the added heat transfer which accompanied the onset of convection. Silveston determined the critical vertical temperature difference in experiments not only by heat transfer measurements, but also by optical observations. In 1961, in his book, *Hydrodynamic and Hydromagnetic Stability*, Chandrasekhar made a thorough mathematical analysis of the instability that arises solely due to buoyancy in a fluid layer heated from below (Chandrasekhar 1961).

In 1967, Davis published a well-known computational study of the Rayleigh convection that can occur in a bounded, three-dimensional, rectangular box (Davis 1967). He used a Galerkin numerical scheme to model the behavior of the system, and determine the effects of lateral walls on the convective behavior. He also observed the widely known effect of greatly increasing the horizontal dimensions of the container, which is to cause the critical Rayleigh number to rapidly decrease to 1708. Lastly, as Chandrasekhar had done in his previously mentioned 1961 book, Davis explained that moderately-sized convective cells are preferred at onset to tall, narrow cells or wide, flat cells; this is because tall, narrow cells dissipate too large an amount of energy, and wide, flat cells require fluid particles to travel too great a horizontal distance before they can fall and release their potential energy. This sort of reasoning was

introduced in Chapter 1. In a 1970 paper (Charlson & Sani 1970) and an extension of it published in 1971 (Charlson & Sani 1971), Charlson and Sani did a mathematical study to determine the critical temperature difference for the onset of axisymmetric (1970) and non-axisymmetric (1971) flow patterns in cylindrical fluid layers heated from below. Their study included quite a wide range of aspect ratios (ratio of container radius to container height) and addressed the cases of both insulating and conducting side walls. In 1972, Stork and Müller published an experimental study in which they studied a system quite similar to the one mathematically analyzed by Davis in 1967 (Stork & Müller 1972). They varied the lateral dimensions of their rectangular system and found their critical temperature difference results to be generally below those of Davis. They attributed this discrepancy between experiment and theory to the effect of imperfect experimental control of the heat transfer boundary conditions at the lateral walls. In Koschmieder's 1974 experimental study, the heat flux through an oil layer before and after the onset of convection was monitored; he was, however, unable to get an accurate measure of the heat transfer through the oil layer for cases with low critical, vertical temperature differences (Koschmieder 1974).

Like this research, the 1974 experimental study of Stork and Müller addressed Rayleigh convection in annular systems. As in their 1972 work, they examined a fluid layer of 10 mm vertical depth, comprised of silicone oil mixed with aluminum tracer powder, with the temperature at the top and bottom of the layer carefully controlled. In some experiments, they considered simply a system of cylindrical cross-section, while in others, they added a center-piece to the cylinder to create an annular system. In all of their experiments, they detected the onset of convection by visual observation of the fluid layer and then obtained the critical vertical temperature difference by reading appropriately placed thermocouples. For the experiments on

cylinders, onset conditions were determined for different aspect ratios; for the experiments on annuli, the onset conditions were determined for several different annular gap widths. As mentioned earlier, their experiments on annuli resulted in flow patterns that looked rather like spokes of a wheel, with several rolls of convecting fluid (always an even number of them) aligned in the azimuthal direction. As the annular gap width was increased (meaning, for example, the center-piece of the annulus was made to be of smaller diameter), some quite interesting flow behavior was observed; for some large enough gap widths, there were more flow cells along the outer wall of the annulus than the inner wall. One important difference between the research in this thesis and the work of Stork and Müller is that this research focuses on the transition in the types of onset flow patterns that are observed when the annular gap width becomes sufficiently large (see Section 1.4), whereas this transition seemed to be more of a secondary observation in the work of Stork and Müller. In this research, annular systems of certain dimensions were designed specifically for investigating this transition in onset flow patterns. Sets of annular dimensions appropriate for this investigation were able to be chosen based on computations for the critical conditions, run for annular systems. Another important difference between this research and that of Stork and Müller is that this research includes a computation to accompany the experiments, and their work did not.

In 1990, Hardin, Sani, Henry, and Roux published a computational study in which they determined the conditions at the onset of Rayleigh convection for cylindrical systems of several aspect ratios (Hardin, Sani, Henry, & Roux 1990).

Also in 1990, Littlefield and Desai published a theoretical study in which they found the critical conditions for Rayleigh convection for an annular system with conducting side walls and with top and bottom walls that were assumed to be flat and free (Littlefield & Desai 1990). This

research differs from the work of Littlefield and Desai in multiple ways. In this research, the computations address the more realistic case, with regard to a single-fluid-layer system, in which there is a no-slip condition on velocity at the walls; additionally, the radial walls in this research were considered as insulating rather than conducting, and the variation of viscosity with temperature was accounted for. Another important difference of this research from the work of Littlefield and Desai is that it includes experiments which may be compared with the computations. The calculations of Littlefield and Desai matched qualitatively well with the experimental study of annular systems done by Stork and Müller. Like the experimental study of Stork and Müller, their work showed that as the ratio of the inner radius to the outer radius becomes larger (meaning that the annular gap becomes narrower), more and more convective cells form in the azimuthal direction at onset (larger azimuthal wave number at onset). They reached the conclusion that as the ratio of the inner radius to the outer radius (the “radius ratio” which was earlier named  $S$  for this research) becomes larger, the critical Rayleigh number (and critical vertical temperature difference) approaches the value corresponding to a vertical channel; they also determined that as the radius ratio becomes smaller, the critical Rayleigh number approaches the value corresponding to a vertical cylinder. Littlefield and Desai noted that the convective patterns which develop in the annular system have a higher tendency to include new cells in the azimuthal direction than in the radial direction. This can be explained, they say, by the physical argument that new cells which form in the azimuthal direction are more uniform in size (compared to one another and to cells already present) than new cells which form in the radial direction, and thus they form more easily because of the lower velocities and viscous stresses that they involve.

At this point, to be clear, a list of the ways in which this research differs from the previous works on Rayleigh convection in single-fluid-layer annular systems is given.

- This research includes corresponding computational and experimental work.
- In this research, dimensions of annular systems investigated computationally and experimentally were chosen particularly to focus on the transition in the types of onset flow patterns which occurs when the ratio of the inner annular radius to the outer annular radius is sufficiently small, and to determine what value for this ratio corresponds to the transition (when this ratio is small enough, the onset flow patterns can have one or more convective rolls in the radial direction, while they generally have no convective rolls in the radial direction when this ratio is larger).
- Computations for this research include the variation of viscosity with temperature.
- Computations for this research address the realistic case in which there is a no-slip condition on velocity at the walls.
- Computations for this research are for the case in which the radial walls are insulating.

Another study of Rayleigh convection in an annular system was presented in 1990 by Ciliberto, Bagnoli, and Caponeri (Ciliberto, Bagnoli, & Caponeri 1990). Their study was experimental and it involved observing the convective behavior of an annular layer of silicone oil by shadowgraph. The flow patterns observed in their study consist of an azimuthally aligned series of cells, and are consistent with the patterns seen by other researchers.

In 1995, Zhao, Moates, and Narayanan published an interesting study of Rayleigh convection in cylindrical systems (Zhao, Moates, & Narayanan 1995). The study included both theoretical and experimental parts, which agreed well with one another. The experimental apparatus used was similar to the one being used in this research. The bottom temperature of a layer of silicone oil was controlled by circulating hot water below an aluminum plate, while the top temperature was controlled by circulating cooler water above a sapphire window. Flow was visualized by means of aluminum powder which was mixed in with the silicone oil. It is noteworthy that this study addressed the changes in convective behavior which arise when one accounts for the variation of viscosity with temperature rather than simply assuming it to be

constant. It was seen that, depending on the aspect ratio of the system, the variation of viscosity with temperature could have a significant impact on not only the critical vertical temperature difference for the onset of convection, but also on the flow pattern at onset. This can be seen more later in this paper. The fact that the computations in this research account for the variation of viscosity with temperature when determining the critical conditions for convection is another noteworthy feature of this research, which may set it apart from previous works on annular systems.

## **2.2 Multiple Fluid Layers**

As mentioned, the studies on single fluid layers, for the fact that they exclude the Marangoni effect, are rather more relevant to this research. Still, some works on multiple fluid layers can be helpful in understanding what goes on in problems involving buoyancy-driven convection in single fluid layers, too. Buoyancy-driven convection, after all, is generally occurring in problems with multiple fluid layers, as well, even though the systems may be more complicated. Thus, a brief summary of it will now be given, and so will be presented a more complete picture of what sorts of research have been done on convective phenomena over the years.

Following experimental evidence obtained by Block in 1956 (Block 1956), Pearson, in 1958, produced a paper which proposed a mechanism to attribute convective flow of the type observed by Bénard to surface tension gradients rather than buoyancy forces (Pearson 1958). Pearson's study focussed on a fluid layer, heated from below, laterally unbounded, with a rigid wall as its bottom surface, and a free surface at the top. A passive gas was the upper phase in the study. In that study, the temperature of the bottom wall was held fixed, while the temperature at the upper surface was governed by a heat transfer boundary condition. At the top and bottom

surfaces of the fluid layer, Pearson considered the effects of having both conducting and insulating behaviors with regard to heat transfer. In Pearson's paper, a dimensionless number called "*B*" showed up as a preliminary form of what would, in later years, be called the Marangoni number. The Marangoni number is surface tension-driven convection's analog to the Rayleigh number of buoyancy-driven convection. Pearson's analysis assumed that the upper free surface could not deflect. In 1959, a paper by Sternling and Scriven presented physical mechanisms and a corresponding simple mathematical model to explain how several types of interfacial flows may develop in bilayer systems (Sternling & Scriven 1959). A 1964 paper by the same two authors extended Pearson's work by considering the same system but allowing deflection of the free surface (Scriven & Sternling 1964). Like Pearson's work, the work of Sternling and Scriven involved solving for the behavior of the system in response to a small, imposed disturbance. None of the works, that were just described, by Pearson, or Sternling and Scriven included an experimental component. The 1967 work of Koschmieder, however, was an experimental study of the convective behavior of a cylindrical layer of silicone oil, heated from below by a solid boundary, and cooled from above by a layer of air (Koschmieder 1967). In that study, the flow was visualized using aluminum powder, and it was found that convective flow in the system initially took the form of concentric circular rolls, and subsequently transformed into a hexagonal pattern. Koschmieder was able to make an accurate determination of the wavelengths of the flows, as well as their dependence on the dimensions of the fluid layer.

Many studies involving multiple fluid layers were performed on systems comprised of one vapor layer atop one fluid layer. It is noteworthy that in 1972, Zeren and Reynolds published a study in which they examined Rayleigh and Marangoni convection in a liquid-liquid system (Zeren & Reynolds 1972). The liquids considered were benzene and water. Their study

included both theoretical and experimental parts. They felt that the presence of contaminants in the interfacial region could have affected their experimental results significantly. The work of Ferm and Wollkind, published in 1982, improved and extended the theoretical analysis given by Zeren and Reynolds (Ferm & Wollkind 1982).

While it seems that most of the work done with annular systems has involved only single fluid layers, Bensimon, in 1988, published a study in which he experimentally examined the convective behavior in an annular layer of liquid with free boundary conditions at the top and bottom surfaces (Bensimon 1988). He arranged this system by placing a layer of silicone oil on top of a layer of mercury and leaving an air layer above the silicone oil. Flow visualization was accomplished in his study by the shadowgraph technique. In the shadowgraph images he presents in the paper, the flow patterns look quite similar to those that are seen in single-fluid-layer, annular systems.

Returning to the works of Koschmieder, an entirely experimental work was published by Koschmieder and Prahl in 1990 (Koschmieder & Prahl 1990). It investigated the tendency of wide fluid layers, when heated from below and open to air at the top surface, to convect in a pattern of hexagonal cells. They examined silicone oil-air bilayers in small containers of differing shapes to find out what effects the differing container shapes had on the convective patterns that would form. They observed that as the width-to-height ratio for the containers increased, more and more convective cells would form at the onset in order to fill the larger width. While determining the critical conditions by observation of the vertical heat transfer through the system is a nice method in terms of objectivity, Koschmieder and Prahl point out that in their experiments with small fluid layers, the voltage created by the heat sensor was too small in comparison with outside electrical noise to be useful. Thus, the more desirable method (which

is the method used in the current research) was to optically observe the fluid layers and note the first appearance of fluid motion as the critical point. A 1992 experimental work by Koschmieder and Switzer examined surface-tension driven convection using shadowgraphy (Koschmieder & Switzer 1992).

In a 1995 paper by Zhao, Wagner, Narayanan, and Friedrich, a theoretical study is presented that addresses Rayleigh and Marangoni convection in fluid bilayer systems – both liquid-liquid, and liquid-vapor (Zhao, Wagner, Narayanan, & Friedrich 1995). A wide range of cases are considered, including heating from below, heating from above, and the case in which solidification is occurring at the bottom surface of a liquid-liquid bilayer; the last case mentioned has strong similarity to crystal growth because of the solidification which it accounts for. The 1996 theoretical study of Dauby and Lebon addressed the Rayleigh and Marangoni effects in a liquid-vapor bilayer system and included both linear and nonlinear analyses (Dauby & Lebon 1996). The linear analysis allows one to determine the critical vertical temperature difference at which convection begins, as well as the flow pattern at the onset. The nonlinear analysis provides more specific information on the flow behavior and can be used to predict supercritical behaviors. Most theoretical studies, up to this point, had assumed laterally unbounded systems. That assumption allows separation of variables, and thus an easier solution to the system of differential equations that model the problem. Of course, in actual experiments and other applications of these phenomena, lateral walls are present, and these walls can have important effects on the critical conditions and onset flow patterns. Thus, another point of interest in the study by Dauby and Lebon is that they formed their mathematical model to include no-slip walls at the lateral boundaries. This is the most realistic boundary condition that could be enforced at those locations. Dauby and Lebon found their theoretical results to be in good qualitative

agreement with the experimental results of Koschmieder and Prahl. In 1997 by Kats-Demyanets, Oron, and Nepomnyashchy published a study, which examines convective behavior in tri-layer fluid systems, and thus is also quite applicable to the science of crystal growth (Kats-Demyanets, Oron, & Nepomnyashchy 1997). Johnson and Narayanan published a tutorial in 1999 which explained five different mechanisms by which convection in two vertically stacked fluid layers could couple (Johnson & Narayanan 1999). Their tutorial also discussed the situation in which, at certain aspect ratios, due to the effects of side walls and the dimensions of the system, a convecting system may find two flow patterns equally favorable from an energy standpoint; as a result, the system would oscillate between the two patterns. A point such as this is called a codimension-two point.

## CHAPTER 3 MODELING EQUATIONS

To predict the onset conditions of convection requires a model that respects the physics of the problem. Such a model would utilize momentum, mass, and energy equations. The inputs to the model would be the vertical phase depth and thermophysical properties of the fluid, and the outputs would be the critical temperature difference needed for convection, as well as the associated pattern of the flow. The details of such a model are given in this chapter, while later in this thesis, an explanation of the numerical scheme used to solve the system of modeling equations is given. In Appendix C, the modeling equations are presented and developed more fully for the simple case in which the fluid is assumed to have a viscosity constant with respect to temperature. The modeling equations presented and developed throughout this chapter and Chapter 4, however, are for a more physically accurate mathematical model, in which the variation of viscosity with temperature is included.

To get started the nonlinear equations that govern flow in a convecting layer of fluid shall be introduced. These equations are nonlinear primarily on account of the dependence of velocity on temperature, coupled with the effects of the interactions between velocity and temperature fields on heat transport.

### 3.1 Nonlinear Equations

The domain equations used to model the convective behavior of the system are the momentum equation, the energy equation, and the continuity equation, which, respectively, are

$$\rho \frac{\partial \bar{v}}{\partial t} + \rho \bar{v} \cdot \nabla \bar{v} = -\nabla P + \rho \bar{g} + \nabla \cdot \bar{S}, \quad (3.1)$$

$$\rho C_v \frac{\partial T}{\partial t} + \rho C_v \bar{v} \cdot \nabla T = k \nabla^2 T, \quad (3.2)$$

$$\frac{\partial \rho}{\partial t} = \nabla \cdot (\rho \bar{v}). \quad (3.3)$$

In these equations,  $\rho$  is the density of the fluid,  $t$  is time,  $\bar{v}$  is the velocity of the fluid,  $P$  is the pressure of the fluid,  $\bar{g}$  is gravity,  $\bar{\bar{S}}$  is the stress tensor for the fluid,  $C_V$  is the constant-volume heat capacity of the fluid,  $T$  is the temperature of the fluid, and  $k$  is the thermal conductivity of the fluid.

The last term of the momentum equation has not been further simplified, at this point, because it will be needed in this form in order to properly account for the dependence of the fluid's viscosity on temperature. The stress tensor,  $\bar{\bar{S}}$ , can be expanded as

$$\bar{\bar{S}} = 2\mu \left[ \frac{\nabla \bar{v} + (\nabla \bar{v})^\tau}{2} \right]. \quad (3.4)$$

The use of this expansion, however, will be postponed for now. In this expansion,  $\mu$  is the dynamic viscosity of the fluid and  $\tau$  represents a transposed matrix. Since the velocity gradients in this system will not be very large, the energy equation has been simplified by neglecting the viscous dissipation. The system of equations is analyzed in cylindrical coordinates, which are clearly the natural choice for this problem; thus “r” denotes the radial direction, “ $\theta$ ” denotes the azimuthal direction, and “z” denotes the vertical direction. The system may be treated as periodic in the  $\theta$ -direction (this is accomplished mathematically by the expansion of the variables into modes), with the oscillations of the form  $e^{im\theta}$ , in which  $m$  is the azimuthal wave number.

Another approximation is to be made, and it affects the momentum equation. It is called the Boussinesq approximation and it addresses the variation of density with temperature. This approximation says that variation of density with temperature is negligible insofar as the change

in momentum or mass is concerned, but that it does affect the acceleration in the system insofar as the body forces are concerned. The reasoning for introducing the Boussinesq approximation, and some notes on its applicability are explained in Appendix B as Section B.1.

Once the Boussinesq approximation is applied to Equation 3.1, it becomes

$$\rho_R \frac{\partial \bar{v}}{\partial t} + \rho_R \bar{v} \cdot \nabla \bar{v} = -\nabla P + \rho_R (1 - \alpha(T - T_R)) \bar{g} + \nabla \cdot \bar{S}. \quad (3.5)$$

In Equation 3.5,  $T_R$  and  $\rho_R$  are a reference temperature and the fluid's density at the reference temperature, respectively, and  $\alpha$  is the volumetric thermal expansion coefficient of the fluid phase. Note, also, that the Boussinesq approximation results in the disappearance of the time-derivative term of the continuity equation. At this point, multiple nonlinearities appear in the system of equations; a note about these nonlinearities is given in the appendix as Section B.2.

An additional modification to the momentum equation is to define a modified pressure, which is

$$-\nabla p = -\nabla P + \rho_R \bar{g}. \quad (3.6)$$

Using this, the momentum equation may be written as

$$\rho_R \frac{\partial \bar{v}}{\partial t} + \rho_R \bar{v} \cdot \nabla \bar{v} = -\nabla p - \rho_R \alpha (T - T_R) \bar{g} + \nabla \cdot \bar{S}. \quad (3.7)$$

Now, the expansion of  $\bar{S}$  shall be introduced to the momentum equation. The result of doing so is

$$\begin{aligned} \rho_R \frac{\partial \bar{v}}{\partial t} + \rho_R \bar{v} \cdot \nabla \bar{v} = & -\nabla p - \rho_R \alpha (T - T_R) \bar{g} + \mu \nabla^2 \bar{v} + \\ & (\nabla \mu) \cdot (\nabla \bar{v} + (\nabla \bar{v})^T). \end{aligned} \quad (3.8)$$

As mentioned, a goal of this calculation is to include the effects of the variation of viscosity with temperature. Thus, the viscosity at any location can be written as

$$\mu = \mu_R [f(T - T_R)], \quad (3.9)$$

where  $f$  is some function of the difference between the temperature at that location and the reference temperature. In this equation,  $\mu_R$  is the dynamic viscosity at the reference temperature. Note that, since  $\mu$  has the same dimensions as  $\mu_R$ ,  $f$  must be dimensionless.

Using this expansion, Equation 3.8 may be rewritten as

$$\begin{aligned} \rho_R \frac{\partial \bar{v}}{\partial t} + \rho_R \bar{v} \cdot \nabla \bar{v} = -\nabla p - \rho_R \alpha (T - T_R) \bar{g} + \mu_R f \nabla^2 \bar{v} + \\ \mu_R (\nabla f) \cdot (\nabla \bar{v} + (\nabla \bar{v})^T) . \end{aligned} \quad (3.10)$$

The assumed form for viscosity's temperature dependence will be exponential, like the form assumed in the work of Zhao, Moates, and Narayanan (Zhao, Moates, & Narayanan 1995).

The form of this exponential temperature dependence is

$$f(T - T_R) = e^{B(T - T_R)}, \quad (3.11)$$

in which  $B$  is a constant that can be determined using measurements of the fluid's viscosity obtained at a range of different temperatures. For temperatures in degrees Celsius, the dimensions of  $B$  would be  $\frac{1}{^\circ\text{C}}$ .

In this system of three domain equations, it appears that five unknowns are present. These are the velocities in the  $r$ ,  $\theta$ , and  $z$  directions, the pressure, and the temperature. The continuity equation can eliminate pressure by representing it in terms of velocities, and this reduces the number of unknowns to four. To solve for the convective behavior of a cylindrical system, constraints would be needed on the velocities in the  $r$ ,  $\theta$ , and  $z$  directions, as well as on the temperature, at the top wall ( $z = L_z$ ), the bottom wall ( $z = 0$ ), and the outer radial wall ( $r = R_o$ ). Considering an annular system, however, four additional mathematical constraints are

required; these constraints on the three components of velocity and temperature are applied at the inner radial wall of the system ( $r = R_i$ ). Figure 3-1 shows the geometry being considered. The symbol  $L_r$  is used to denote the radius in a cylindrical system, and also to denote the difference between  $R_o$  and  $R_i$  ( $L_r = R_o - R_i$ ) for an annular system. This means that for an annular system,  $L_r$  is the width of the annular gap that is filled with fluid.

Thus, for the annular system, a total of sixteen constraints are needed, while only twelve are needed for the cylindrical system. These constraints are the boundary conditions. In their unscaled form, they are

$$v_r = v_\theta = v_z = 0 \text{ at } z = 0, \quad (3.12)$$

$$T = T_b \text{ at } z = 0, \quad (3.13)$$

$$v_r = v_\theta = v_z = 0 \text{ at } z = L_z, \quad (3.14)$$

$$T = T_t \text{ at } z = L_z, \quad (3.15)$$

$$v_r = v_\theta = v_z = 0 \text{ at } r = R_o, \quad (3.16)$$

$$\frac{\partial T}{\partial r} = 0 \text{ at } r = R_o, \quad (3.17)$$

and, when considering an annular system, the conditions at the inner annular wall,

$$v_r = v_\theta = v_z = 0 \text{ at } r = R_i, \quad (3.18)$$

$$\frac{\partial T}{\partial r} = 0 \text{ at } r = R_i \quad (3.19)$$

are needed.

In these equations,  $v_r$ ,  $v_\theta$ , and  $v_z$  are the components of velocity in the  $r$ ,  $\theta$ , and  $z$  directions, respectively. The boundary conditions on velocity enforce no-slip behavior at the

walls, and state that no flow may pass through the walls. The conditions on temperature at bottom and top walls keep the temperature fixed at those locations; in these equations,  $T_b$  and  $T_t$  are the constant temperatures at the bottom wall and top wall, respectively. The conditions on temperature at the radial walls represent the insulating behavior at those boundaries.

### 3.2 Scaling

Now that the complete set of domain equations and boundary conditions has been listed, these equations will be made dimensionless. In scaling these equations, one has the option to choose several combinations of parameters to use in defining a characteristic velocity ( $\bar{v}$ ) and a characteristic time ( $\bar{t}$ ). A brief discussion of how to choose these parameters is in Section B.3 of Appendix B.

Lengths are scaled using the vertical depth of the fluid. With that said, a list of the scaling relations used will now be presented. In these equations, the “hat” symbol indicates a dimensionless variable, and the “bar” indicates a characteristic value for a variable. The scaling relations are

$$\hat{v} = \frac{v}{\bar{v}}, \quad (3.20)$$

$$\hat{T} = \frac{T - T_R}{\Delta T}, \quad (3.21)$$

$$\Delta T = T_b - T_t, \quad (3.22)$$

$$\hat{p} = \frac{p}{\bar{p}}, \quad (3.23)$$

$$\bar{p} = \frac{\mu_R \bar{v}}{L_z}, \quad (3.24)$$

$$\hat{t} = \frac{t}{\bar{t}}, \quad (3.25)$$

$$\hat{\nabla} = L_z \nabla. \quad (3.26)$$

In the above equations,  $L_z$  is the vertical depth of the fluid phase. As mentioned earlier,  $T_R$  is the reference temperature. In simple cases where the system of equations was solved without considering the dependence of viscosity on temperature,  $T_R$  could be chosen to be the temperature at the top boundary of the system ( $T$ ), and the reference dynamic viscosity,  $\mu_R$ , would simply be the dynamic viscosity at that temperature. When the variation of viscosity with temperature is considered, however,  $T_R$  is selected later, during the numerical solution of the system of equations, to correspond to the mean dynamic viscosity value of the fluid in its motionless base state, when the fluid layer is at the critical vertical temperature difference, just before the onset of convection (the viscosity of the fluid varies from top to bottom along the motionless liquid layer corresponding to the vertical temperature gradient). When the variation of viscosity with temperature is being considered, this mean dynamic viscosity value is the reference dynamic viscosity,  $\mu_R$ .  $\Delta T$  is the overall temperature difference across the system.

In addition to these scalings,  $f$  (Equation 3.11) should be re-expressed in terms of dimensionless temperature. This new version of  $f$ , which will be called  $F$ , is

$$F(\hat{T}) = e^{B(\Delta T)\hat{T}}. \quad (3.27)$$

Applying these scalings to the domain equations, the following dimensionless (though the “hat” symbol will now be discarded) equations are obtained (Equations 3.28-3.30):

$$\frac{\rho_R L_z^2}{\mu_R \bar{t}} \frac{\partial \bar{v}}{\partial t} + \frac{\rho_R L_z \bar{v}}{\mu_R} \bar{v} \cdot \nabla \bar{v} = -\nabla p - \frac{\alpha L_z^2 \bar{g}(\Delta T)}{\nu \bar{v}} T + F \nabla^2 \bar{v} + (\nabla F) \cdot (\nabla \bar{v} + (\nabla \bar{v})^\tau) \quad (3.28)$$

$$\frac{L_z^2}{\kappa \bar{t}} \frac{\partial T}{\partial t} + \frac{L_z \bar{v}}{\kappa} \bar{v} \cdot \nabla T = \nabla^2 T, \quad (3.29)$$

$$0 = \nabla \cdot \bar{v}, \quad (3.30)$$

in which  $\kappa$ , the thermal diffusivity of the fluid, is equal to the fluid's thermal conductivity divided by the product of its density and heat capacity.

Unless otherwise indicated, all thermophysical properties in these equations are considered at the reference temperature. The subscript "R" has not been included on the symbols for all of these properties; however, it has been left on the symbols  $\rho_R$  and  $\mu_R$  because, in those cases, it arose from the expansions by which the density and dynamic viscosity of the fluid were defined. This is the reason, for example, that the subscript "R" is not included on the kinematic viscosity in Equation 3.28, even though that property is simply a ratio of the dynamic viscosity and the density taken at the reference temperature. Observe that if a substitution of the ratio of  $\kappa$  to  $L_z$  were made for  $\bar{v}$ , then the coefficient of the temperature term in Equation 3.28 would be the Rayleigh number. Since many possible values could be assigned to  $\bar{v}$ , depending on the relative values of system parameters,  $\bar{v}$  has been left in the set of modeling equations. Again, a discussion regarding the definition of  $\bar{v}$  is in Section B.3 of Appendix B.

As for the scaling of the boundary conditions, the conditions on velocity remain unchanged in appearance, as do the conditions on temperature at the radial walls. However, the conditions on temperature at the top and bottom walls appear slightly differently depending on whether or not the problem is being solved considering the variation of viscosity with temperature. The reader is asked to refer to Appendix C for more information on the case in which this variation is not being considered. In cases in which the variation of viscosity with temperature is being considered, the dimensionless temperatures at the vertical boundaries are dependent on  $T_R$ .  $T_R$ , though, is dependent on the vertical temperature gradient in the fluid, which means that it needs to be determined along with the critical vertical temperature difference

for convection by an iterative approach (described in Chapter 5). Thus, for the non-constant viscosity case, the temperature boundary conditions at the top and bottom walls must be left in a more general form for now. In this general form, they are

$$T = \frac{T_b - T_R}{\Delta T} \text{ at } z = 0, \quad (3.31)$$

$$T = \frac{T_t - T_R}{\Delta T} \text{ at } z = L_z. \quad (3.32)$$

This completes the presentation of the scaled domain equations and boundary conditions.

Next, the equations shall be simplified by linearization and the removal of time dependence.

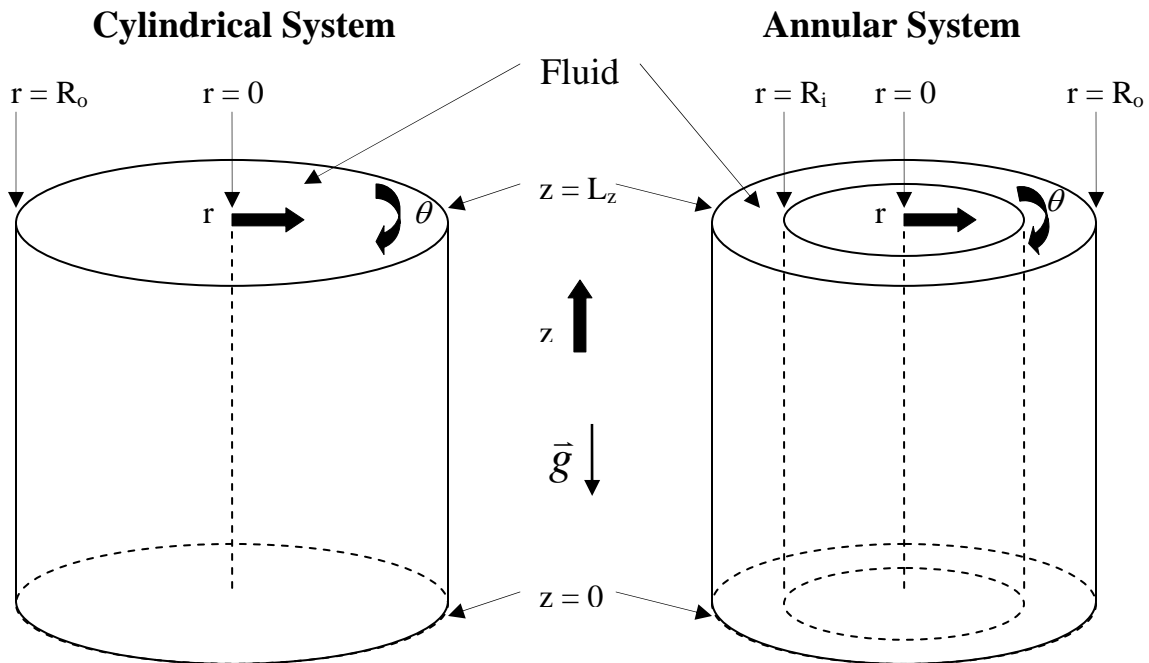


Figure 3-1. System diagram: cylindrical and annular systems.

## CHAPTER 4 LINEARIZED EQUATIONS

In this chapter, the process of simplifying the set of modeling equations by linearizing them around a motionless base state, and then eliminating their time dependence shall be shown. Since the goals of the calculations in this research are to determine only the onset conditions for convection (critical vertical temperature difference and flow pattern at onset) as opposed to the flow behavior at supercritical conditions, a linearized model is sufficient for the analysis. A nonlinear calculation would be necessary if the supercritical behavior of the system were to be determined. Time dependence is being removed from the equations because a system is independent of time at critical conditions (also known as marginal stability). Linearization and the removal of time dependence are accomplished by introducing a series perturbation expansion to the variables, then applying a further expansion to the perturbed variables (expansion into modes), and then setting the inverse time constant in the expansion equal to zero. As mentioned earlier, the same process is presented for the less complex case in which the fluid is assumed to have a constant viscosity with respect to temperature is included in Appendix C.

### **4.1 Linearization**

The system of equations shall be linearized around the motionless base state of the system. In this motionless initial state, heat is transferred within the system only in the vertical direction and only by conduction.

The form of the expansions which shall be used in this linearization, considering, for example, the expansion of velocity, is

$$\bar{v} = \left[ \bar{v} \Big|_{\varepsilon = 0} \right] + \varepsilon \left[ \frac{\partial \bar{v}}{\partial \varepsilon} \Big|_{\varepsilon = 0} \right] + \frac{1}{2!} \varepsilon^2 \left[ \frac{\partial^2 \bar{v}}{\partial \varepsilon^2} \Big|_{\varepsilon = 0} \right] + \frac{1}{3!} \varepsilon^3 \left[ \frac{\partial^3 \bar{v}}{\partial \varepsilon^3} \Big|_{\varepsilon = 0} \right] + \dots \quad (4.1)$$

Replacing the expressions in brackets, this may be rewritten as

$$\bar{v} = \bar{v}_0 + \varepsilon \bar{v}_1 + \frac{1}{2!} \varepsilon^2 \bar{v}_2 + \frac{1}{3!} \varepsilon^3 \bar{v}_3 + \dots \quad (4.2)$$

The subscript “0” denotes values pertaining to the motionless base state, in which heat is transferred only by conduction, and the temperature and pressure gradients are only in the vertical direction. Clearly, then,  $\bar{v}_0$  is equal to zero. This fact allows the cancellation of some terms in the linearized forms of the modeling equations. If the system begins to flow due to some perturbation, then the remaining terms in this series ( $\bar{v}_1, \bar{v}_2$ , etc.), which are the perturbed variables, represent the flow behavior of the system. The amplitude of the perturbation that transforms the base state into the flowing, “perturbed” state is called  $\varepsilon$ ; this perturbation is taken to be extremely small. Considering a small perturbation allows a conclusion on the stability of the system to be reached using linearized equations. If a system is unstable to a small perturbation, it will, of course, be unstable to larger perturbations. If a system is stable to a small perturbation, then no such conclusion may be drawn; in this case, the system could simply require a larger disturbance to become unstable. The linearized equations (comprised of terms that are first order in  $\varepsilon$ ) are an approximation of the behavior of the system and can be used to determine the conditions corresponding to the onset of convection and the pattern of flow at the onset. If it is desired to determine the magnitudes of the velocities in the convecting fluid, as

opposed to simply determining their values relative to one another, then a nonlinear analysis is necessary.

A disturbance of magnitude  $\varepsilon$  is mathematically applied to the system by expanding each variable in the modeling equations with the form shown in Equation 4.2. The set of linearized equations is then obtained by collecting only the terms which are first order in  $\varepsilon$ . The resulting linearized domain equations are

$$\frac{\rho_R L_z^2}{\mu_R \bar{t}} \frac{\partial \bar{v}_1}{\partial t} = -\nabla p_1 - \frac{\alpha L_z^2 \bar{g}(\Delta T)}{\nu \bar{v}} T_1 + F_0 \nabla^2 \bar{v}_1 + (\nabla F_0) \cdot (\nabla \bar{v}_1 + (\nabla \bar{v}_1)^T), \quad (4.3)$$

$$\frac{L_z^2}{\kappa \bar{t}} \frac{\partial T_1}{\partial t} + \frac{L_z \bar{v}}{\kappa} \frac{\partial T_0}{\partial z} v_{1z} = \nabla^2 T_1, \quad (4.4)$$

$$0 = \nabla \cdot \bar{v}_1. \quad (4.5)$$

In these equations,  $F_0$  is the same as  $F$  except that the exponential temperature value is now the base state temperature,  $T_0$ .  $F_0(T_0)$ , then, is

$$F_0(T_0) = e^{B(\Delta T)T_0}. \quad (4.6)$$

The linearized forms of the boundary conditions are

$$v_{1r} = v_{1\theta} = v_{1z} = 0 \text{ at } z = 0, \quad (4.7)$$

$$T_1 = 0 \text{ at } z = 0, \quad (4.8)$$

$$v_{1r} = v_{1\theta} = v_{1z} = 0 \text{ at } z = L_z, \quad (4.9)$$

$$T_1 = 0 \text{ at } z = L_z, \quad (4.10)$$

$$v_{1r} = v_{1\theta} = v_{1z} = 0 \text{ at } r = R_o, \quad (4.11)$$

$$\frac{\partial T_1}{\partial r} = 0 \text{ at } r = R_o, \quad (4.12)$$

and, when considering an annular system,

$$v_{1r} = v_{1\theta} = v_{1z} = 0 \text{ at } r = R_i, \quad (4.13)$$

$$\frac{\partial T_1}{\partial r} = 0 \text{ at } r = R_i \quad (4.14)$$

hold.

Linearization simplifies the boundary conditions on temperature at the top and bottom walls because it is the base state values of temperature,  $T_0$  at the top wall and bottom wall, which are equal to the fixed values of temperature at those boundaries.

Substituting for  $F_0$  in the momentum equation, and making use of

$$\nabla F_0 = \frac{\partial F_0}{\partial T_0} \nabla T_0 = \frac{\partial F_0}{\partial T_0} \frac{\partial T_0}{\partial z} \bar{\delta}_z, \quad (4.15)$$

in which  $\bar{\delta}_z$  is the unit vector in the z-direction, brings the momentum equation into the form

$$\begin{aligned} \frac{\rho_R L_z^2}{\mu_R \bar{t}} \frac{\partial \bar{v}_1}{\partial t} = & -\nabla p_1 + \frac{\alpha L_z^2 g (\Delta T)}{\nu \bar{v}} T_1 \bar{\delta}_z + e^{B(\Delta T)T_0} \nabla^2 \bar{v}_1 + \\ & (B(\Delta T) e^{B(\Delta T)T_0} \frac{\partial T_0}{\partial z}) \bar{\delta}_z \cdot (\nabla \bar{v}_1 + (\nabla \bar{v}_1)^T) . \end{aligned} \quad (4.16)$$

Note that all factors on the right-hand-side of Equation 4.15 are dimensionless since  $\nabla F_0$ , from which they arose, was already made dimensionless in Chapter 3. For a more detailed and well given explanation of this perturbation method, refer to the book titled *Interfacial Instability* by Johns and Narayanan (Johns & Narayanan 2002). The momentum equation (Equation 4.16) is now rewritten as the three scalar equations which are its components in the r,  $\theta$ , and z directions. The  $\nabla$  operators are expanded in cylindrical coordinates from this point

onward. The scalar component equations comprising the vector form of the momentum equation are the r-component of the momentum equation, the  $\theta$ -component of the momentum equation, and the z-component of the momentum equation, which, respectively, are

$$\begin{aligned} \frac{L_z^2}{\nu \bar{t}} \frac{\partial v_{1_r}}{\partial t} &= -\frac{\partial p_1}{\partial r} + \\ e^{B(\Delta T)T_0} &\left[ \left[ \frac{\partial^2}{\partial r^2} + \frac{1}{r} \frac{\partial}{\partial r} + \frac{1}{r^2} \frac{\partial^2}{\partial \theta^2} + \frac{\partial^2}{\partial z^2} - \frac{1}{r^2} \right] v_{1_r} - \right. \\ &\left. \left[ \frac{2}{r^2} \frac{\partial}{\partial \theta} \right] v_{1_\theta} \right] + \\ (B(\Delta T)e^{B(\Delta T)T_0} \frac{\partial T_0}{\partial z}) &\left[ \frac{\partial v_{1_r}}{\partial z} + \frac{\partial v_{1_z}}{\partial r} \right], \end{aligned} \quad (4.17)$$

$$\begin{aligned} \frac{L_z^2}{\nu \bar{t}} \frac{\partial v_{1_\theta}}{\partial t} &= -\frac{1}{r} \frac{\partial p_1}{\partial \theta} + \\ e^{B(\Delta T)T_0} &\left[ \left[ \frac{\partial^2}{\partial r^2} + \frac{1}{r} \frac{\partial}{\partial r} + \frac{1}{r^2} \frac{\partial^2}{\partial \theta^2} + \frac{\partial^2}{\partial z^2} - \frac{1}{r^2} \right] v_{1_\theta} + \right. \\ &\left. \left[ \frac{2}{r^2} \frac{\partial}{\partial \theta} \right] v_{1_r} \right] + \\ (B(\Delta T)e^{B(\Delta T)T_0} \frac{\partial T_0}{\partial z}) &\left[ \frac{\partial v_{1_\theta}}{\partial z} + \frac{1}{r} \frac{\partial v_{1_z}}{\partial \theta} \right], \end{aligned} \quad (4.18)$$

$$\begin{aligned}
\frac{L_z^2}{\nu \bar{t}} \frac{\partial v_{1z}}{\partial t} &= -\frac{\partial p_1}{\partial z} + \\
e^{B(\Delta T)T_0} &\left[ \left[ \frac{\partial^2}{\partial r^2} + \frac{1}{r} \frac{\partial}{\partial r} + \frac{1}{r^2} \frac{\partial^2}{\partial \theta^2} + \frac{\partial^2}{\partial z^2} \right] v_{1z} \right] + \\
(B(\Delta T)e^{B(\Delta T)T_0} \frac{\partial T_0}{\partial z}) &\left[ 2 \frac{\partial v_{1z}}{\partial z} \right] + \frac{\alpha L_z^2 g(\Delta T)}{\nu \bar{v}} T_1 .
\end{aligned} \tag{4.19}$$

## 4.2 Expansion into Normal Modes

The set of domain equations now includes Equations 4.4, 4.5, 4.17, 4.18, and 4.19. A second expansion (expansion into modes) will now be applied to the variables, as well. This new expansion separates the r-direction and z-direction dependencies of each variable from the  $\theta$ -direction and time dependencies. In the example expansion shown as Equation 4.20, the new variable representing only the r-direction and z-direction dependencies is marked with a “prime” symbol. This expansion assumes a periodic form for the  $\theta$ -direction dependencies, which is sensible, since the cylindrical and annular systems being considered are indeed periodic in the  $\theta$ -direction. The nature of the periodicity in the  $\theta$ -direction is described by an azimuthal wave number, called  $m$ . Note that this wave number is dimensionless since it arises from dimensionless variables. The time dependence of each variable is assumed to have an exponential behavior. This exponential behavior with respect to time is governed by an inverse time constant, called  $\sigma$ .  $\sigma$  is dimensionless since it arises from dimensionless equations; if unscaled, its units would be (1/time). Using pressure as an example, the form of the expansion is

$$p_1 = p'_1(r, z) e^{im\theta + \sigma t} . \tag{4.20}$$

The form of  $\theta$ -direction dependency assumed in the expansion can be used because the periodic spatial dependence of the system in the  $\theta$ -direction can be represented by a series of sines and cosines. When the system of modeling equations is subjected to a perturbation ( $\varepsilon$ ), the perturbation may either grow, resulting in the onset of flow, or it may die out if the system is not at critical or supercritical conditions. The value of  $\sigma$  is an indicator of the system's response to a given perturbation. It should be noted that in certain cases, for which the system oscillates between convective flow patterns, the value of  $\sigma$  is imaginary. It can be mathematically shown, however, that  $\sigma$  is strictly real for the non-oscillatory cases considered in this research. If a disturbance applied to the system dies out, meaning that the system is stable, then  $\sigma$  has a negative value. If the system is unstable, and will flow when subjected to a perturbation,  $\sigma$  is positive. At marginal stability, however, when the system initially becomes unstable, the system is independent of time and the value of  $\sigma$  is 0. The fact that  $\sigma = 0$  at marginal stability allows the elimination of all time-derivative terms in the modeling equations once this expansion is applied. The final forms of the modeling equations (including all three components of the momentum equation, the energy equation, the continuity equation, and the boundary conditions), with this expansion applied, and with the "prime" symbols dropped from the newly defined variables, are

$$\begin{aligned}
0 = & -\frac{\partial p_1}{\partial r} + \\
& e^{B(\Delta T)T_0} \left[ \left[ \frac{\partial^2}{\partial r^2} + \frac{1}{r} \frac{\partial}{\partial r} + \frac{\partial^2}{\partial z^2} - \frac{(m^2+1)}{r^2} \right] v_{1_r} - \right. \\
& \left. \left[ \frac{2im}{r^2} \right] v_{1_\theta} \right] +
\end{aligned} \tag{4.21}$$

$$(B(\Delta T)e^{B(\Delta T)T_0} \frac{\partial T_0}{\partial z}) \left[ \frac{\partial v_{1_r}}{\partial z} + \frac{\partial v_{1_z}}{\partial r} \right],$$

$$\begin{aligned}
0 = & -\frac{im}{r} p_1 + \\
& e^{B(\Delta T)T_0} \left[ \left[ \frac{\partial^2}{\partial r^2} + \frac{1}{r} \frac{\partial}{\partial r} + \frac{\partial^2}{\partial z^2} - \frac{(m^2+1)}{r^2} \right] v_{1_\theta} + \right. \\
& \left. \left[ \frac{2im}{r^2} \right] v_{1_r} \right] +
\end{aligned} \tag{4.22}$$

$$(B(\Delta T)e^{B(\Delta T)T_0} \frac{\partial T_0}{\partial z}) \left[ \frac{\partial v_{1_\theta}}{\partial z} + \frac{im}{r} v_{1_z} \right],$$

$$\begin{aligned}
0 = & -\frac{\partial p_1}{\partial z} + \\
& e^{B(\Delta T)T_0} \left[ \left[ \frac{\partial^2}{\partial r^2} + \frac{1}{r} \frac{\partial}{\partial r} - \frac{m^2}{r^2} + \frac{\partial^2}{\partial z^2} \right] v_{1_z} \right] +
\end{aligned} \tag{4.23}$$

$$(B(\Delta T)e^{B(\Delta T)T_0} \frac{\partial T_0}{\partial z}) \left[ 2 \frac{\partial v_{1_z}}{\partial z} \right] + \frac{\alpha L_z^2 g(\Delta T)}{\nu \bar{v}} T_1,$$

$$0 = -\frac{L_z \bar{v}}{\kappa} \frac{\partial T_0}{\partial z} \bar{v}_1 + \left[ \frac{\partial^2}{\partial r^2} + \frac{1}{r} \frac{\partial}{\partial r} + \frac{\partial^2}{\partial z^2} - \frac{m^2}{r^2} \right] T_1, \quad (4.24)$$

$$0 = \left[ \frac{\partial}{\partial r} + \frac{1}{r} \right] v_{1r} + \left[ \frac{im}{r} \right] v_{1\theta} + \left[ \frac{\partial}{\partial z} \right] v_{1z}, \quad (4.25)$$

$$v_{1r} = v_{1\theta} = v_{1z} = 0 \text{ at } z = 0, \quad (4.26)$$

$$T_1 = 0 \text{ at } z = 0, \quad (4.27)$$

$$v_{1r} = v_{1\theta} = v_{1z} = 0 \text{ at } z = L_z, \quad (4.28)$$

$$T_1 = 0 \text{ at } z = L_z, \quad (4.29)$$

$$v_{1r} = v_{1\theta} = v_{1z} = 0 \text{ at } r = R_o, \quad (4.30)$$

$$\frac{\partial T_1}{\partial r} = 0 \text{ at } r = R_o, \quad (4.31)$$

and, when considering an annular system,

$$v_{1r} = v_{1\theta} = v_{1z} = 0 \text{ at } r = R_i, \quad (4.32)$$

$$\frac{\partial T_1}{\partial r} = 0 \text{ at } r = R_i \quad (4.33)$$

are needed.

At this point, two important dimensionless groups which show up in the motion equation are  $F_0$  (see Equation 4.6) and

$$\Omega = B(\Delta T) e^{B(\Delta T)T_0} \frac{\partial T_0}{\partial z}. \quad (4.34)$$

Now, the entire collection of modeling equations (Equations 4.21 – 4.33) may be simultaneously, numerically solved on a computer as an eigenvalue problem, in which the

eigenvalue is  $\Delta T$ . Since  $\sigma$  has been set equal to 0, the problem is being solved at the critical point for the onset of convection, and so the  $\Delta T$  value to be determined is the critical vertical temperature difference for convection, or  $[\Delta T]_{\text{crit}}$ . How exactly the solution for the  $[\Delta T]_{\text{crit}}$  is carried out is the topic of the next chapter.

Notice that the Prandtl number ( $\nu/\kappa$ ) does not appear in any of these equations. This may be surprising since one might expect that ratio of thermophysical properties to play a role in determining the critical conditions for convection. Now, recall that in Chapter 1 it was shown that the graph of critical Rayleigh number versus aspect ratio, for different azimuthal wave numbers, was identical for any system, regardless of the system's thermophysical properties. This interesting fact can be clearly explained at this point. The kinematic viscosity and thermal diffusivity of the system affect how quickly disturbances may die out or grow. Thus, before the onset of convection, their values make  $\sigma$  more or less negative depending on how stable the system is, and after the onset of convection, their values make  $\sigma$  more or less positive depending on how rapidly a destabilizing disturbance grew and how strongly the system is convecting in response to it. Precisely at the onset of convection, however, which is the condition at which the modeling equations are being solved, the system is independent of time ( $\sigma = 0$ ), and so the thermophysical properties play no role in determining the critical conditions for convection. If, rather than simply changing the thermophysical properties of the fluid, the insulating boundary conditions on temperature at the radial walls were changed to conducting boundary conditions, the graph of the critical Rayleigh number versus aspect ratio would change (as explained in Chapter 1, the critical vertical temperature differences for convection are lower when insulating radial walls are considered rather than conducting radial walls).

## CHAPTER 5 SPECTRAL SOLUTION METHOD

The goal of this chapter is to explain the spectral solution method used for computations in this research. The method is introduced and described in Section 5.1. Section 5.2 focuses on the application of the method.

Rearranging the set of modeling equations to be solved numerically as an eigenvalue problem for  $\Delta T$  is not too difficult. To do so, one must isolate the term of the z-direction-component of the momentum Equation 4.23 which includes  $T_l$ . What is meant by isolating that term is arranging the equation so that that term is on the side of the equation opposite from all of the other terms. Supposing the side of the equation where the  $T_l$  term is placed is chosen to be the right-hand-side of the equation, then the remaining terms of the z-direction-component of the momentum equation, and all nonzero terms of all of the other domain equations and boundary conditions should be kept on the left-hand-sides of those equations. In general, what is being done here is that the problem is being recast in the form of a generalized eigenvalue problem for  $\Delta T$ . The form of this generalized eigenvalue problem is

$$\bar{\bar{A}}\bar{X} = \lambda\bar{\bar{B}}\bar{X} . \tag{5.1}$$

Here,  $\bar{\bar{A}}$  is the matrix containing the coefficients of the velocity components, temperature, and pressure from the left-hand-sides of the domain equations and boundary conditions.  $\bar{\bar{B}}$ , as one would imagine, is the matrix of the coefficients of the velocity components, temperature, and pressure from the right-hand-sides of the set of modeling equations.  $\bar{X}$  is the eigenvector; it is a column-vector including all three velocity components, temperature, and pressure. From this point onward, the subscript “1”s used to indicate perturbed variables will be discarded, as nearly all variables referred to will be perturbed

variables. The only exceptions to this would be the base state variables, which, for this reason, will still be denoted by a subscript “0” in all locations. The form of  $\bar{X}$  is

$$\bar{X} = \begin{bmatrix} v_r \\ v_\theta \\ v_z \\ T \\ P \end{bmatrix}. \quad (5.2)$$

$\lambda$ , of course, is the eigenvalue, which is  $\Delta T$ . Arranging the system of modeling equations in this form is straightforward when the variation of viscosity with temperature is not being considered. For the non-constant viscosity case, however,  $\Delta T$  is present in more locations than just the coefficient of  $T_l$  in the  $z$ -direction-component of the momentum equation; it is also present as an exponent in several terms. These terms, though, may be kept on the left-hand-side of the modeling equations rather than being placed on the right-hand-side of Equation 5.1. If the equations are arranged in this way,  $\Delta T$  can be determined by an iterative approach. In this iterative approach, a value must first be chosen for  $T_t$ , the temperature at the top of the fluid layer. In all experiments done for this research, this temperature was kept constant at 30.0 °C, so that value was always substituted for  $T_t$  in the calculations. Next, a guess-value, which will be called  $[\Delta T]_{\text{guess}}$ , is substituted for  $\Delta T$  on the left-hand-side of Equation 5.1. Then, the eigenvalue ( $\Delta T$ ) on the right-hand-side of Equation 5.1 is solved for, and then its value is used to update the  $[\Delta T]_{\text{guess}}$  value on the left-hand-side of Equation 5.1, and so on. The procedure is repeated until convergence, which occurs quickly. Since  $T_R$  and  $\mu_R$  are dependent on the vertical temperature gradient prior to the onset of convection, their values are updated as  $[\Delta T]_{\text{guess}}$  is updated. Note that updating the  $[\Delta T]_{\text{guess}}$  value on the left-hand-side of Equation 5.1 represents updating the value of viscosity, through its exponential temperature dependence.

Also, note that in the case where the variation of viscosity with temperature is not accounted for, the viscosity value at 35.0 °C, which is given in Appendix A, is used throughout the calculation.

### 5.1 Explanation of the Method

Once the system of modeling equations has been written in the form of Equation 5.1, it can be used to numerically approximate the critical vertical temperature difference for convection, and the onset flow pattern. As is typical of numerical solution methods, the first step is to consider discretized versions of the modeling equations, which describe the behavior at a collection of individual points in the system as an approximation of the full behavior of the system. This means that each variable is written as a vector containing the values of that variable at a set of points within the system. For example, a cylindrical system could be discretized into sets of points (or “nodes”) in the r-direction and z-direction as shown in Figure 5-1. Of course, the subscripted numbers here have nothing to do with the subscripted numbers that appeared during linearization in Chapter 4; they simply indicate the spatial arrangement of the nodes.

In this case, the cylinder was discretized into rows of four nodes in the r-direction, and columns of four nodes in the z-direction. Clearly, these sets of nodes in the r-direction and z-direction form a grid of nodes in which the location of any node can be specified with an index for the r-direction and an index for the z-direction. For this reason, the discretization nodes are also referred to as “grid points.” Either direction could have been discretized into any number of nodes. Of course, considering a larger number of nodes leads to a more accurate discretized model. The numbers of nodes created in the r-direction and the z-direction are decided by the selection of parameters called  $N_r$  and  $N_z$ , respectively. For the example above,  $N_r = 3$  and  $N_z = 3$ . Note that discretizing the r-direction and z-direction means that r and z are written as vectors

now rather than scalars. In general, the sets of nodes in the r-direction and z-direction, respectively, can be written as

$$\vec{r} = \begin{bmatrix} r_0 \\ r_1 \\ r_2 \\ \vdots \\ r_{N_r} \end{bmatrix}, \quad (5.3)$$

$$\vec{z} = \begin{bmatrix} z_0 \\ z_1 \\ z_2 \\ \vdots \\ z_{N_z} \end{bmatrix}. \quad (5.4)$$

Due to the inclusion of  $r_0$  and  $z_0$ , the numbers of nodes in the r-direction and z-direction are actually  $(N_r + 1)$  and  $(N_z + 1)$ , respectively. It should be mentioned that, in this research, the treatment of the  $\theta$ -direction was much simpler than the discretization applied to the r-direction and z-direction, due to the periodic form assumed for  $\theta$ -direction dependencies; the treatment of the  $\theta$ -direction will be discussed later. For now, the reader is free to imagine that the discussion here pertains to simply systems axisymmetric in the  $\theta$ -direction, even though, in actuality, the treatment of the  $\theta$ -direction is such that everything presented here applies to systems of any azimuthal periodicity.

As indicated by Figure 5-1, when considering a system in two or more spatial dimensions, the indices of the nodes in the r-direction and z-direction may be thought of as indices corresponding to different planes slicing through the system, normal to the r-direction

and the z-direction, respectively. Thus, discretizing the r-direction into  $(N_r + 1)$  nodes and the z-direction into  $(N_z + 1)$  nodes divides the system into a grid of nodes that includes a total of  $((N_r + 1) * (N_z + 1))$  nodes. Again, note that the computational treatment of the  $\theta$ -direction has not yet been addressed; this means that the discretized form of the system being discussed at the moment is only one plane in the  $\theta$ -direction. Given this form of discretization, every variable in the system must be written as a vector of its scalar values at every node of the discretized system. Temperature, for example, would be written in discrete form as shown in Equation 5.5. To allow a shortened, more clear representation on paper, Equation 5.5 will show  $\vec{T}$  in the transposed arrangement; note that it is actually a column-vector like  $\vec{r}$  and  $\vec{z}$ . The transposed form of the discretized temperature is

$$\vec{T}^T = [T_{r_0, z_0}, T_{r_1, z_0}, \dots, T_{r_{N_r}, z_0}, T_{r_0, z_1}, T_{r_1, z_1}, \dots, \dots, T_{r_{N_r}, z_1}, \dots, T_{r_0, z_{N_z}}, T_{r_1, z_{N_z}}, \dots, T_{r_{N_r}, z_{N_z}}] \quad (5.5)$$

The raised ellipsis in Equation 5.5 indicates the continuation of this row-vector on the next line. The discretization nodes, although they may appear to be so in Figure 5-1, are not necessarily evenly distributed in the system. In fact, it can be quite beneficial to use nodes which are not evenly spaced. The sets of nodes used in this research are not evenly spaced; they are called the Gauss-Chebyshev-Lobatto grid points and the Gauss-Radau grid points (Trefethen 2000). Both sets of grid points are more highly clustered near the boundaries of the system than near the center of the system. It is highly beneficial to use these sets of clustered grid points as opposed to evenly spaced grid points because the clustered grid points allow much quicker and more accurate numerical convergence. Using these sets of grid points is also beneficial because, in the systems considered in this research, much of the important convective flow behavior

occurs near the edges of the system, and using sets of grid points more clustered near the edges of the system thus allows the convective behavior of the system to be more easily captured by the discretized modeling equations.

Gauss-Chebyshev-Lobatto grid points are a set of points spanning the range  $[-1,1]$  (including the endpoints at both  $-1$  and  $1$ ), and so the actual distances within the system must be rescaled in order to fit this range. The set of Gauss-Radau grid points, however, spans the range  $(-1,1]$ , meaning that it does include the endpoint at  $1$ , but does not include the endpoint at  $-1$ . Simple diagrams showing the general appearance of the Gauss-Chebyshev-Lobatto and Gauss-Radau sets of grid points, considering the  $r$ -direction, and considering seven grid points, are shown below as Figure 5-2.

To show how to determine the exact spacing of these clustered sets of grid points, the equations to generate the Gauss-Chebyshev-Lobatto and Gauss-Radau points are shown below, considering the discretization of the  $r$ -direction. The equation to generate the Gauss-Chebyshev-Lobatto points is

$$r_j = -\cos\left(\frac{j\pi}{N_r}\right), \quad j = 0,1,\dots,N_r, \quad (5.6)$$

and the equation to generate the Gauss-Radau points is

$$r_j^* = \cos\left(\frac{2\pi j}{2N_r + 1}\right), \quad j = 0,1,\dots,N_r. \quad (5.7)$$

A negative sign has been added to the Gauss-Chebyshev-Lobatto equation so that that set of points corresponds with Figure 5-1. For the Gauss-Radau points,  $r_j$  has been marked with a superscripted “\*” to indicate that the order of the set of points generated by Equation 5.7 actually needs to be reversed so that the points correspond with Figure 5-1.

In all calculations done for this research, the Gauss-Chebyshev-Lobatto grid points were used in discretizing the z-direction. In calculations for annular systems, the Gauss-Chebyshev-Lobatto grid points were used for the discretization of the r-direction, as well. In calculations for cylindrical systems, however, Gauss-Radau grid points were used in discretizing the r-direction. The reason for this will be explained now. The discretization in the r-direction is done along the radius of the cylinder, and not the diameter. In the set of modeling equations for the cylindrical system, though, there are no boundary conditions at  $r = 0$  (the interior endpoint of the discretization in the r-direction). Thus, including that location in the discretization of the r-direction would cause computational problems. This difficulty can be dealt with by excluding the location  $r = 0$  from the discretization. The use of Gauss-Radau grid points for the discretization in the r-direction accomplishes this because this set of grid points excludes one endpoint.

Given that all variables must be written as vectors of their scalar values at every node of the discretized system, in the manner shown in Equation 5.5, it is clear that the eigenvector,  $\vec{X}$ , will actually be a concatenated column-vector comprised of the column-vectors for each system variable. This means that it is a vector in which the smaller column-vectors for each system variable are vertically arranged above and below one another, head-to-tail. In the discretized form of the problem, the matrices  $\vec{A}$  and  $\vec{B}$  of Equation 5.1 are actually large matrices comprised of many smaller matrices which operate on the discretized variables in  $\vec{X}$  in accordance with the modeling equations. Each row of submatrices within  $\vec{A}$  and  $\vec{B}$  represents a different domain equation or boundary condition. Each submatrix in a row of submatrices representing a domain equation must operate on all grid points in the system, whereas each submatrix in a row of submatrices representing a boundary condition operates on only the grid

points on the boundary where the condition is enforced. A diagram illustrating the general layout of the matrices and vectors of the discretized, generalized eigenvalue problem is shown below as Figure 5-3.

All differential operators in the modeling equations must be expressed in matrix-form so that they may operate on the discretized variables. The differentiation matrices can be derived from polynomial interpolation equations. When taking derivatives in a direction that was discretized with Gauss-Chebyshev-Lobatto grid points, the differentiation matrix is different than the one that would be used for taking derivatives in a direction that was discretized with Gauss-Radau grid points. An example differentiation matrix, for r-direction differentiation on Gauss-Chebyshev-Lobatto grid points (as given by Equation 5.6) with  $N_r = 3$  is

$$D_{r,N_r=3} = \begin{bmatrix} -3.1667 & 4.0000 & -1.3333 & 0.5000 \\ -1.0000 & 0.3333 & 1.0000 & -0.3333 \\ 0.3333 & -1.0000 & -0.3333 & 1.0000 \\ -0.5000 & 1.3333 & -4.0000 & 3.1667 \end{bmatrix}, \quad (5.8)$$

where the subscript of  $D_r$  reflects the fact that this matrix is for  $N_r = 3$ .

More details about how to obtain differentiation matrices and how to set up and apply the spectral solution method being used in this research can be found in a helpful book by Trefethen, called *Spectral Methods in MATLAB* (2000).

The discretization and discrete problem formulation described so far are an accurate description of how to treat the system of modeling equations on a given plane normal to the azimuthal direction (an r-z plane). Dealing with the  $\theta$ -direction dependence of the physical system is mathematically quite simple because of the periodicity of the system in the  $\theta$ -

direction. Recall that the periodic  $\theta$ -direction dependence of the system was represented in the form shown in Equation 4.20. This results in the presence of the azimuthal wave number,  $m$ , in the final set of modeling equations. To account for the  $\theta$ -direction dependence of the physical system, one must simply assume a value for  $m$ . To choose a value for  $m$ , of course, is to assume the exact periodic form (number of periods in the  $\theta$ -direction) of the convective flow pattern at onset. If, for example,  $m$  is assumed to be equal to 2, then the onset flow pattern being sought is one which repeats twice as one progresses a single cycle through the fluid layer in the  $\theta$ -direction. If  $m = 0$  is assumed, then the onset flow pattern is one which does not vary in the  $\theta$ -direction at all; the  $m = 0$  case is axisymmetric in the  $\theta$ -direction.

Once a value is set for  $m$ , and thus the particular periodic form of the onset flow pattern has been assumed, the discrete system of modeling equations in matrix-form (Figure 5-3) can be solved for the eigenvalue,  $\Delta T$ . This can be done numerically with an eigenvalue solver (for example, in MATLAB<sup>®</sup>) that accommodates generalized eigenvalue problems.

Note that, in this research, the left-hand-side matrix (the  $\bar{\bar{A}}$  matrix in Figure 5-3) was not of full rank. Another way of saying this is that the set of eigenvalues of the  $\bar{\bar{A}}$  matrix, itself, included some eigenvalues which were equal to zero. MATLAB<sup>®</sup> was selected as the software to be used in performing the computations for this research. The MATLAB<sup>®</sup> generalized eigenvalue solver used in this research, like most other generalized eigenvalue solvers that the author has encountered, required that the  $\bar{\bar{A}}$  matrix be of full rank. Consequently, if the matrices of discretized modeling equations were directly fed into a generalized eigenvalue solver, then the output would include several spurious values. The reasons for the appearance of the spurious values related to the redundancy of boundary conditions at some points. To read more about this type of complication, the reader is asked to see the 1993 work of Labrosse (Labrosse 1993). In

order to eliminate spurious values from the output of the eigenvalue calculation, the  $\bar{\bar{A}}$  matrix was put through a pre-conditioning process involving singular-value decomposition. In this process, the  $\bar{\bar{A}}$  matrix was decomposed into three matrices by singular-value decomposition, then the rows in the matrices corresponding to any eigenvalues equal to zero could be located, and finally those rows were filtered out of further computations.

The critical temperature difference and flow pattern at the onset of convection can be determined by comparing the  $\Delta T$  values (eigenvalues) obtained for a range of different  $m$  values. When making this comparison, the lowest  $\Delta T$  value corresponds to the  $m$  value for which the fluid layer is most unstable to buoyancy forces. The lowest  $\Delta T$  value and the corresponding  $m$  value, thus, represent the critical temperature difference and flow pattern at the onset of convection, respectively. Note, also, that in order to account for the variation of viscosity with temperature, it is necessary to use an iterative procedure (as described earlier in this chapter) to obtain the  $\Delta T$  value corresponding to each  $m$  value.

A flow-diagram displaying the general procedure carried out in MATLAB<sup>®</sup> to solve the system of modeling equations for onset conditions is given in Appendix D. A set of MATLAB<sup>®</sup> programs were created to be used in the calculations for this research, and some examples of these programs are given in Appendix E.

## 5.2 Application of the Method

As mentioned, considering a larger number of nodes makes the discretized model more accurate. If the number of discretization nodes used to model the physical system were small enough, an inaccurate critical temperature difference would be obtained from the eigenvalue calculation. If the number of nodes were, then, increased further and further, the critical temperature difference results given by the eigenvalue calculation would progressively converge

toward the physically correct value. Eventually, when considering a sufficiently high number of discretization nodes, the critical temperature difference obtained would be the physically correct value, and further increases to the number of nodes considered would have no impact on the critical temperature difference result obtained. A nice quality of the spectral method used here, though, is that not too large a number of nodes are actually needed for the computational solution to converge to an accurate solution. In all computations done for this research, 17 nodes were used in the r-direction and in the z-direction; this was always more than enough nodes to obtain a converged solution. Convergence of the computational results was, of course, verified by repeating computations with even higher numbers of discretization nodes. To exemplify this convergence behavior, a table is given below (Table 5-1) which shows the convergence of critical temperature difference values obtained using the author's MATLAB<sup>®</sup> program. The example system considered for this convergence table is a fluid layer in a cylindrical container, with rigid, no-slip walls, insulated at the lateral boundary, and heated from below so as to facilitate Rayleigh convection. In particular, a case is being considered in which the size of the cylindrical system is such that the convective flow pattern at onset is a one-cell pattern, axisymmetric in the  $\theta$ -direction. The convergence of the critical temperature difference ( $[\Delta T]_{\text{crit}}$ ) is shown with respect to both  $N_r$  and  $N_z$ .

To confirm the validity of the set of computational programs written for this research, results obtained using the programs were checked against results for standard Rayleigh-Bénard problems (problems involving buoyancy-driven convection in systems heated from below) and some results obtained by other authors.

As one check of the validity of the computational programs, a comparison was made between the critical temperature difference results obtained for a two-dimensional, rectangular

case (x-direction and z-direction only) and a one-dimensional, rectangular case (z-direction only). In the two-dimensional case, the rectangular fluid layer was heated from below, with stress-free, insulated side walls, and constant-temperature, no-slip walls as the top and bottom boundaries of the layer. The distance between the side walls for the two-dimensional case is called  $L_x$ . In the one-dimensional case, the fluid layer was heated from below, was bounded at the top and bottom edges by constant-temperature, no-slip walls, and was unbounded in the lateral direction. In neither case was the variation of viscosity with temperature considered. The two-dimensional case with stress-free side walls was expected to produce exactly the same critical temperature difference results as a corresponding one-dimensional case, in which the system had the same vertical depth as the two-dimensional case. As Table 5-2 shows, it did. At first it may appear unusual that the one-dimensional calculation could produce two different critical temperature difference results for the same vertical depth ( $L_z = 7.2$  mm). The reason this is possible has to do with the way the one-dimensional calculation is carried out. As explained in Chapter 1, a two-dimensional system with lateral walls can only physically accommodate a certain set of onset flow patterns, which is dependent on the lateral width of the system. Thus, if the critical temperature difference result for a two-dimensional system with lateral walls is to be compared with the result for a corresponding one-dimensional calculation, it is only the disturbances of proper shape and size to induce these physically admissible onset flow patterns which may be considered in the one-dimensional calculation. It is because of this that the critical temperature difference results obtained from the one-dimensional calculation for the two cases in which  $L_z = 7.2$  mm are different. Now that results are being shown for systems of specified depths and boundary conditions, it is a good time to mention that the fluid used in all experiments and calculations for this research is Dow Corning 200<sup>®</sup> 1 Stoke silicone oil. Thus,

its thermophysical properties are used in all calculations presented in this paper. A list of these thermophysical properties is given in Appendix A. The dependence of temperature on the viscosity of the oil was determined using viscosity measurements taken with a Cole-Parmer<sup>®</sup> 98936 series viscometer. The exponential equation for the viscosity of the oil as a function of temperature is included in Appendix A, as well as a description of the manner in which viscosity measurements were obtained. Except for the viscosity, which was measured as described, the thermophysical properties of the silicone oil were based on information provided by Dow Corning.

As an initial check of the ability of the computational programs to model cylindrical systems, critical temperature difference results were computed for buoyancy-driven convection in a cylindrical fluid layer, and compared to the results given in a 1990 publication by Hardin et al. (Hardin, Sani, Henry, & Roux 1990). The particular system considered for this comparison was a layer of silicone oil in a cylindrical container, heated from below, with no-slip walls at all boundaries, constant-temperature conditions at the top and bottom boundaries, and insulation at the radial wall. Again, the variation of viscosity with temperature was not considered. Hardin et al. give several critical temperature difference results for this system, as well as the corresponding flow patterns. A comparison of the results produced by the author's computations for this system with those of Hardin et al. is given in Table 5-3. These comparisons show the validity of the MATLAB<sup>®</sup> programs written for the computations in this research. The results of Hardin et al. were given in terms of the dimensionless Rayleigh number, so in order to compare with them, the author's critical temperature difference results in this table have been re-expressed in terms of the Rayleigh number, as well (as shown in Equation 1.1). Since the variation of viscosity with temperature was not considered in this case, the viscosity value used in the

computation was simply the constant viscosity value at 35 °C given in Appendix A. The aspect ratio is simply the ratio of the radius of the cylindrical container to the vertical height of the container ( $L_r / L_z$ ). The way in which convective flow patterns are named should be briefly discussed here, too. In general, they are named by their azimuthal wave number,  $m$ . For example, a ring-shaped pattern axisymmetric in the  $\theta$ -direction is called an  $m = 0$  pattern. Optionally, when considering cylindrical systems, the flow pattern may be referred to with a parenthetical notation, including two indices. A parenthetical system for naming the onset flow patterns in annular systems is given in Chapter 7. In the parenthetical notation for cylindrical systems, the first index is the azimuthal wave number and the second index represents the maximum number of convective rolls that can be counted across the diameter of the cylindrical test section. Diagrams to exemplify the use of this parenthetical notation for flow patterns in cylindrical systems are shown as Figure 5-4. The diagrams are taken almost directly from the 1995 paper by Zhao, Moates, and Narayanan (Zhao, Moates, & Narayanan 1995). In Figure 5-4, a top view of each flow pattern is given, and below the top view of each pattern is a side view of the same pattern. In the top views, the “X” indicates falling fluid and the “O” indicates rising fluid. Diagrams (a) and (c) in Figure 5-4 could simply be called  $m = 0$  patterns if the parenthetical notation were not being used; likewise, diagrams (b) and (d) could be called  $m = 1$  patterns.

Now, the method of obtaining computational results has been explained, and the validity of the computational method has been demonstrated. The computational results were compared with the results from experiments, and an explanation of the experimental apparatus and the manner in which experimental results were obtained is given in Chapter 6.

Table 5-1. Example of convergence of computed result with  $N_r$  and  $N_z$ .

$N_r$	$N_z$	$[\Delta T]_{crit}$ (°C)	$N_r$	$N_z$	$[\Delta T]_{crit}$ (°C)
3	13	6.55	13	3	Inf
4	13	5.55	13	4	5.42
5	13	5.60	13	5	5.55
6	13	5.59	13	6	5.60
7	13	5.60	13	7	5.60
8	13	5.60	13	8	5.60
9	13	5.60	13	9	5.60
10	13	5.60	13	10	5.60
11	13	5.60	13	11	5.60
12	13	5.60	13	12	5.60
13	13	5.60	13	13	5.60

Table 5-2. Comparison of rectangular, 2-D, no-stress results with rectangular 1-D results.

$L_x$ (mm)	$L_z$ (mm)	$[\Delta T]_{crit}$ (°C), 2-D, No-Stress	$[\Delta T]_{crit}$ (°C), 1-D
5	5	12.87	12.87
7.2	7.2	4.31	4.31
23	7.2	4.33	4.33
9	9	2.21	2.21

Table 5-3. Comparison of calculated cylindrical results with results of Hardin et al.

Predicted Flow Pattern, Author's Computation	Predicted Flow Pattern, Hardin et al.	Critical Rayleigh Number, Author's Computation	Critical Rayleigh Number, Hardin et al.
<b>Aspect Ratio: .75, <math>L_r = 4.5</math> mm, <math>L_z = 6</math> mm</b>			
(1,1)	(1,1)	2590	2592
<b>Aspect Ratio: 1, <math>L_r = 6</math> mm, <math>L_z = 6</math> mm</b>			
(0,2)	(0,2)	2260	2260
<b>Aspect Ratio: 1.5, <math>L_r = 9</math> mm, <math>L_z = 6</math> mm</b>			
(0,2)	(0,2)	1895	1895
<b>Aspect Ratio: 2.5, <math>L_r = 15</math> mm, <math>L_z = 6</math> mm</b>			
(0,4)	(0,4)	1780	1781

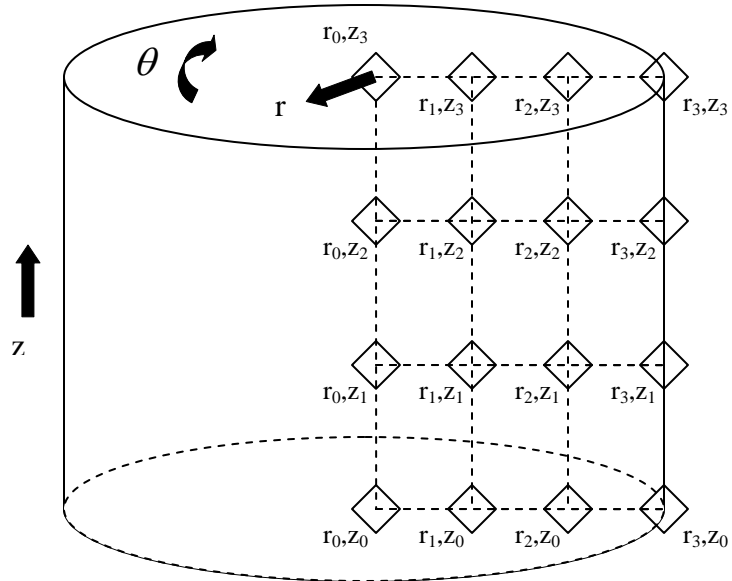


Figure 5-1. Discretization nodes in a cylinder.

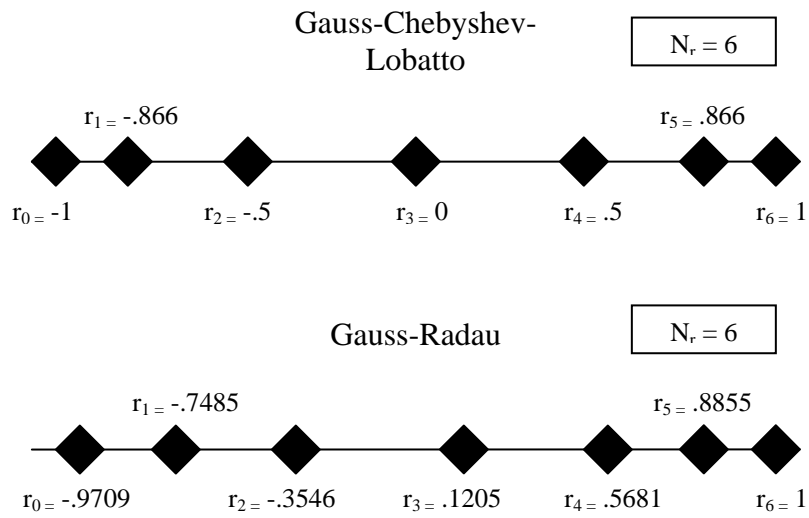


Figure 5-2. Example: grid point spacing.

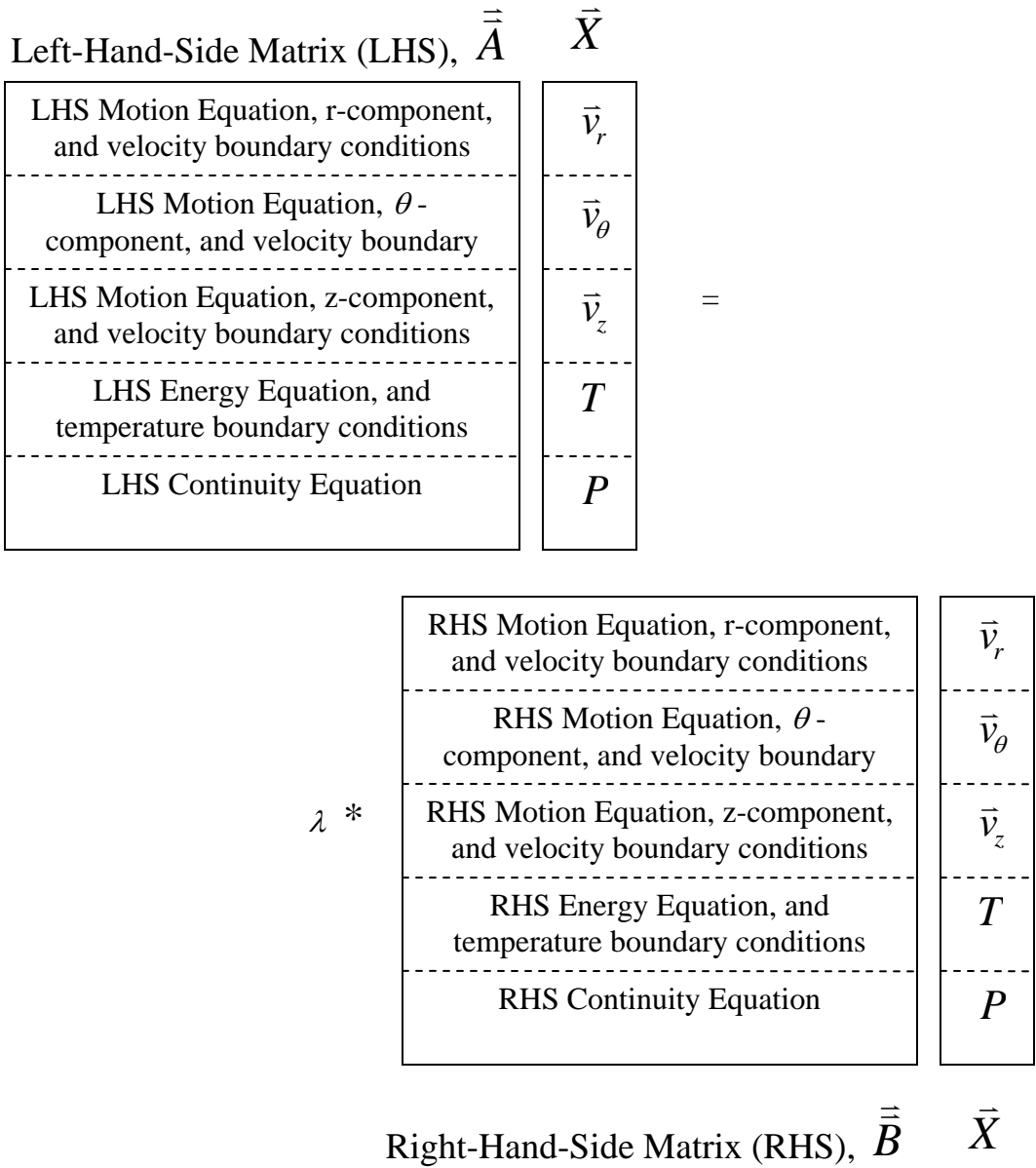


Figure 5-3. Diagram of matrix/vector arrangement of discretized problem.

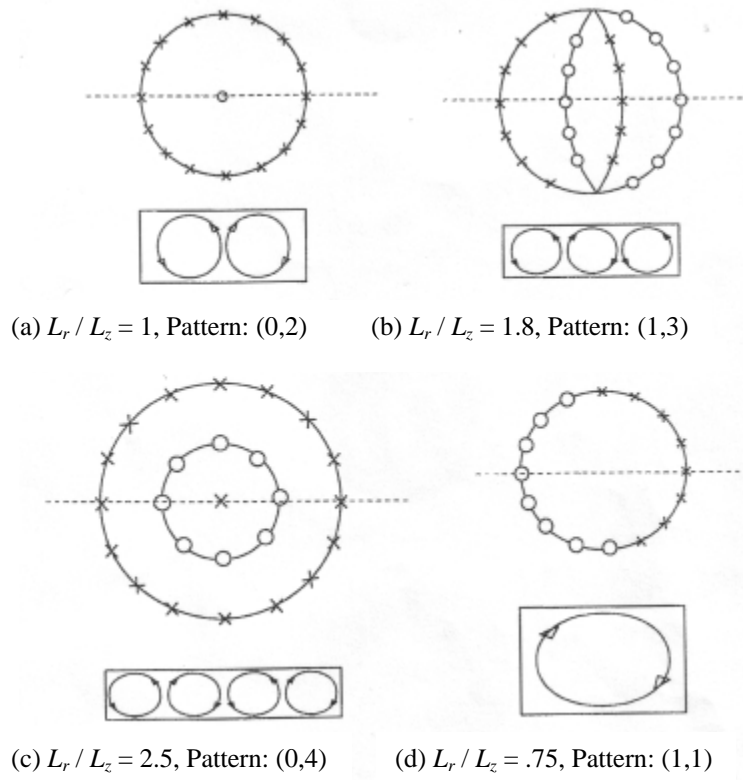


Figure 5-4. Examples of flow patterns and parenthetical notation for cylindrical systems.

## CHAPTER 6 EXPERIMENTAL DESIGN

After computational results were obtained in this research, they were compared with experimental results for systems identical to those considered in the computations. The apparatus which was designed to run experiments for this research is the subject of this chapter. Any possible errors associated with the apparatus and its measurements are discussed in Chapter 7.

### **6.1 Goals in Experimental Design**

There were several requirements made of the experimental system. One requirement was that the top and bottom temperatures of the fluid layer ( $T_t$  and  $T_b$ , respectively) were kept constant and uniform at desired values. By monitoring and controlling the top and bottom temperatures of the fluid layer, the vertical temperature difference across the fluid layer could be regulated. The radial walls in the experiments needed to be insulating so that heat did not escape the experimental test fluid into the air surrounding the experiment. Lastly, some means of flow visualization needed to be employed in order to determine when the fluid layer was or was not convecting, so that the critical conditions for the onset of convection could be determined. Below, the means by which these goals were accomplished are described.

### **6.2 Experimental Apparatus**

As mentioned, the test fluid in the experiments was Dow Corning 200<sup>®</sup> 1 Stoke silicone oil (thermophysical properties given in Appendix A). This fluid was chosen as the test fluid for this research because, for systems in the size range of those examined in this research, its thermophysical properties are such that the critical vertical temperature differences for convection were easily obtainable in experiments. The only thermophysical properties of the silicone oil which vary significantly with temperature are the density (enough to facilitate

Rayleigh convection) and viscosity. In the experimental apparatus, a lucite ring acted as the outer radial boundary of the silicone oil test section. A lucite middle-piece was added when the test section was annular. The dimensions of these lucite pieces, thus, set the sizes of the cylindrical and annular test sections. A copper plate at the top of a continuously stirred water bath was the bottom boundary of the test section, and a sapphire window at the bottom of a flow-through water bath was the top plate of the test section. To create heated-from-below conditions, the temperature of the bottom water bath was adjusted to certain set-point values while the top water bath was always kept at a constant, cooler temperature.

A process control computer, running a LabVIEW<sup>TM</sup> process control program written by the author, sent signals to turn a heater in the experiment on and off as needed in order to keep the bottom water bath at desired set-point temperatures. The process control system built for the experiments in this research will be further discussed in Section 6.3. The test section was insulated to prevent heat loss in the radial direction. To allow flow visualization, a small amount of aluminum tracer powder was mixed into the silicone oil. So that the flow behavior of the experimental system could be recorded and reviewed, a digital camcorder was mounted above the test section. More detailed descriptions of the components and features of the experimental apparatus, as well as some notes on the experimental start-up procedure, are given in the following subsections. A simple diagram of the apparatus is shown below as Figure 6-1, and a couple of photographs of the apparatus follow as Figures 6-2 and 6-3.

### **6.2.1 Test Section**

As mentioned, a lucite ring acted as the outer radial boundary of the test section which contained the silicone oil. The bottom boundary of the test section was a copper plate, which was the top surface of a stirred water bath that will be described shortly. The top boundary of the

test section was a sapphire window, which was the bottom surface of a flow-through water bath, which also will be described. The lucite rings typically ranged from about 15 mm to 30 mm in diameter and about 6 mm to 8 mm in height. The sets of experiments for cylindrical systems were run before the sets for annular systems; this procedure was used so that when the annular experiments were run, a nesting hole in the bottom copper plate could be used to anchor the bottoms of the lucite center-pieces, which were added to transform the cylindrical systems to annular systems. A reason for selecting lucite as the material from which to construct the outer-boundary rings and the center-pieces for the annular systems is its thermal conductivity, which is very close to that of the silicone oil (see Appendix A). Since the system of silicone oil being examined in this research was subjected to vertical temperature gradients, so, too, were the radial walls of the system. Thus, the fact that lucite has a thermal conductivity close to that of silicone oil made it an appealing choice as the material from which to construct the radial walls because it ensured that the vertical temperature gradients at the radial boundaries of the test section would not differ from those in the interior. This, and the fact that the lucite outer radial wall was surrounded by an insulating coating (which shall be further explained later), ensured that heat would not flow into or out of the silicone oil in the test section in the radial direction.

After placing the lucite ring onto the copper plate and before filling the test section with oil, a lucite clamp-piece was screwed down on top of the lucite test section ring to tighten the ring down against the copper plate (the clamp-piece screws into the bottom water bath). This was an important measure taken to prevent any leakage of air/oil at the bottom of the test section. Once the test section ring was tightened down to the copper plate, the test section was intentionally over-filled with silicone oil. This was done so that the sapphire plate of the flow-through top water bath could more easily be pressed down onto the top of the test section without

trapping air bubbles in the test section. A simple cross-sectional diagram of the test section is given below as Figure 6-4.

### **6.2.2 Bottom Temperature Bath**

The temperature at the bottom surface of the test section was kept constant and uniform by a constantly stirred water bath. The body of this bottom water bath was primarily lucite, but its top and bottom surfaces were copper plates. As mentioned, the top copper plate of this water bath acted as the bottom surface of the test section. The bottom copper plate rested on an electrical resistance heater, which was the means by which the temperature of the water in the bottom bath could be adjusted. This arrangement can be seen in Figure 6-1.

Three OMEGA<sup>®</sup> thermistors, which were attached to the underside of the top copper plate of this bath, measured resistances in the water at that location and sent the resistance data to a process control computer. The resistance data, based on calibration equations relating the thermistors' resistance readings to temperatures, was used to determine the temperature at each thermistor. Since the thermistors were on the underside of the bath's top copper plate, and copper is an extremely good heat conductor, they gave a very accurate reading of the temperature at the bottom of the test section. Depending on the readings of these thermistors, the heater at the bottom surface of the water bath was turned on or off in order to maintain a set-point value for the temperature at the bottom of the test section. The temperature of the bottom water bath typically needed to be in the range of 30.0 °C to 40.0 °C. The bottom water bath also contained a small magnetic stir-bar so that the water within the bottom bath could be mixed by a magnetic stirring plate, which was the surface upon which the electrical resistance heater rested. This mixing ensured that the temperature was uniform throughout this bath's top copper plate, which

was the bottom surface of the test section. The high thermal conductivity of copper also helped to ensure that the temperature was uniform at the bottom surface of the test section.

### **6.2.3 Top Temperature Bath**

The top surface of the test section was a sapphire window. This window was the bottom surface of a flow-through water bath. The body of the flow-through water bath was comprised of a thick aluminum bottom-piece and a transparent top-piece made of plexiglass; the aluminum bottom-piece had a circular section cut out of it, and that is where the sapphire window was located. The temperature of the flow-through water bath was set by water which flowed into it from a larger constant-temperature water bath. The larger constant-temperature bath was a NESLAB EX Series bath that was bought from Thermo Electron Corporation. The smaller, flow-through water bath had two water inlets and two water outlets, and this allowed a high volume of water to continuously pass over the top of the sapphire window. This, in turn, kept the sapphire window at a constant and uniform temperature by removing any heat conducted to it from the test section. If the temperature of the smaller, flow-through water bath, and thus the value of  $T_t$ , were to be changed, it was the set-point temperature of the larger NESLAB bath which needed to be adjusted. During all experiments for this research, the temperature at the top of the test section was maintained at 30.0 °C. The high thermal conductivity of sapphire (see Appendix A) ensured that the temperature throughout the sapphire window remained uniform. Another important property of the sapphire was its transparency; the transparency of the sapphire window and the transparency of the plexiglass top-piece of the flow-through water bath were necessary to allow flow visualization by means of aluminum tracer powder.

Two OMEGA<sup>®</sup> thermistors placed in the flowing water's inlet and outlet tubing were used to monitor the temperature within the flow-through water bath on the process control

computer. In the experiments for this research, these thermistors were used to verify that the temperature in the top water bath was indeed constant at 30.0 °C as desired.

#### **6.2.4 Insulation**

In the experiments for this research, it was important that heat was not lost from the test section to the surrounding air through the outer radial wall of the test section. To prevent this sort of heat exchange between the test section and the surroundings, a ring of foam insulation was placed snugly around the outer surface of each of the lucite rings used in the experimental runs. For the experiments on annular systems, at and near the onset of convection, no significant amount of heat would flow through the lucite center-pieces, and so it was not necessary to insulate them in any way.

#### **6.2.5 Flow Visualization**

A small amount of aluminum tracer powder was mixed in with the test fluid so that convective flow patterns in the fluid layer could be seen. As explained earlier, when the oil flow was horizontal, the aluminum particles aligned so that they reflected more light, making the regions of horizontal flow appear lighter in color; in regions where flow was vertical, the aluminum particles aligned such that they reflected less light, making those regions appear darker in color.

As mentioned, the sapphire top surface of the test section and the plexiglass top-piece of the upper flow-through water bath are both transparent, and this allowed the flow patterns in the test section to be easily observed from above the test section. The experiments often ran continuously for a day or more, so it was desirable to have a way of recording video footage of the flow behavior (or lack of such behavior) in the system for later viewing. To facilitate this, a digital camcorder, a television, and a video cassette recorder were included in the experimental

design. The digital camcorder, mounted directly above the test section, continuously captured a top-view image of the test section as the experiment was running. This image was sent to the video cassette recorder. The circuitry of the video cassette recorder was modified so that it could receive “Record” and “Stop” signals sent, through a relay, from the process control computer. The LabVIEW™ process control program then, periodically throughout the course of each experiment, sent a series of signals to the video cassette recorder, causing it to intermittently record for periods of about five seconds. The result of this was a conveniently reviewable time-lapsed video recording of the convective flow behavior observed over the entire experimental run. For real-time viewing of the flow behavior during the experiment, as well as viewing of the experimental video recordings, a television was connected to the video cassette recorder.

### **6.3 Process Control System**

The process control system built for running this experiment includes a process control computer equipped with a LabVIEW™ process control program, a circuit board to interface between the computer and the components of the experiment, and parts of the experimental apparatus, itself. The layout of the process control system is shown as Figure 6-5. In this diagram, the dashed connecting lines represent signals which are part of the process control system.

As Figure 6-5 shows, the process control computer collected data from thermistors placed in and near the top and bottom water baths, between which was the test section. Note that three OMEGA® thermistors were placed in the bottom, stirred water bath, and two OMEGA® thermistors were placed in the tubing near the top, flow-through water bath. Before the thermistor readings reached the computer, they were routed through a process control circuit board built for this research. The most important components in the large system of circuitry

were a set of National Instruments<sup>TM</sup> FieldPoint modules. The National Instruments<sup>TM</sup> FP-RTD-122 module was used to collect data from the thermistors, and the National Instruments<sup>TM</sup> FP-RLY-422 module was used to send process control signals to components of the experiment.

The readings from the thermistors are resistances, not temperatures. Thus, calibration equations stored in the process control computer needed to be used to convert the resistance data to temperature data. The thermistors were placed such that their readings accurately represented the values of  $T_i$  and  $T_b$ .

A LabVIEW<sup>TM</sup> process control program was written by the author, and saved on the process control computer. The process control program allowed its user to input a series of set-point values for the temperature of the lower bath, and thus, the temperature of the lower surface of the test section. Recall that the top, flow-through bath was kept at a constant temperature of 30.0 °C for all experiments. Additionally, the program allowed its user to input a time-segment value, which determined how long each set-point value for the bottom water bath temperature was maintained before the next set-point was targeted. Using “If” loops, this program sent “On” and “Off” signals to the heater beneath the bottom water bath, as needed, in order to keep that water bath at the current set-point temperature. To improve the ability of the process control program to keep the  $T_b$  value near the set-point, the process control could be set to behave in an advanced way (acting in anticipation of upcoming changes in  $T_b$ ) in a small range of temperatures around the  $T_b$  set-point. This small range of temperatures is called the “deadband.” While the experiments ran, the program also kept track of how much time had elapsed; depending on the amount of elapsed time, the program sent signals causing the video cassette recorder to record segments of the video image of the test section which was being continuously captured by the digital camcorder.

In addition to its powerful process control capabilities, LabVIEW™ also allows the creation of user-friendly front pages for process control programs. Thus, temperatures and temperature differences could easily be monitored on continuously updated graphs during experimental runs. A flow-chart giving a very general layout of the LabVIEW™ process control program and how it worked is given as Appendix F.

#### **6.4 Typical Experimental Procedure**

The purpose of this section is to briefly describe the typical procedure that was followed during the preparation of the experiment and the experimental runs for this research. First, a suitable mixture of silicone oil and the aluminum tracer powder needed to be made. When making this, it was important not to use too much tracer powder, so as not to significantly alter the properties of the silicone oil. Once this mixture was made, it was placed under the suction of a vacuum pump to remove any air bubbles in it.

The next step in preparing the experiment was to fill the top and bottom water baths with water and make sure that no air bubbles were present in them. Then, the bottom water bath (the copper plate on top of it, in particular) was made level, and the lucite ring (and middle-piece in annular cases) and lucite clamp-piece were assembled on top of it. Screws in the lucite clamp-piece were used to tighten the lucite ring on to the top copper plate of the bottom water bath. Next, the test section was filled with silicone oil. As mentioned earlier, the test section was purposely overfilled, which made it easier to avoid trapping air bubbles in the test section when placing the sapphire window of the flow-through water bath on top of the test section. Once the flow-through water bath was put in place, completing the assembly of the test section, temperature control could be initiated.

Usually, the bottom of the test section was immediately heated up enough to generate a strong convective flow under supercritical conditions. Then, the vertical temperature difference was gradually, incrementally decreased by decreasing  $T_b$ . Each vertical temperature difference was maintained for a time segment often in the range of 1 to 4 hours, depending on the time scales associated with the systems being examined. The time scales, of course, depended strongly on the sizes of the systems. The computational predictions could be used to aid in deciding approximately what ranges of vertical temperature differences to examine experimentally. Decreasing the vertical temperature difference, over time, resulted in the weakening of convective flow. At some point near the critical temperature difference, the flow pattern would likely be the pattern predicted computationally. Further decreasing the temperature difference in very small steps made it possible to determine the temperature difference at which convective flow stopped. Then, it was known that the last temperature difference value at which the fluid was convectively flowing was the critical temperature difference. To further check this experimental critical temperature difference result, the temperature difference could be increased slowly from the no-flow state to determine the temperature difference at which flow restarted. As an additional check of the experimental result, experimental runs were repeated multiple times.

The runs could easily last for longer than a day, depending on the time segment being used for each vertical temperature difference in the experiment. Thus, it was often helpful to make a video recording of the flow behavior at each vertical temperature difference and review the flow behavior using the video recording.

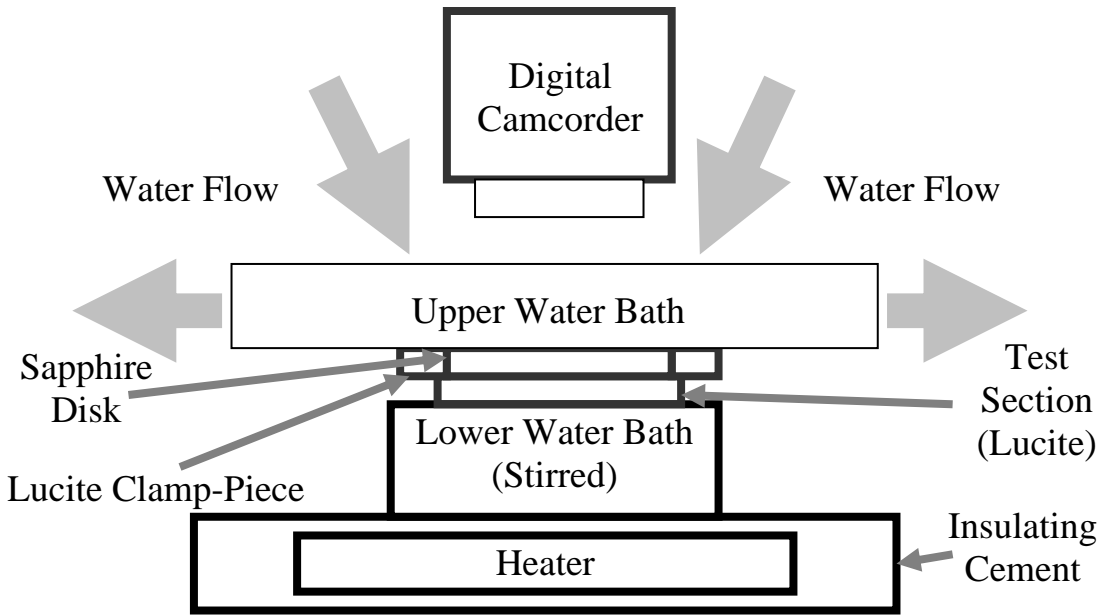


Figure 6-1. Simple experiment diagram.

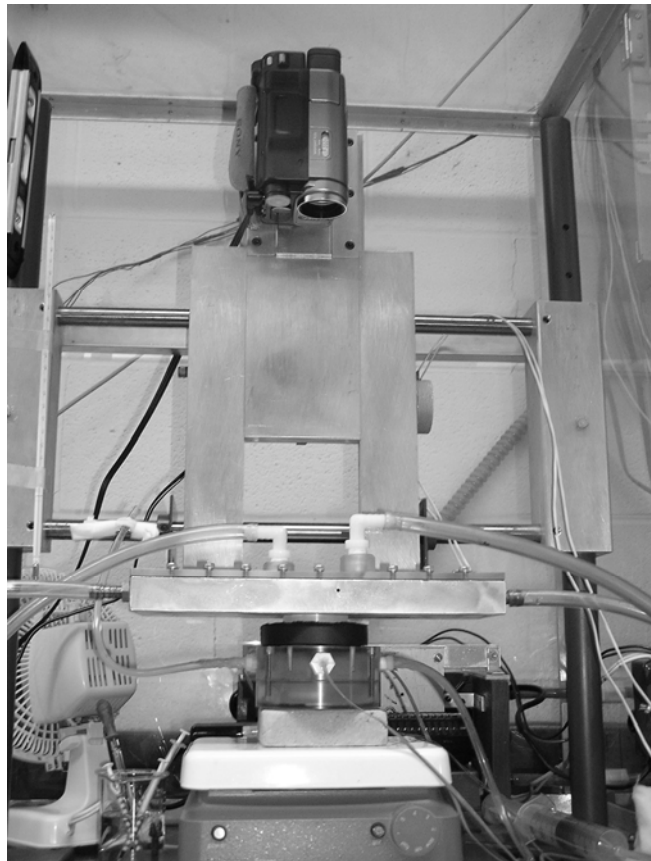


Figure 6-2. Photograph of experimental apparatus.

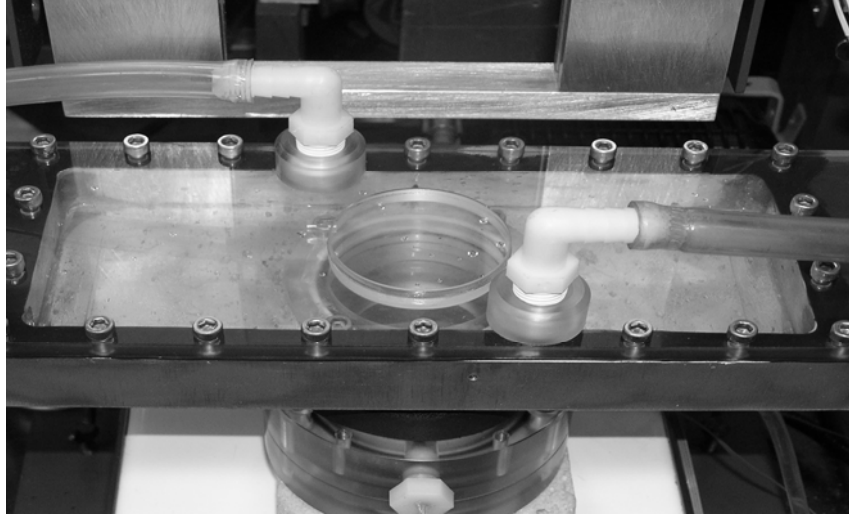


Figure 6-3. Photograph of flow-through top water bath of experimental apparatus.

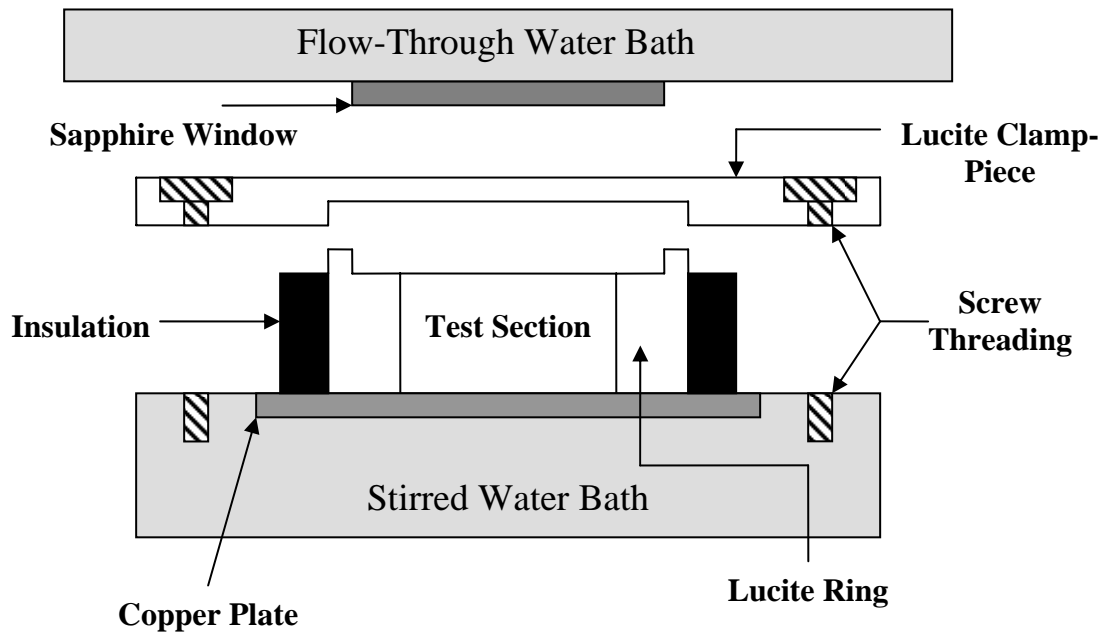


Figure 6-4. Cross-sectional diagram of test section.

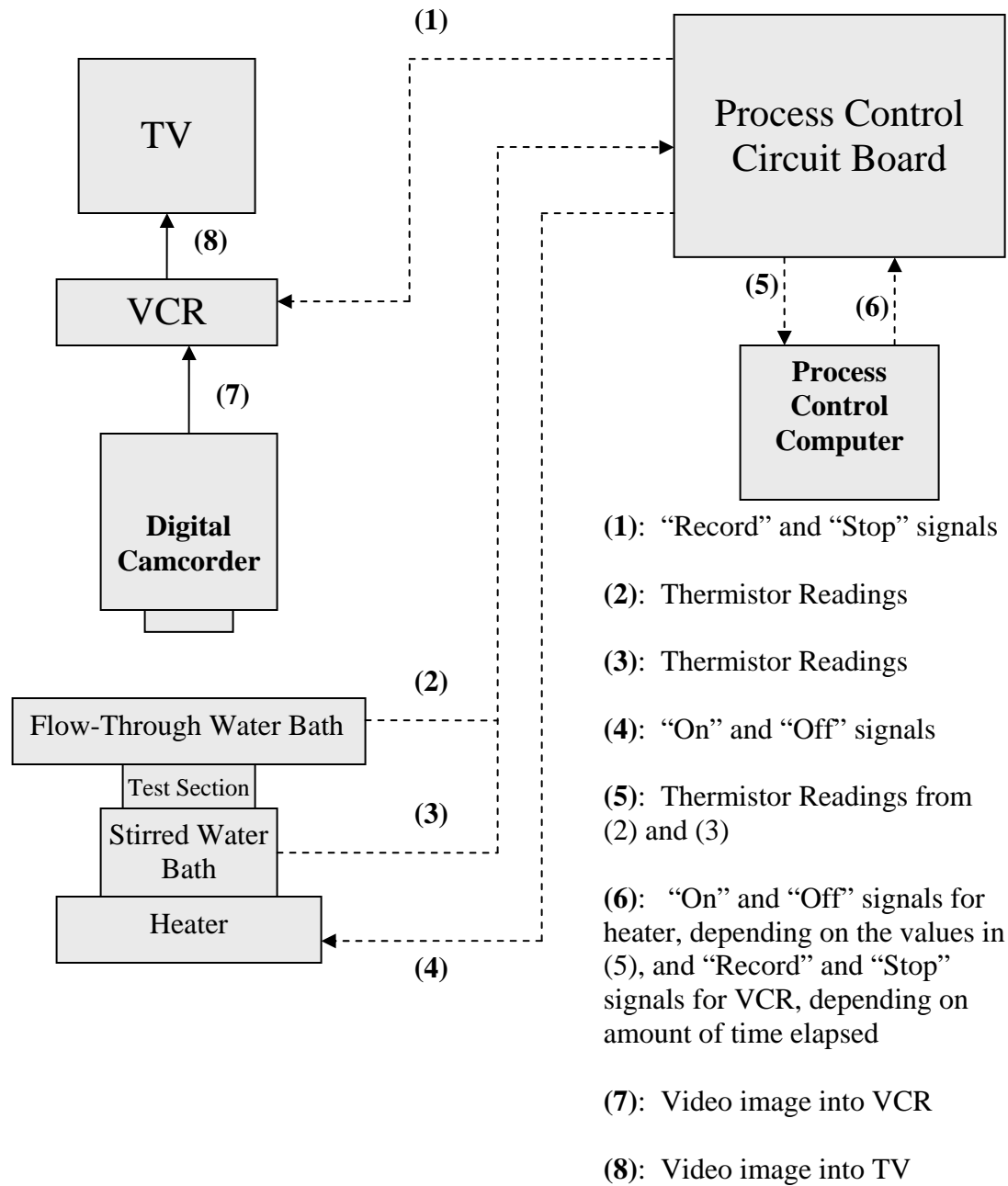


Figure 6-5. Process control system layout.

## CHAPTER 7 RESULTS AND DISCUSSION

In this research, the results that were sought through computations and experiments were the critical conditions for the onset of convection in the systems being studied. These conditions included the critical vertical temperature difference corresponding to the onset of convection, and the corresponding convective flow patterns. Results were obtained both from calculations in which the variation of viscosity with temperature was not accounted for, and from calculations in which it was. The results from these computations were then compared with results obtained experimentally for the same systems that the computations addressed. The test fluid considered in all computations and used in all experiments was Dow Corning 200<sup>®</sup> 1 Stoke silicone oil; its properties are given in Appendix A. Possible errors in the results are noted on the tables of results, and the sources and quantification of the errors are explained in Section 7.3.

### 7.1 Cylindrical Systems

This section presents the critical conditions for the onset of convection, determined computationally and experimentally, for cylindrical systems of three different sets of dimensions. The computational results are shown both for the case in which the variation of viscosity with temperature is included, and for the case in which it is not. Then, the experimental results are given. After that, the computational and experimental results are compared against each other.

#### 7.1.1 Constant Viscosity Computations: Cylinder

Since the top temperature of the test section was always kept constant at 30.0 °C, and the bottom temperature of the test section typically ranged from 30.0 °C to 40.0 °C, the constant viscosity value assumed for these calculations was the viscosity value for the oil at 35.0 °C, which is the mean value in the 30.0 °C – 40.0 °C temperature range. The kinematic viscosity of the oil at 35.0 °C is given in Appendix A. The results of the constant viscosity computations for

the three sets of cylindrical dimensions that were considered in experiments are given below as Table 7-1. In this table, the parenthetical notation for flow patterns in cylindrical systems, which was introduced in Chapter 5, is used again to describe the onset flow patterns. Remember that in this notation, the first index is the azimuthal wave number, and the second index is the maximum number of convective rolls that can be counted across the diameter of the cylindrical test section.

The experimental results corresponding to these calculations will be shown in Section 7.1.3. Carrying out the constant viscosity computation for the critical conditions at a wide range of aspect ratios yields the stability diagram shown as Figure 7-1. This diagram includes the stability curves for the onset flow patterns with  $m = 0, 1, 2, 3, 4,$  and  $5$ . Figure 7-2 is from the same stability diagram, but is a close-up of a small portion of the diagram that better shows the behavior in that region.

Notice that Figure 7-1 is much like the graph shown in Chapter 1 as Figure 1-10. Figure 1-10, though, was created simply by logically considering the physics and pattern selection behavior of buoyancy-driven convection in a cylindrical system. Figure 7-1 shows that, even after working through a computational solution to obtain a stability diagram for this system, the result matches what could be predicted based on physical reasoning alone. This diagram is valid for any constant viscosity cylindrical system regardless of the exact dimensions or thermophysical properties of the system. In this diagram, as explained in Chapter 1, the points at which the slope of the curve for a particular  $m$  value changes from positive to negative correspond to transitions in the number of convective rolls present in the onset flow pattern for that azimuthal wave number. For example, following the  $m = 0$  curve, for the region of  $A$  (aspect ratio) between  $.7$  and approximately  $1.7$ , where an inflection occurs, the onset flow pattern would be  $(0,2)$  pattern. Advancing in  $A$  to the range between about  $1.7$  and  $2.7$ , the onset flow pattern

would be a (0,4) pattern. At even higher aspect ratios, a (0,6) pattern could be seen. Likewise, for increasing  $A$ , with the changes from positive to negative in the slope of the  $m = 1$  curve, an onset  $m = 1$  pattern would progress from a (1,1) pattern to a (1,3) pattern, and then to a (1,5) pattern, and so on.

### **7.1.2 Non-Constant Viscosity Computations: Cylinder**

Table 7-2 shows the results of the non-constant viscosity computations for the three sets of cylindrical dimensions that were considered in experiments. As stated, the temperature at the top of the test section for all computations and experiments was 30.0 °C. In all computational cases for this research in which the variation of viscosity with temperature is taken into account, whether considering a cylindrical system or an annular system, the kinematic viscosity used in the Rayleigh number is the reference kinematic viscosity, which is a mean value based on the critical vertical temperature difference for each case. This is why, even though the critical vertical temperature difference for the non-constant viscosity case is noticeably different from that for the constant viscosity case, the critical Rayleigh numbers for the two cases can be nearly identical.

The critical temperature differences calculated for the non-constant viscosity case are generally higher than those calculated for the constant viscosity case. This can be seen by comparing Table 7-1 with Table 7-2. Now, the computed velocity profiles for these three sets of dimensions will be shown. In these flow profiles, the velocities are scaled, negative velocities represent downward flow in the  $z$ -direction (which extends into and out of the plane of the diagram), and positive velocities represent upward flow in the  $z$ -direction. All velocity profiles given in this chapter were computed using non-constant viscosity computations. Also, each of

the cross-sectional velocity profiles shown here represents a cross-sectional region approximately half of the distance along the vertical depth of the system that it is computed for.

When a non-constant viscosity computation for the critical conditions is carried out at a wide range of aspect ratios, a stability diagram relating the critical Rayleigh number to the dimensions of the system, much like Figure 7-1, can be obtained. Since the critical conditions determined from a non-constant viscosity computation are dependent on the vertical temperature difference in the system just before the onset of convection, which, for a given aspect ratio, is dependent on the vertical height of the system, the stability diagram differs very slightly from that for the constant viscosity case depending on the vertical height of the system being considered. Thus, in order to present the relation between the system dimensions and the critical Rayleigh number as simply and clearly as possible, for cylindrical systems and for annular systems, stability diagrams are presented only for the constant viscosity cases. Note that the vertical temperature difference in the system just before the onset of convection shows up in the dimensionless groups,  $F_0$  and  $\Omega$ , given in Chapter 4. To read more about the effects of considering a non-constant viscosity in calculations, the reader is directed to the work of Zhao, Moates, and Narayanan (Zhao, Moates, & Narayanan 1995).

### **7.1.3 Experiments: Cylinder**

Experiments were run to determine the critical vertical temperature difference and flow pattern for cylindrical systems of three sets of dimensions. The results of these experiments are given here and then compared to the computational results in Section 7.1.4. First, a table containing these experimental results is given, and then photos of the onset flow patterns for each of the three cases are given. In this table, the value used for the kinematic viscosity in the Rayleigh number is, in each case, the value corresponding to the mean temperature in the fluid

just before the onset of convection (if the critical temperature difference were 5.0 °C, then since the top temperature was always kept at 30.0 °C, the kinematic viscosity of the oil at 32.5 °C would be used in calculating the Rayleigh number).

Photos of the onset flow patterns follow (Figures 7-6 – 7-8). Remember that in these images, due to the use of aluminum powder as a tracer in the silicone oil, the lighter-colored regions are regions of horizontal flow, and the darker-colored regions are regions of vertical flow.

#### **7.1.4 Comparison of Results: Cylinder**

To begin with, all results are consolidated in Table 7-4. In this table, the “% Error” column is an indication of the absolute value of the percentage of error between the experimental critical temperature difference and the critical temperature difference obtained from the non-constant viscosity computation. The error percentage is computed with respect to the non-constant viscosity computational result. The error percentage has been adjusted by scaling out the portion of the error that results from uncertainty in the thermophysical properties assumed in computations (the thermophysical properties of the silicone oil used in experiments are close to but do not exactly match the values assumed in computations). Exactly how the error percentage is computed, adjusted in this way, is explained in Section 7.3. Thus, the error percentages in Table 7-4 represent error arising from sources other than thermophysical property uncertainty; several possible sources of experimental error are explained in Section 7.3.

Clearly, the non-constant viscosity computational results are closer to the experimental results than are the constant viscosity computational results. This is to be expected, though, because the non-constant viscosity form of the mathematical model more realistically represents the thermophysical behavior of the experimental system than does the constant viscosity form.

As Table 7-4 shows, the agreement between the non-constant viscosity computations and the experimental results is quite good when considering cylindrical systems. Now, the results for annular systems will be presented.

## **7.2 Annular Systems**

The critical conditions for the onset of convection in annular systems, as determined computationally and experimentally, are given in this section. Critical conditions were determined for six different sets of dimensions. Included in these six cases are three subsets of two cases each. In each subset of two cases, the outer radius of the annular test section is the same, but the inner radius of the annular test section is relatively small in one case, and relatively large in the other. Again, critical conditions were determined computationally for the case in which the variation of viscosity with temperature is included, and for the case in which it is not. The sets of dimensions considered in the calculations are the same sets of dimensions considered experimentally.

The dimensions for the three cases in which the ratio of the inner annular radius to the outer annular radius is small were chosen specifically because the onset flow patterns in those systems would include at least one radially aligned convective roll. Again, this approach is a point that distinguishes this research from the works of previous authors. It should be mentioned that the selection of the exact sizes of the inner annular pieces for the systems of small radius ratio were selected also, in part, based on the fact that inner pieces of too small a diameter would be too difficult to physically construct from lucite.

After the presentation of the computational results, the experimental results are shown, and then the computational and experimental results are compared.

### 7.2.1 Constant Viscosity Computations: Annulus

As explained in Section 7.1.1, the viscosity value assumed for the constant viscosity computations was the viscosity value for the oil at 35.0 °C, which is given in Appendix A. Now, a new system for naming the onset flow patterns in annular systems shall be introduced. From this point onward, the onset flow patterns in annular systems may be referred to using a parenthetical notation similar to the one used for naming the flow patterns in cylindrical systems. The parenthetical notation for flow patterns in annular systems, like the one for cylindrical systems, includes two indices, separated by a comma, within parentheses. The first index is the azimuthal wave number (which indicates the periodicity of the flow pattern in the azimuthal direction), and the second index indicates the maximum total number of radially aligned convective rolls which may be counted between the inner annular radius and the outer annular radius of the test section. The type of arrangement in which convective rolls are arranged like spokes on a wheel is called azimuthal alignment; if a convective roll spans the entire azimuthal extent of the test section and is concentric to the inner annular piece, then this is called radial alignment. For example, Figure 1-11 in Chapter 1 is a (12,0) pattern, and Figure 1-12 is a (2,1) pattern. Many more examples of the use of this nomenclature arise when the computationally and experimentally obtained onset flow patterns for annular systems are shown. Note that, while traversing along the azimuthal direction, an up-flow section is always accompanied by a down-flow section, and that the combination of an up-flow section and down-flow section adjacent in the azimuthal direction forms a convective cell. The azimuthal wave number relates more directly to convective cells than to convective rolls. This is why, in Figure 1-11, for example, 24 convective rolls along the azimuthal direction correspond to an azimuthal wave number of only

12. The results of the constant viscosity computations for annular systems, using this new notation, are given below as Table 7-5.

For any given aspect ratio, the constant viscosity computation for the critical conditions can be carried out for a wide range of  $S$  values. Doing this for several different aspect ratios elucidates the relations between the critical conditions, the radius ratio, and the aspect ratio for annular systems. These relations are illustrated below in stability diagrams (Figures 7-9 – 7-20) for several fixed values of the aspect ratio,  $A$ . The values of  $A$  considered in the diagrams include .75, the three values corresponding to the systems studied experimentally, 2.90, and 3.40. Also, as done in Section 7.1.1, close-up views of some of the more interesting regions of the diagrams accompany the full diagrams. Just like the relation between  $Ra_{crit}$  and  $A$  for constant viscosity cylindrical systems, the relations between  $Ra_{crit}$ ,  $A$ , and  $S$  for constant viscosity annular systems are the same regardless of the thermophysical properties or the specific dimensions of the system being considered. Again, this interesting characteristic of the system stems from the fact that the system is time-independent at the onset of convection. Also, as explained earlier, considering a viscosity non-constant with respect to temperature would result in slight differences in the stability diagrams depending on the specific dimensions of the system. Some comments on the diagrams follow.

Comparing the results for cylindrical systems in Table 7-4 with the results in Figures 7-11, 7-13, 7-15 in the regions of very small  $S$  values, it can be seen that as the center-piece of an annular system becomes extremely small in diameter, the onset flow pattern in the annular system is the same as the onset pattern in the corresponding cylindrical system. This seems quite reasonable since an annular system with a center-piece extremely small in diameter is nearly a cylindrical system. In most annular cases considered in this research, except for those at higher

aspect ratios (such as 2.90 or 3.40), the onset flow pattern at small  $S$  values is  $m = 0, 1,$  or  $2$ . Onset flow patterns with azimuthal wave numbers of  $m = 0, 1,$  and  $2$  are the onset flow patterns most often seen in the cylindrical systems considered in this research, as well, as shown in Figure 7-1. Typically, the  $m = 0, 1,$  and  $2$  onset flow patterns include convective rolls in radial alignment in addition to azimuthally aligned convective rolls (except for the  $m = 0$  pattern which includes no azimuthally aligned convective rolls), and onset flow patterns with azimuthal wave numbers of  $m = 3$  or higher, for the cases considered in this research, do not tend to include radially aligned convective rolls. At higher  $S$  values, the onset flow patterns in the annular systems considered are generally of high azimuthal wave number (such as  $m = 3, 4, 5,$  etc.) and include only azimuthally aligned convective rolls. At these high  $S$  values, a higher  $S$  value generally corresponds to a higher azimuthal wave number. This is plausible because increasing  $S$  narrows the area in which flow can occur, causing azimuthally aligned convective cells to stretch out in the azimuthal direction to spatially fill the system, and at certain high enough  $S$  values, it is simply more energetically favorable for new azimuthally aligned convective cells to form rather than to stretch the existing cells even further into extreme azimuthal lengths. All of this agrees with the observations of Littlefield and Desai that an annulus with a small  $S$  value behaves more like a cylindrical system, and an annulus with a large  $S$  value behaves more like a long, rectangular system.

In these stability diagrams, as is the case for cylindrical systems, the azimuthal wave number with the lowest curve at a given radius ratio is the azimuthal wave number of the disturbance most destabilizing to the system at that radius ratio, and, thus, is the azimuthal wave number of the onset flow pattern at that radius ratio. Also, changes in the number of radially aligned convective rolls present in the onset flow pattern of a given azimuthal wave number are

indicated by inflections in the stability curves. However, by examining the computed onset velocity profiles while doing the computations for this research, it was seen that not all inflections in the stability curves correspond to these pattern transitions. Some of the less severe inflections simply correspond to slight variations in the instability of the system to a particular pattern with unchanging numbers of radially and azimuthally aligned convective rolls. In general, the number of radially aligned convective rolls in the onset flow pattern for a given azimuthal wave number decreases as the radius ratio is increased. This is logical because in annular systems with higher radius ratios, it is energetically more and more difficult for a flow pattern with a greater number of radially aligned convective rolls to exist due to the no-slip conditions on velocity imposed by the inner and outer radial walls of the annulus.

It has been explained, now, how the radius ratio in an annular system affects the numbers of azimuthally and radially aligned convective rolls present at the onset of convection. In the stability diagrams above, the effect of  $S$  on the number of azimuthally aligned rolls is obvious; the effect of  $S$  on the number of radially aligned rolls has been explained, though it is not quite so easy to see on the stability diagrams since some of the less severe inflections on the diagrams do not correspond to pattern transitions. Another key point is that the aspect ratio of an annular system determines the range of values over which the numbers of azimuthally and radially aligned convective rolls vary in response to variations in the radius ratio. A system of large aspect ratio, since it is more spacious, will generally have higher numbers of both azimuthally and radially aligned convective rolls present in its onset flow patterns than will a system of smaller aspect ratio. Stork and Müller's experiments, for example, addressed large aspect ratios, such as  $A = 5$ , and the onset patterns they observed had quite large azimuthal wave numbers. As

a side note, the MATLAB computational program written for this research was able to predict the same onset flow patterns that Stork and Müller observed experimentally.

### **7.2.2 Non-Constant Viscosity Computations: Annulus**

Table 7-6 presents the results of the non-constant viscosity computations for the sets of annular dimensions that were considered in experiments. Again, the temperature at the top of the test section was 30.0 °C.

The computed velocity profiles for these annular cases are shown below (Figures 7-21 – 7-26). Again, the velocities in these profiles are scaled, negative velocities represent downward flow in the z-direction (which extends into and out of the plane of the diagram), and positive velocities represent upward flow in the z-direction.

### **7.2.3 Experiments: Annulus**

In this section, a table containing the experimental results for annular systems is given. Then, photos of the onset flow patterns for each of the cases are given. In the table, the value used for the kinematic viscosity in the Rayleigh number is the value corresponding to the mean temperature in the fluid just before the onset of convection.

Photos of the onset flow patterns observed in the experiments on annular systems are given as Figures 7-27 – 7-32.

Any noticeable asymmetries in these patterns are, of course, simply due to small imperfections in the experimental system that cause it to slightly differ from the theoretical system. If it is noticeable that some of these flow patterns appear to be more strongly flowing than others, the reason for that is simple. In several experimental cases, the computationally predicted onset flow pattern would show up at supercritical conditions (in which the vertical temperature difference in the experiment exceeds the critical value determined by the

experiment), and when this happened, the flow was even stronger than it would be at onset, allowing the pattern to be more easily viewed in photos. In other cases, however, the computationally predicted onset flow pattern would appear only near the critical temperature difference determined by the experiment, and would thus be flowing relatively weakly, and be less distinct in appearance.

Figure 7-27 is the  $m = 0:(0,1)$  onset flow pattern seen in the annular container with  $R_o = 8.75$  mm. The flow pattern was particularly weak and sometimes difficult to discern in this particular case. A reason suspected for this is that the systems with  $R_o = 8.75$  mm were the smallest in radial extent of all systems considered, and the combination of the radially confining dimensions of the system and the relatively large radial components of velocity associated with the  $m = 0:(0,1)$  flow pattern resulted in much of the aluminum tracer powder in the test fluid quickly adhering to the radial walls and bottom plate of the system.

#### **7.2.4 Comparison of Results: Annulus**

Table 7-8 includes all of the results obtained for annular systems. The “% Error” column, an indication of the absolute value of the percentage of error between the experimental critical temperature difference and the critical temperature difference obtained from the non-constant viscosity computation, is calculated with respect to the non-constant viscosity computational result. Again, the error has been adjusted to exclude the portion which arises from uncertainty in the thermophysical property values assumed in computations. Thus, the error percentages shown represent experimental error due to other sources; several possible error sources are described in Section 7.3. Also, as expected, the non-constant viscosity results more closely match the experimental results than do the constant viscosity results; this is because of

the fact that the non-constant viscosity computation more realistically represents the experimental system.

As this table shows, the agreement between the computational and experimental critical temperature difference results is best in the cases in which  $S$  has a smaller value. Even though a full analysis of the errors in the results is given in Section 7.3, a possible explanation for the poorer agreement between computations and experiments for some of the annular cases will be given here. The cases in which  $S$  is of higher value are the cases in which the center-block of the annulus is larger, and the annular gap width is smaller. It is suspected that the reason for the larger errors in the experimental critical temperature difference results for large  $S$  have to do with the small annular gap width. Slight imperfections in the centering of the annular center-block within the outer annular wall of the experimental system could exist due to extremely small errors in machining, such as errors in the machining of the bottom plate of the test section (in terms of the placement of the notch that the annular center-block is nested in) or the lucite center-blocks of the annular systems. Any small imperfection in the centering of the annular center-block would slightly affect the critical conditions for convection, but would have an even larger effect on the critical conditions for convection in cases in which the annular gap width is smaller, and thus could cause a more noticeable increase in the experimental critical temperature difference in those cases. The reasoning behind this statement is as follows. In an annulus with an off-centered middle-piece, some region of the annulus has a smaller gap width than the originally intended gap width, and the initiation of convective flow in this region, due to its higher degree of mechanical confinement, would be even more difficult than the initiation of flow elsewhere in the annular test section, and would consequently make the entire system more stable to convection. This effect would strengthen as the annular center-block increases in

diameter, because annular center-blocks of larger and larger diameter would introduce smaller and smaller minimum gap widths to a system in which the annular center-block is slightly off-centered. This effect, then, would not be expected to show up as strongly in cases with larger annular gap widths. The experimental results, in fact, support this hypothesis. Of the three cases in which  $S$  is larger, the case in which the annular gap width is largest ( $L_z = 6.53$  mm,  $R_o = 11.28$  mm,  $S = .40$ ) has the smallest error of the three (see Table 7-8), the case with the second largest annular gap width ( $L_z = 6.85$  mm,  $R_o = 8.75$  mm,  $S = .30$ ) has the second smallest error, and the case with the smallest annular gap width ( $L_z = 7.18$  mm,  $R_o = 11.51$  mm,  $S = .50$ ) has the largest error. Since the imperfections present in each experimental run could slightly differ, the degree of off-centering in annular experiments was different in each run. Still, some test measurements of the annular gap width at different locations within the test section showed that the degree of possible off-centering is very small (hundredths of a millimeter) compared to the width of the annular gap.

Another obvious point of discussion in Table 7-8 is that, in one case, the experimentally observed onset flow pattern was not the computationally predicted pattern. For that particular system, the computation shows the difference between the onset vertical temperature differences for the  $m = 0:(0,1)$  pattern, which was predicted computationally, and the  $m = 2:(2,1)$  pattern which was experimentally observed, to be about  $.2$  °C. This is outside of the range of experimental error. It is suspected that the difference in patterns may be a result of imperfections related to the off-centering of the annular center-block, which were just discussed, or perhaps some similarly small experimental imperfections. Off-centering of the annular center-block would make it very difficult for the  $m = 0:(0,1)$  pattern, which is axisymmetric in the azimuthal direction, to form or be sustained (an annular system with an off-centered center-block is, itself,

not azimuthally axisymmetric). This would explain why, even for the case in which an  $m = 0:(0,1)$  was obtained experimentally, the flow was very weak. A full error analysis follows in Section 7.3.

All of these results are summarized in the first section of Chapter 8.

### 7.3 Error Analysis

Unavoidably, some error is present in the experimental results. The main sources of error in the experimental results are error in the thermophysical properties used in the computations, errors in the exact dimensions of the test section (due to machining error), and error in the accuracy of temperature measurements. Imperfect leveling of the test section should also be mentioned as a source of potential error.

One possible source of errors in the thermophysical properties is error in the viscosity measurements taken to determine the dependence of the viscosity of the oil on temperature for the non-constant viscosity computations. Again, a Cole-Parmer<sup>®</sup> 98936 series viscometer was used for viscosity measurements. The oil being tested needed to be kept at several constant temperature values for set lengths of time (more details on the viscosity measurements are given in Appendix A). Its temperature was regulated by circulating water from the large NESLAB water bath mentioned in Chapter 6. Thus, the potential error in the viscosity measurements arises from error in the temperature control provided by the NESLAB water bath. The NESLAB water bath provided great temperature control, keeping the temperature of the oil constant with an error of no more than approximately  $\pm .02$  °C. This could cause a small error in the viscosity values used in the computations, but the maximum possible error in the viscosity is so extremely small (as shown by test computations) that it does not noticeably affect the computed critical temperature differences.

The exact values of the thermophysical properties of silicone oil assumed for the computations (shown in Appendix A) are taken from data provided by Dow Corning and, thus, are reasonably close to the actual properties of the silicone oil used in experiments. Still, they are, of course, not perfect matches to the actual experimental thermophysical properties of the silicone oil. While there is no way to know the exact thermophysical properties of the silicone oil used in experiments, the total experimental error can be adjusted to exclude the portion due to errors in the thermophysical property values assumed in computations by comparing ratios of the results; this will now be explained. First, a ratio must be taken of the  $([\Delta T]_{\text{crit}} * L_z^3)$  value obtained from the constant viscosity computation for a certain test case (call it Case 2) to the  $([\Delta T]_{\text{crit}} * L_z^3)$  value for a different test case (call it Case 1). Then, a ratio must be taken of the  $([\Delta T]_{\text{crit}} * L_z^3)$  value obtained from the experimental result from Case 2 to that from Case 1.

Lastly, those two ratios must be compared. The “% Error” between the two ratios is calculated

simply as  $\frac{|Computational\ Ratio - Experimental\ Ratio|}{Computational\ Ratio} * 100$ . The reasoning behind this process

follows. Taking a ratio of  $([\Delta T]_{\text{crit}} * L_z^3)$  values is the same as taking a ratio of the critical Rayleigh numbers, for the constant viscosity computational results and the experimental results, for a given pair of systems, with the thermophysical properties divided out. The ratio of the critical Rayleigh numbers obtained from the constant viscosity computational results should be very close to the ratio of the critical Rayleigh numbers obtained from the experimental results.

Since the thermophysical properties are divided out, any error between the  $([\Delta T]_{\text{crit}} * L_z^3)$  ratio from the computational results and the  $([\Delta T]_{\text{crit}} * L_z^3)$  ratio from the experimental results must be due to errors in the experiment other than the error associated with uncertainty in the thermophysical properties. Throughout this explanation, the constant viscosity computations have been referred to rather than the non-constant viscosity computations. Still, the entire

explanation applies for the non-constant viscosity computations, as well, because the only difference in the thermophysical properties for the two cases is the viscosity value, and, as viscosity measurements show, the variation in viscosity over the vertical temperature differences considered here is reasonably small. This error-adjustment procedure was followed to obtain the error percentages shown in Tables 7-4 and 7-8 (which are based on the non-constant viscosity computational results). It is applied to every test case except for one. The excluded test case is the reference case in this error-adjustment procedure, and its results are used in the denominator of every ratio taken; in the above explanation, Case 1 is the reference case, and for the error percentages in Tables 7-4 and 7-8, the cylindrical case with an aspect ratio of 1.28 is used as the reference case. Thus, the error percentage shown for the cylindrical case of aspect ratio 1.28 does still include error due to uncertainty in assumed thermophysical properties, and it is

calculated simply as 
$$\frac{|Computational [\Delta T]_{crit} - Experimental [\Delta T]_{crit}|}{Computational [\Delta T]_{crit}} * 100.$$
 The significant

error between the computational and experimental results for some of the annular systems seen in Table 7-8, then, must be attributed to factors other than uncertainty in the experimental thermophysical properties. In fact, it is likely that the relatively large error in those cases arises from the possible slight off-centering of the center-block of the annular system (this effect is described thoroughly in Section 7.2.4).

The dimensions of the lucite rings and inner annular pieces made for the experiment were measured as accurately as possible, with a depth micrometer, but still an error of approximately  $\pm .025$  mm (.0254 mm is a thousandth of an inch) arises in the measured dimensions. Some test computations show that this error could typically lead to an error of about  $\pm .03$  °C. This will be included in the experimental results along with the next error to be discussed.

Some error in temperature measurement was present in the experimental results. Each of the OMEGA thermistors used in the experiment had an error of  $\pm .15$  °C, but since multiple thermistors were used in both the bottom and top water baths, the overall error in the temperature reading at each of those locations was reduced. The error in the temperature reading of the continuously stirred bottom water bath was reduced to  $\pm .05$  °C since three thermistors were used to read the temperature in the bath. The constant temperature (30.0 °C) of the top water bath, while it was monitored using two OMEGA thermistors, was controlled by the large NESLAB water bath. The NESLAB bath was able to maintain a temperature within approximately  $\pm .02$  °C of 30.0 °C (and the thermistors near the upper flow-through water bath showed that there was not significant heat loss to the surroundings as the water flowed from the NESLAB bath to the upper flow-through water bath). Thus, a total error of  $\pm .07$  °C is associated with experimental measurements of the vertical temperature difference. Adding this to the  $\pm .03$  °C machining-related error gives a total error of  $\pm .1$  °C for the experimental results. Note, then, that the “ $\pm .1$  °C” error indications on the tables of results include both the error in temperature measurement and the error due to uncertainties in the precision of machining.

The critical temperature differences in the experiments were never any lower than 5.0 °C, which means that the experimental error of  $\pm .1$  °C was always an error of less than 2 %. This means that any portion of the experimental error greater than approximately 2 % (see Tables 7-4, 7-8) is due to factors other than those considered to reach the  $\pm .1$  °C error estimate. One such factor, in the case of the annular systems, is the possible off-centering of the annular center-block, which has already been explained in Section 7.2.4. Another possible error source was imperfect leveling of the test section. Great care was taken in ensuring that the bottom plate of the test section was level before assembling the experimental apparatus on top of it. A bubble-

level was placed on the bottom copper plate of the test section, and its reading was used to guide adjustments to a leveling plate upon which the entire apparatus sat. Still, the level, itself could not be perfectly accurate. Also, it is likely that the tightening of the four screws which were used to tighten down the lucite clamp on the outer ring of the test section was not perfectly equal on all four screws, and thus, the top of the test section may not have been perfectly level either.

Again, the results in this chapter are summarized at the beginning of Chapter 8.

Table 7-1. Constant viscosity computational results: critical temperature difference and onset flow pattern for sets of cylindrical dimensions considered in experiments.

$L_z$ (mm)	$L_r$ (mm)	$A$	$[\Delta T]_{crit}$ (°C)	$Ra_{crit}$	Onset Flow Pattern
					$m =$
6.85	8.75	1.28	5.58	1907	0:(0,2)
7.18	11.51	1.60	4.82	1890	1:(1,3)
6.53	11.28	1.73	6.23	1841	1:(1,3)

Table 7-2. Non-constant viscosity computational results: critical temperature difference and onset flow pattern for sets of cylindrical dimensions considered in experiments.

$L_z$ (mm)	$L_r$ (mm)	$A$	$[\Delta T]_{crit}$ (°C)	$Ra_{crit}$	Onset Flow Pattern
					$m =$
6.85	8.75	1.28	5.80	1906	0:(0,2)
7.18	11.51	1.60	5.04	1889	1:(1,3)
6.53	11.28	1.73	6.43	1840	1:(1,3)

Table 7-3. Experimental results: critical temperature difference and onset flow pattern for sets of cylindrical dimensions.

$L_z$ (mm)	$L_r$ (mm)	$A$	$[\Delta T]_{crit}$ (°C)	$Ra_{crit}$	Onset Flow Pattern
					$m =$
6.85	8.75	1.28	$5.9 \pm .1$	1943	0:(0,2)
7.18	11.51	1.60	$5.2 \pm .1$	1953	1:(1,3)
6.53	11.28	1.73	$6.5 \pm .1$	1862	1:(1,3)

\* In these results,  $L_z$  and  $L_r$  values have an error of  $\pm .025$  mm, and the error in  $[\Delta T]_{crit}$  includes a  $\pm .03$  °C due to this, as well as a  $\pm .07$  °C error from temperature measurement.

Table 7-4. Summary of computational and experimental results for cylindrical systems.

Constant Visc., $\Delta T$ (°C)	Constant Visc., Pattern	Non-Constant Visc., $\Delta T$ (°C)	Non-Constant Visc., Pattern	Expt. $\Delta T$ (°C)	Expt. Pattern	% Error
<b>Aspect Ratio: 1.28, <math>L_z = 6.85</math> mm, <math>L_r = 8.75</math> mm, Figures 7-3, 7-6, see note below table</b>						
5.58	0:(0,2)	5.8	0:(0,2)	$5.9 \pm .1$	0:(0,2)	0.03 - 3.48
<b>Aspect Ratio: 1.60, <math>L_z = 7.18</math> mm, <math>L_r = 11.51</math> mm, Figures 7-4, 7-7</b>						
4.82	1:(1,3)	5.04	1:(1,3)	$5.2 \pm .1$	1:(1,3)	0.00 - 3.37
<b>Aspect Ratio: 1.73, <math>L_z = 6.53</math> mm, <math>L_r = 11.28</math> mm, Figures 7-5, 7-8</b>						
6.23	1:(1,3)	6.43	1:(1,3)	$6.5 \pm .1$	1:(1,3)	0.00 - 2.24

\* In the experimental results,  $L_z$  and  $L_r$  values have an error of  $\pm .025$  mm, and the error in  $[\Delta T]_{crit}$  includes a  $\pm .03$  °C due to this, as well as a  $\pm .07$  °C error from temperature measurement. The range of error percentages shown corresponds to the indicated  $\pm .1$  °C error in the experimental critical temperature differences. Error percentages are shown with the contribution from uncertainty in the thermophysical properties scaled out. This scaling was done with the cylindrical case of aspect ratio 1.28 used as the reference case, so that case is the only case for which the error percentage still includes the effects of uncertainty in the thermophysical properties.

Table 7-5. Constant viscosity computational results: critical temperature difference and onset flow pattern for sets of annular dimensions considered in experiments.

$L_z$ (mm)	$R_o$ (mm)	$R_i$ (mm)	A	S	$[\Delta T]_{crit}$ (°C)	$Ra_{crit}$	Onset Flow Pattern $m =$
6.85	8.75	1.40	1.28	0.16	6.89	2355	0:(0,1)
6.85	8.75	2.62	1.28	0.30	7.51	2567	3:(3,0)
7.18	11.51	1.38	1.60	0.12	5.35	2099	0:(0,1)
7.18	11.51	5.76	1.60	0.50	6.90	2706	4:(4,0)
6.53	11.28	1.18	1.73	0.10	7.03	2079	2:(2,1)
6.53	11.28	4.51	1.73	0.40	7.93	2345	4:(4,0)

Table 7-6. Non-constant viscosity computational results: critical temperature difference and onset flow pattern for sets of annular dimensions considered in experiments.

$L_z$ (mm)	$R_o$ (mm)	$R_i$ (mm)	A	S	$[\Delta T]_{crit}$ (°C)	$Ra_{crit}$	Onset Flow Pattern $m =$
6.85	8.75	1.40	1.28	0.16	7.08	2353	0:(0,1)
6.85	8.75	2.62	1.28	0.30	7.67	2564	3:(3,0)
7.18	11.51	1.38	1.60	0.12	5.57	2098	0:(0,1)
7.18	11.51	5.76	1.60	0.50	7.09	2704	4:(4,0)
6.53	11.28	1.18	1.73	0.10	7.21	2077	2:(2,1)
6.53	11.28	4.51	1.73	0.40	8.07	2343	4:(4,0)

Table 7-7. Experimental results: critical temperature difference and onset flow pattern for sets of annular dimensions.

$L_z$ (mm)	$R_o$ (mm)	$R_i$ (mm)	$A$	$S$	$[\Delta T]_{crit}$ (°C)	$Ra_{crit}$	Onset Flow Pattern $m =$
6.85	8.75	1.40	1.28	0.16	$7.7 \pm .1$	2573	0:(0,1)
6.85	8.75	2.62	1.28	0.30	$8.8 \pm .1$	2969	3:(3,0)
7.18	11.51	1.38	1.60	0.12	$5.8 \pm .1$	2189	2:(2,1)
7.18	11.51	5.76	1.60	0.50	$8.4 \pm .1$	3242	4:(4,0)
6.53	11.28	1.18	1.73	0.10	$7.5 \pm .1$	2165	2:(2,1)
6.53	11.28	4.51	1.73	0.40	$9.1 \pm .1$	2664	4:(4,0)

\* In these results,  $L_z$  and  $L_r$  values have an error of  $\pm .025$  mm, and the error in  $[\Delta T]_{crit}$  includes a  $\pm .03$  °C due to this, as well as a  $\pm .07$  °C error from temperature measurement.

Table 7-8. Summary of computational and experimental results for annular systems.

Constant Visc., $\Delta T$ (°C)	Constant Visc., Pattern	Non-Constant Visc., $\Delta T$ (°C)	Non-Constant Visc., Pattern	Expt. $\Delta T$ (°C)	Expt. Pattern	% Error
<b><math>A = 1.28, S = .16, L_z = 6.85</math> mm, <math>R_o = 8.75</math> mm, <math>R_i = 1.40</math>, Figures 7-21, 7-27</b>						
6.89	0:(0,1)	7.08	0:(0,1)	$7.7 \pm .1$	0:(0,1)	5.51 - 8.29
<b><math>A = 1.28, S = .30, L_z = 6.85</math> mm, <math>R_o = 8.75</math> mm, <math>R_i = 2.62</math>, Figures 7-22, 7-28</b>						
7.51	3:(3,0)	7.67	3:(3,0)	$8.8 \pm .1$	3:(3,0)	11.41 - 13.97
<b><math>A = 1.60, S = .12, L_z = 7.18</math> mm, <math>R_o = 11.51</math> mm, <math>R_i = 1.38</math>, Figures 7-23, 7-29</b>						
5.35	0:(0,1)	5.57	0:(0,1)	$5.8 \pm .1$	2:(2,1)	0.56 - 4.09
<b><math>A = 1.60, S = .50, L_z = 7.18</math> mm, <math>R_o = 11.51</math> mm, <math>R_i = 5.76</math>, Figures 7-24, 7-30</b>						
6.90	4:(4,0)	7.09	4:(4,0)	$8.4 \pm .1$	4:(4,0)	15.13 - 17.90
<b><math>A = 1.73, S = .10, L_z = 6.53</math> mm, <math>R_o = 11.28</math> mm, <math>R_i = 1.18</math>, Figures 7-25, 7-31</b>						
7.03	2:(2,1)	7.21	2:(2,1)	$7.5 \pm .1$	2:(2,1)	0.81 - 3.54
<b><math>A = 1.73, S = .40, L_z = 6.53</math> mm, <math>R_o = 11.28</math> mm, <math>R_i = 4.51</math>, Figures 7-26, 7-32</b>						
7.93	4:(4,0)	8.07	4:(4,0)	$9.1 \pm .1$	4:(4,0)	9.55 - 11.98

\* In the experimental results,  $L_z$ ,  $R_o$ , and  $R_i$  values have an error of  $\pm .025$  mm, and the error in  $[\Delta T]_{crit}$  includes a  $\pm .03$  °C due to this, as well as a  $\pm .07$  °C error from temperature measurement. The range of error percentages shown corresponds to the indicated  $\pm .1$  °C error in the experimental critical temperature differences. Error percentages are shown with the contribution from uncertainty in the thermophysical properties scaled out. This scaling was done with the cylindrical case of aspect ratio 1.28 used as the reference case.

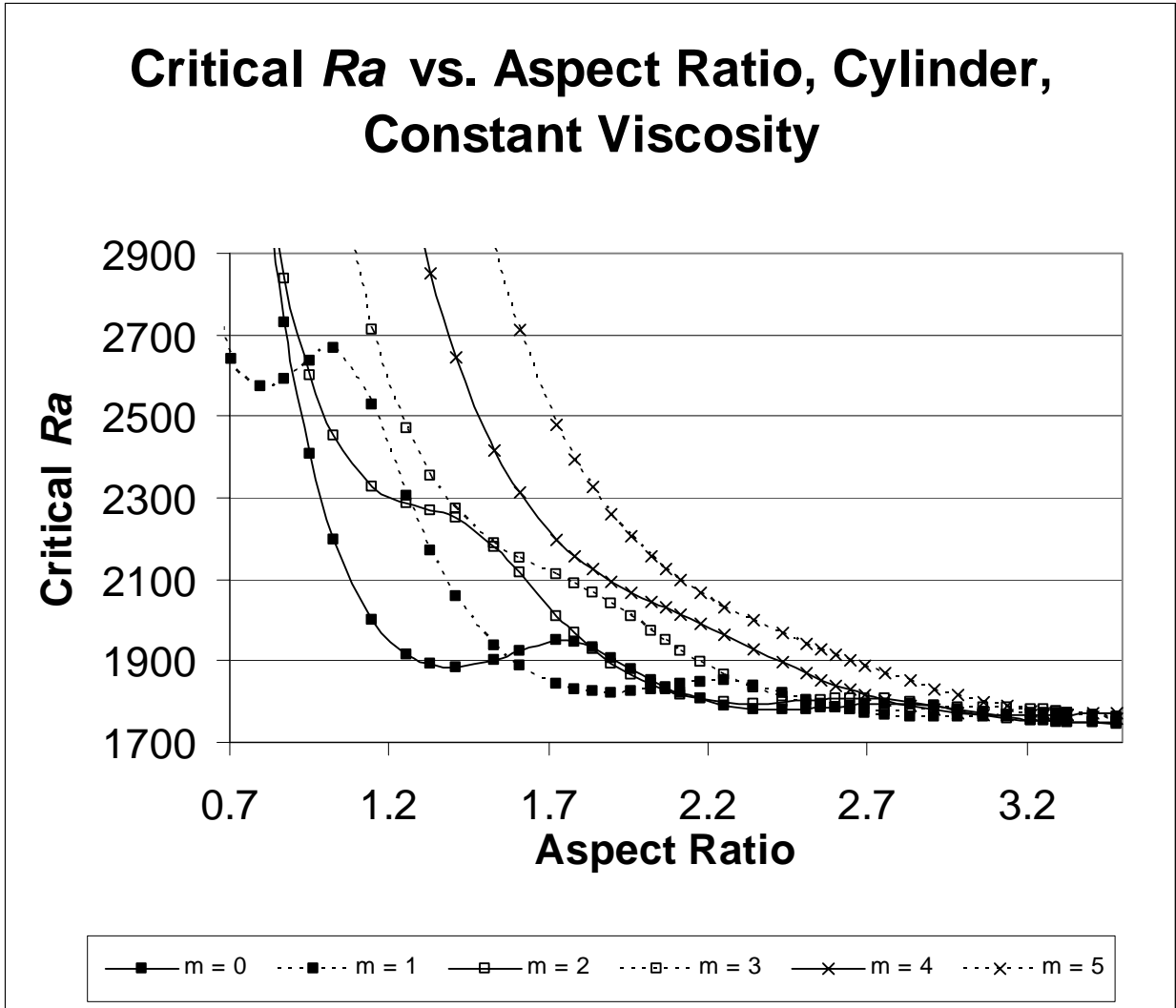


Figure 7-1. Constant viscosity computational results:  $Ra_{crit}$  vs.  $A$  for cylindrical systems.

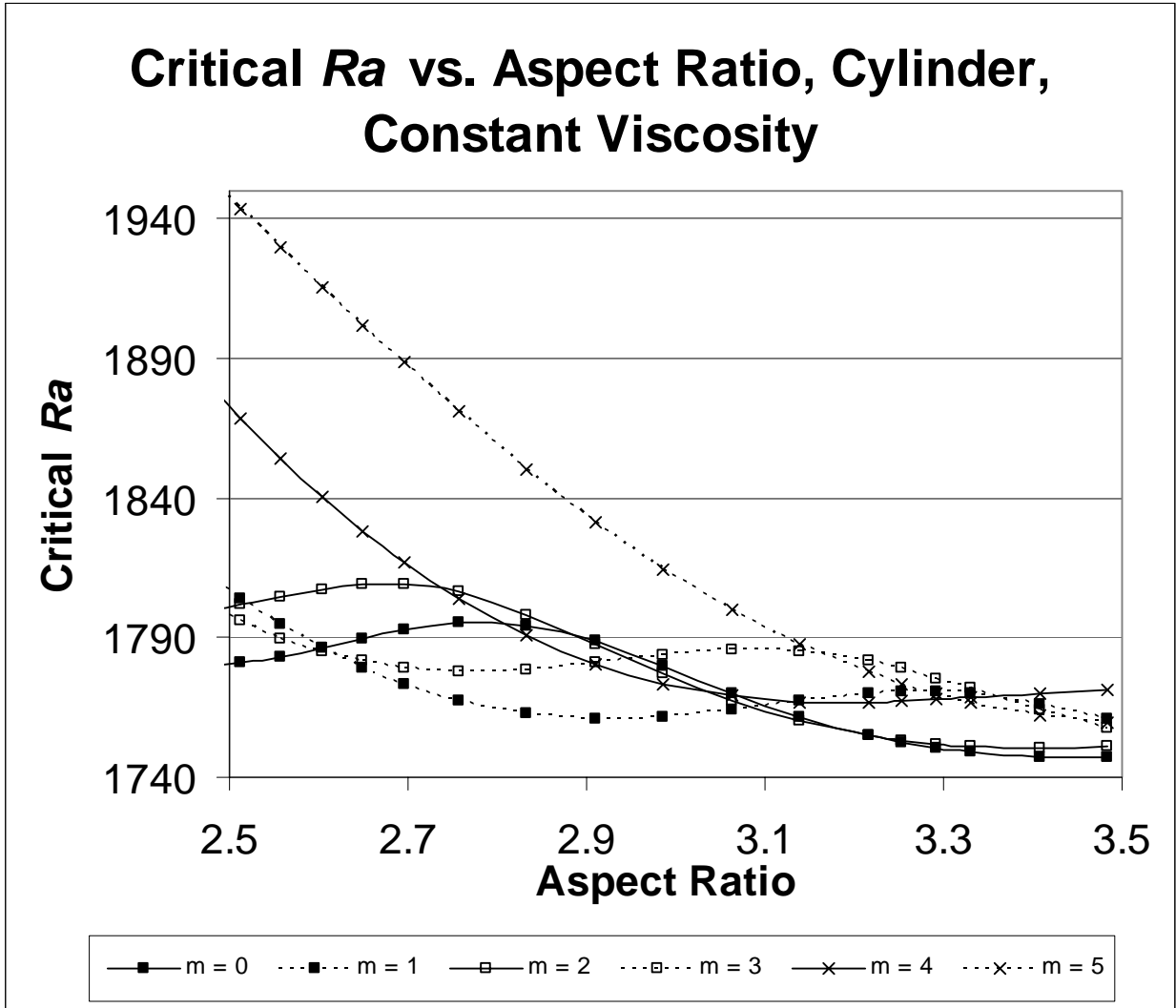


Figure 7-2. Constant viscosity computational results:  $Ra_{crit}$  vs.  $A$  for cylindrical systems, close-up view.

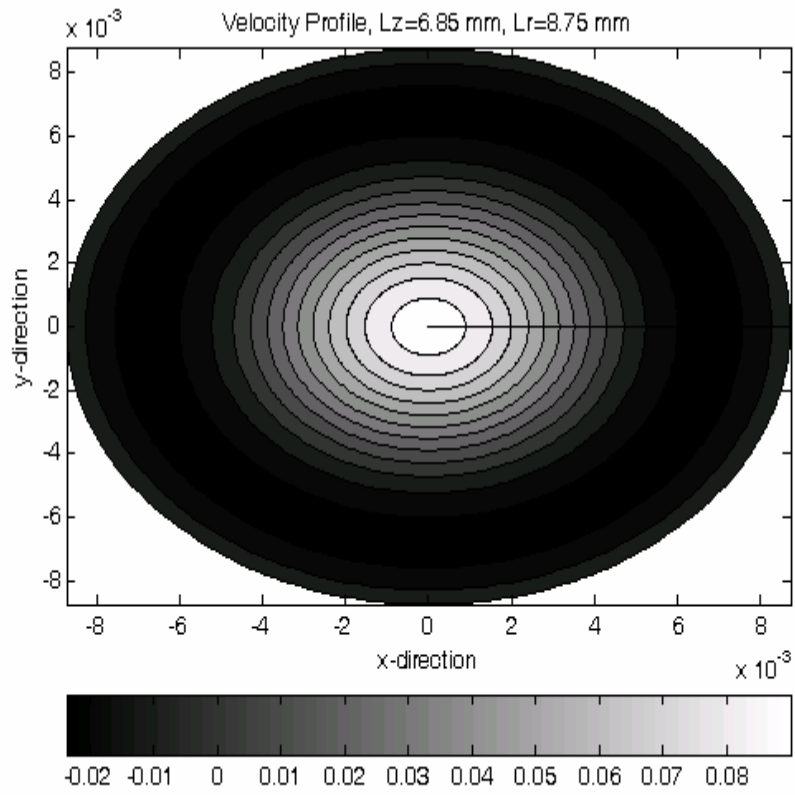


Figure 7-3. Computed velocity profile, cross-sectional view,  $L_z = 6.85$  mm,  $L_r = 8.75$  mm,  $m = 0:(0,2)$ ,  $[\Delta T]_{\text{crit}} = 5.80$  °C.

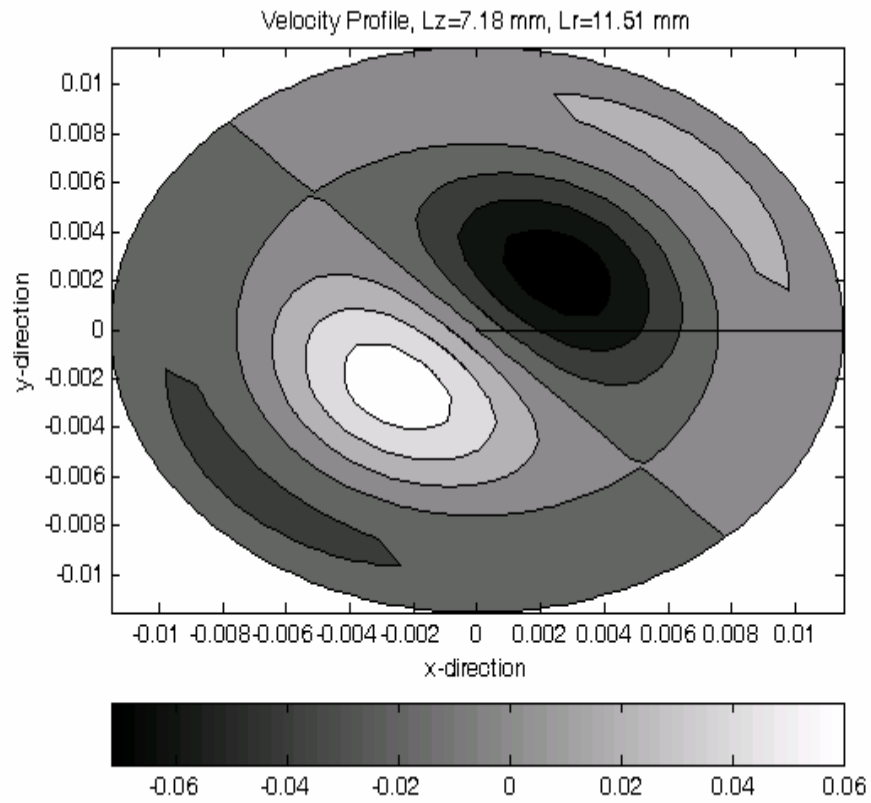


Figure 7-4. Computed velocity profile, cross-sectional View, Lz = 7.18 mm, Lr = 11.51 mm, m = 1:(1,3),  $[\Delta T]_{\text{crit}} = 5.04 \text{ }^\circ\text{C}$ .

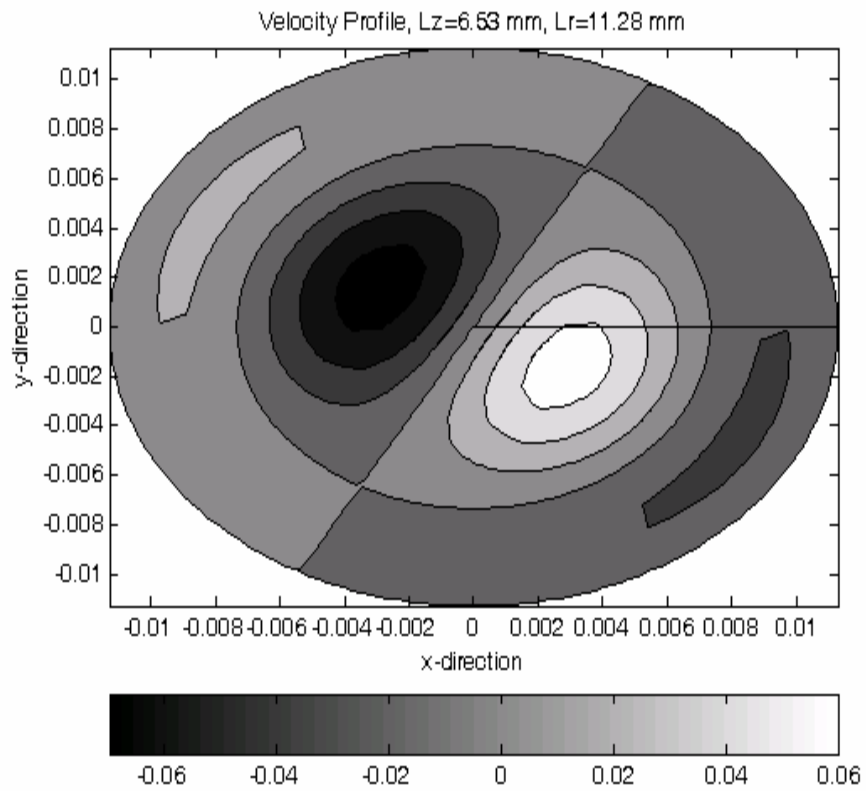


Figure 7-5. Computed velocity profile, cross-sectional view,  $L_z = 6.53$  mm,  $L_r = 11.28$  mm,  $m = 1:(1,3)$ ,  $[\Delta T]_{\text{crit}} = 6.43$  °C.

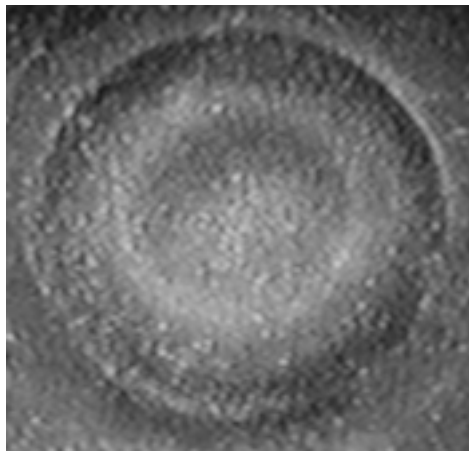


Figure 7-6. Photo of onset flow pattern,  $L_z = 6.85$  mm,  $L_r = 8.75$  mm,  $m = 0:(0,2)$ .

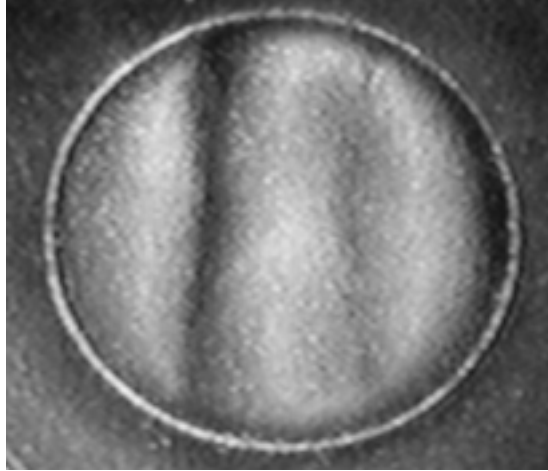


Figure 7-7. Photo of onset flow pattern,  $L_z = 7.18$  mm,  $L_r = 11.51$  mm,  $m = 1:(1,3)$ .

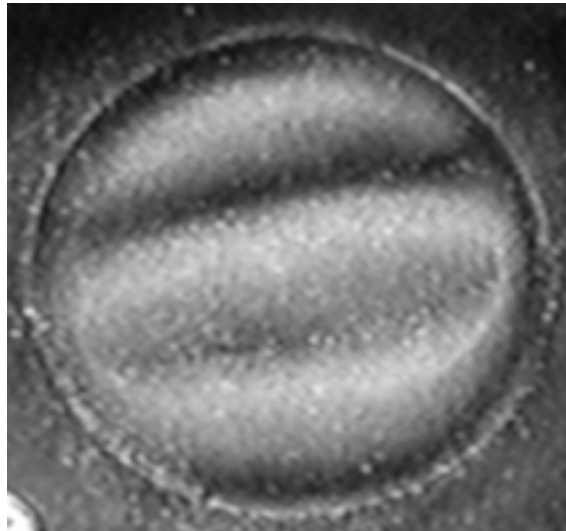


Figure 7-8. Photo of onset flow pattern,  $L_z = 6.53$  mm,  $L_r = 11.28$  mm,  $m = 1:(1,3)$ .

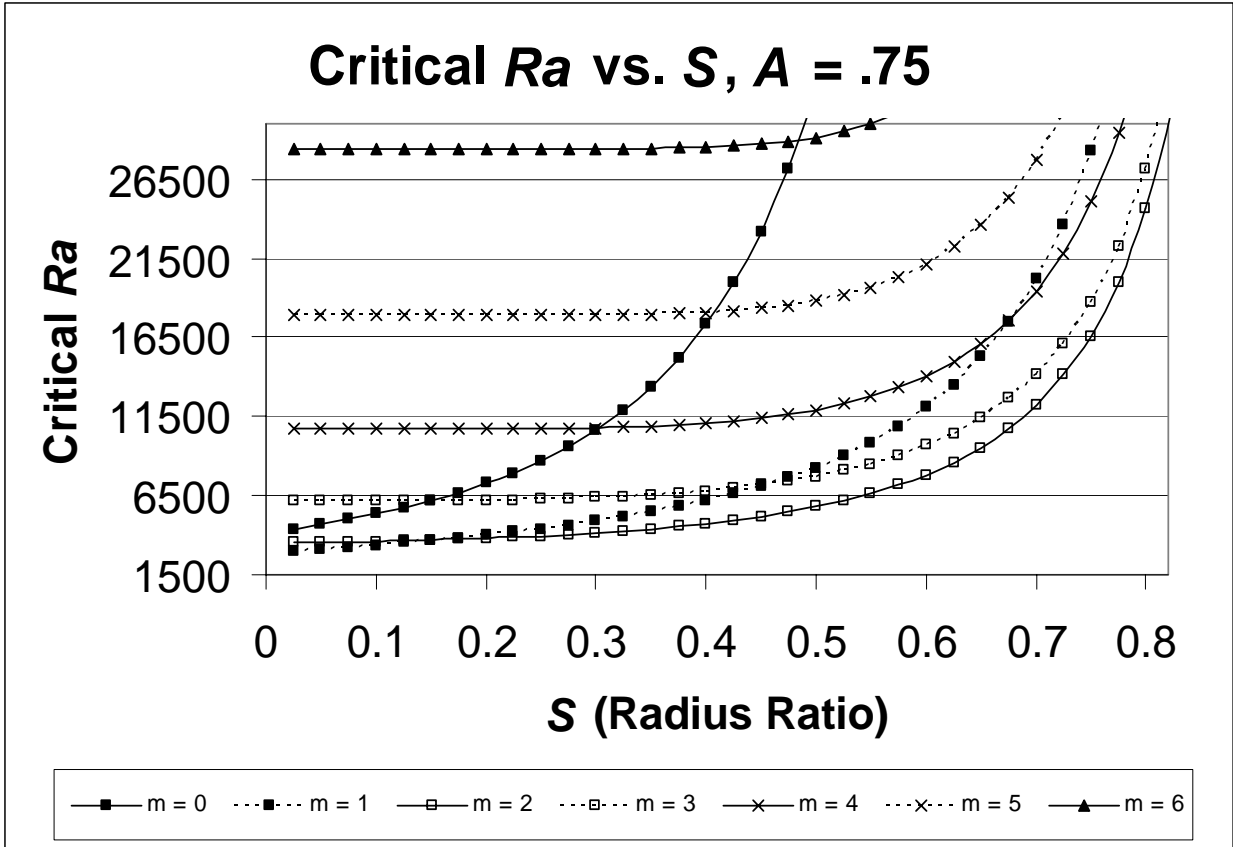


Figure 7-9. Constant viscosity computational results:  $Ra_{crit}$  vs.  $S$  for annular systems with  $A = .75$ .

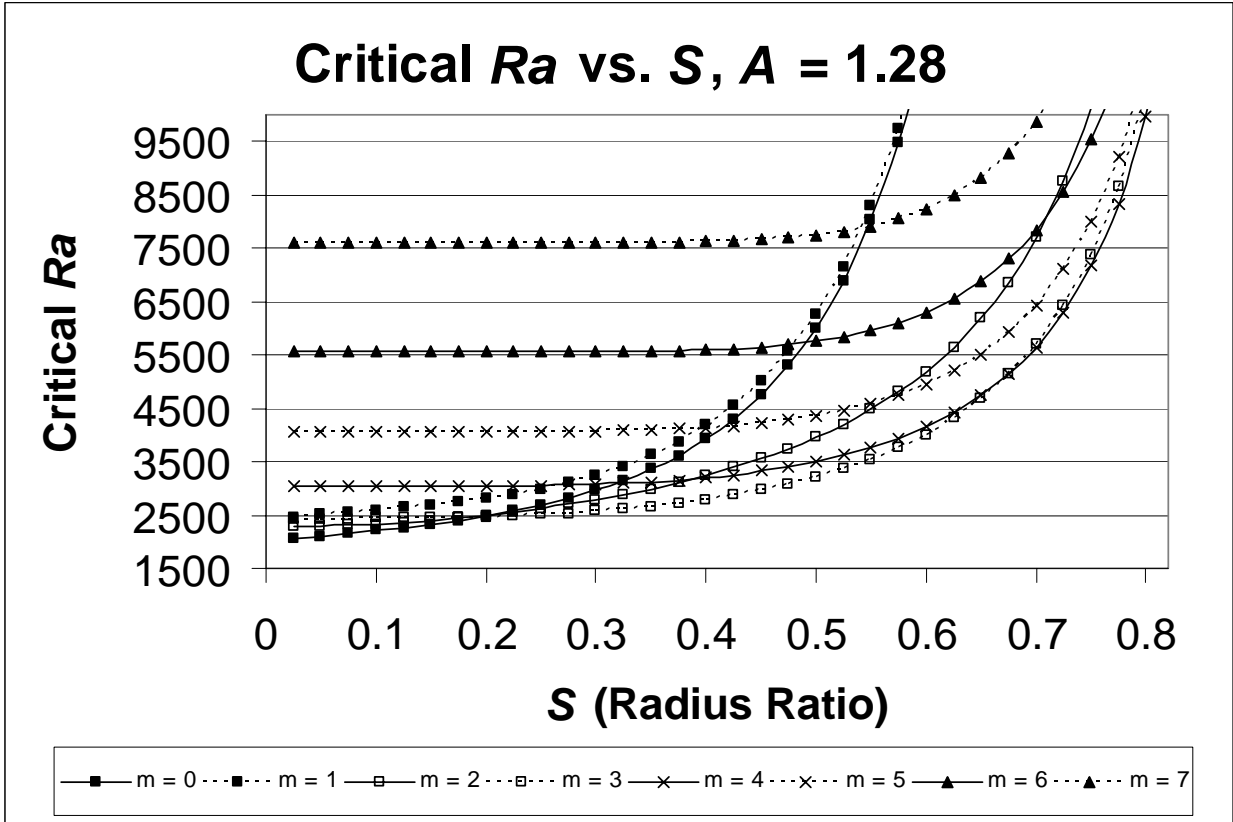


Figure 7-10. Constant viscosity computational results:  $Ra_{crit}$  vs.  $S$  for annular systems with  $A = 1.28$ .

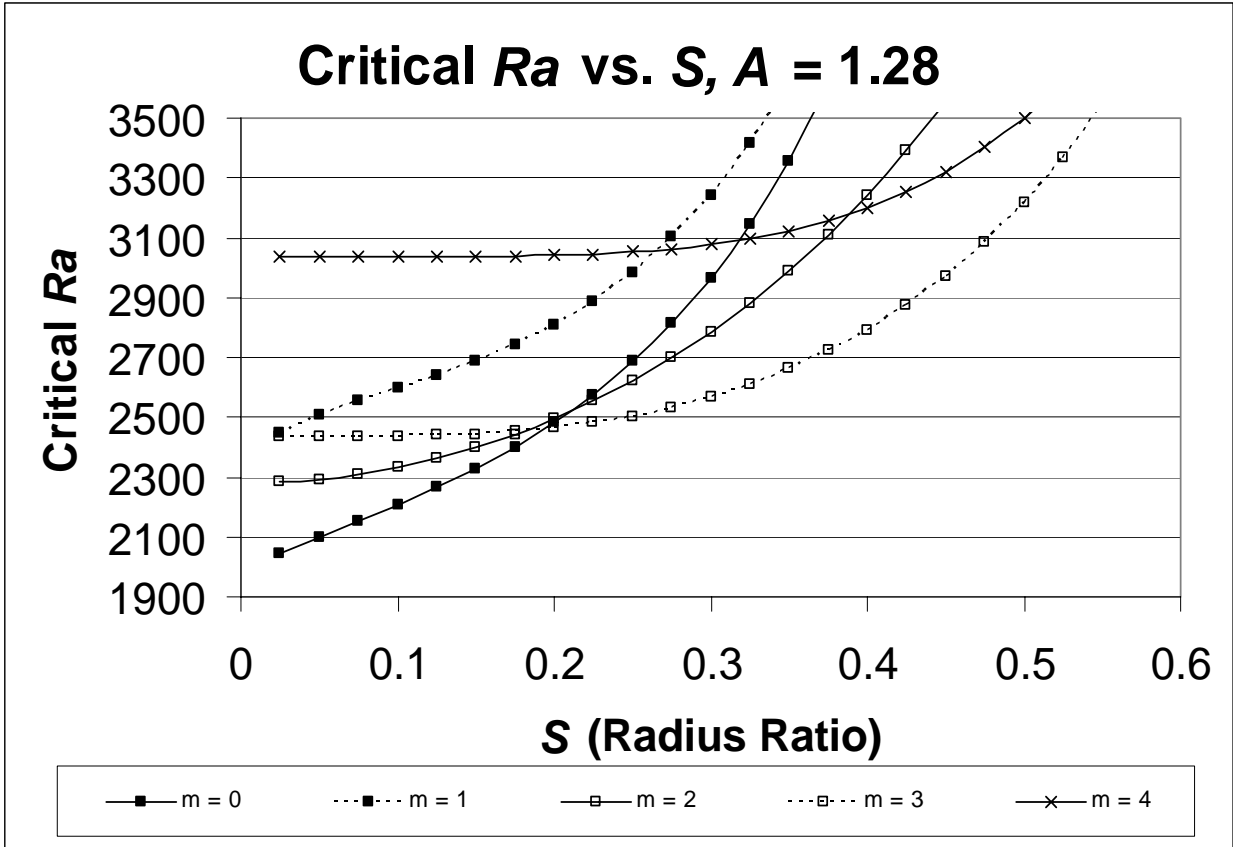


Figure 7-11. Constant viscosity computational results:  $Ra_{crit}$  vs.  $S$  for annular systems with  $A = 1.28$ , close-up view.

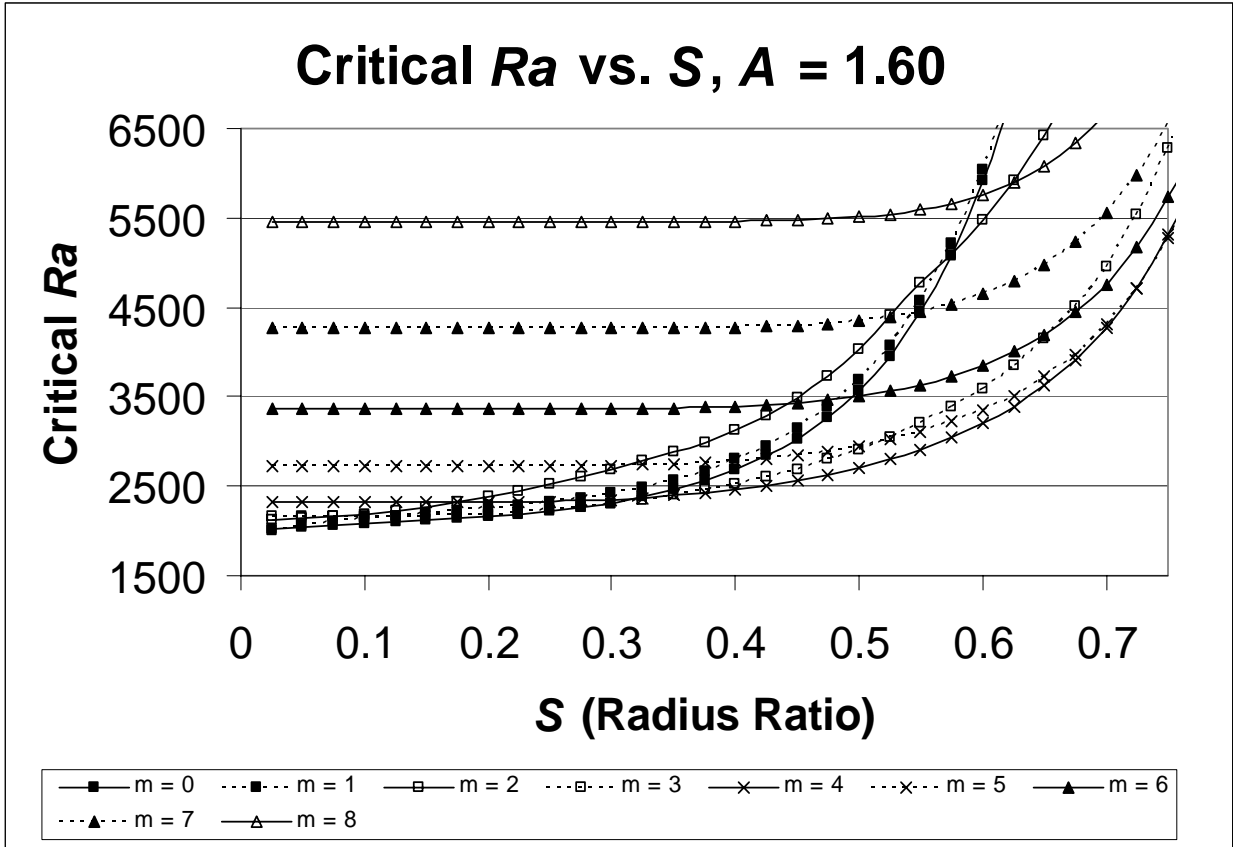


Figure 7-12. Constant viscosity computational results:  $Ra_{crit}$  vs.  $S$  for annular systems with  $A = 1.60$ .

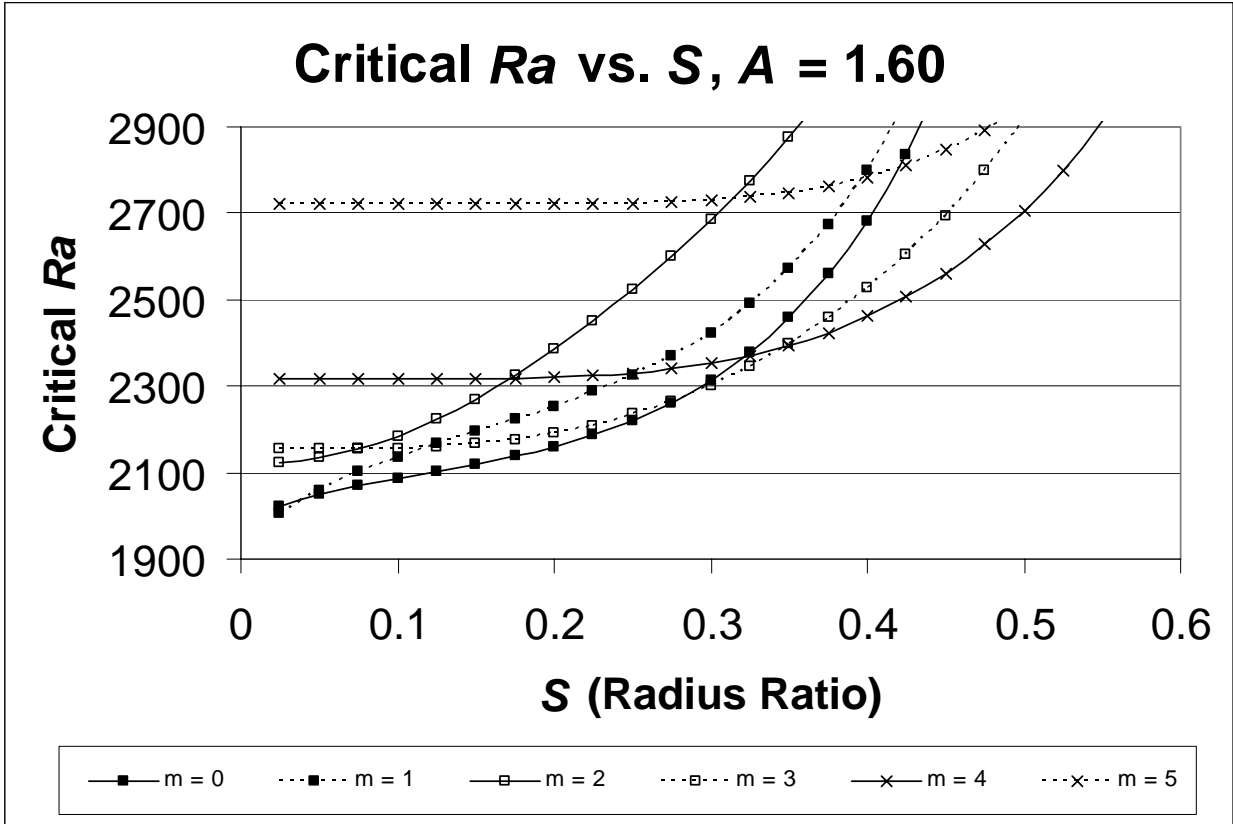


Figure 7-13. Constant viscosity computational results:  $Ra_{crit}$  vs.  $S$  for annular systems with  $A = 1.60$ , close-up view.

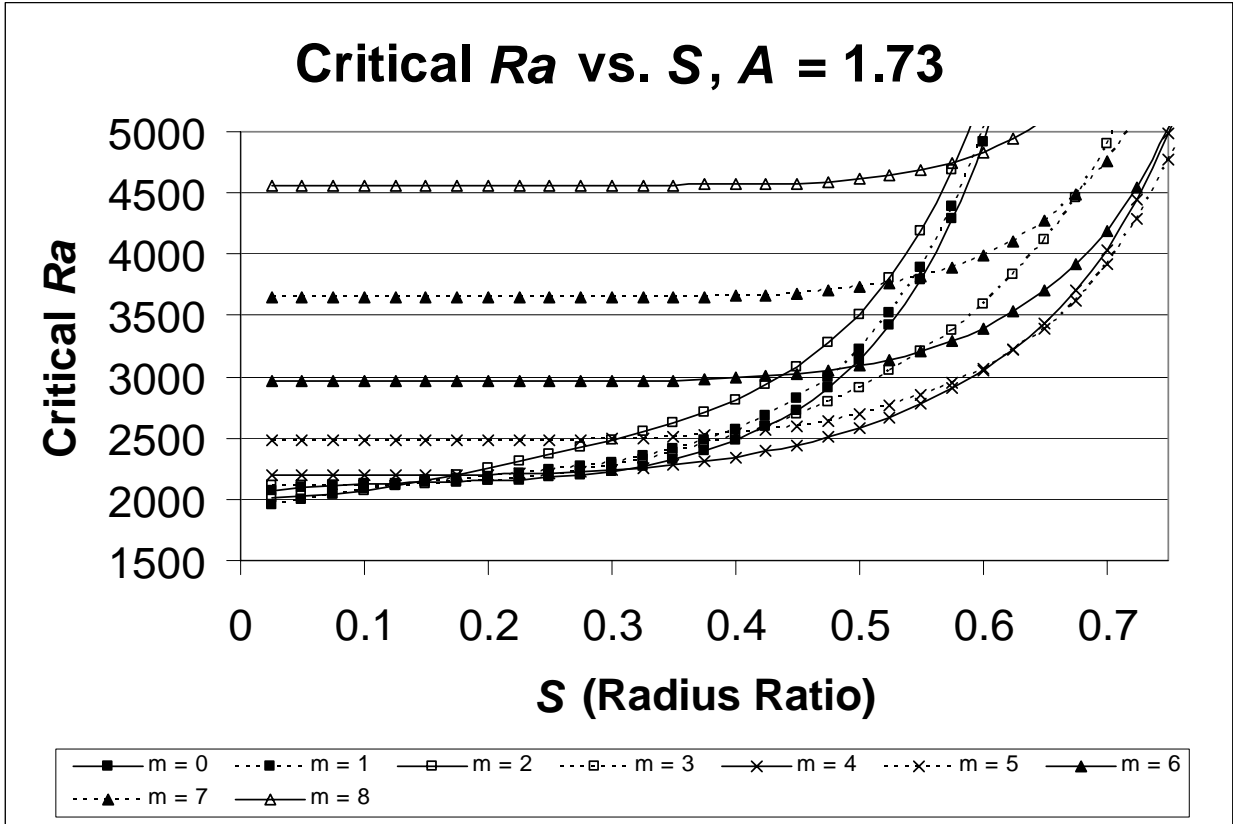


Figure 7-14. Constant viscosity computational results:  $Ra_{crit}$  vs.  $S$  for annular systems with  $A = 1.73$ .

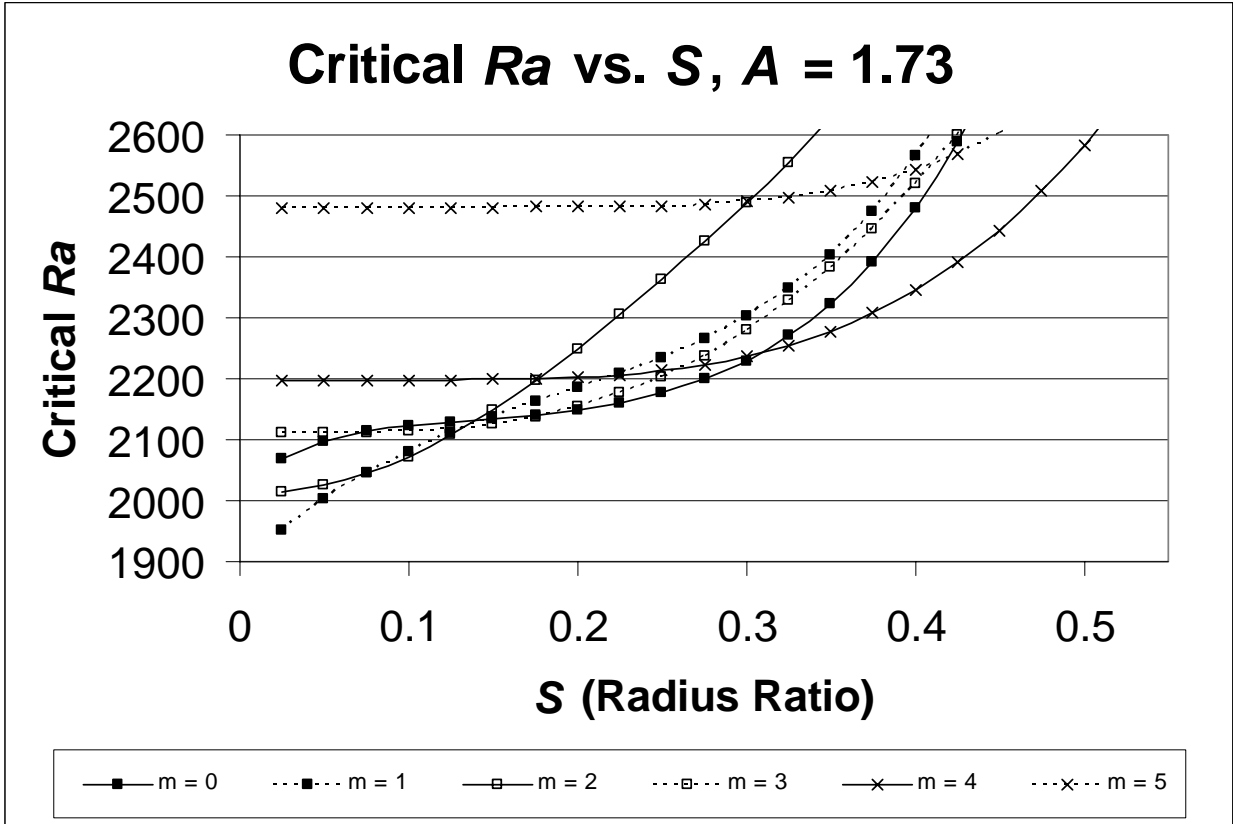


Figure 7-15. Constant viscosity computational results:  $Ra_{crit}$  vs.  $S$  for annular systems with  $A = 1.73$ , close-up view.

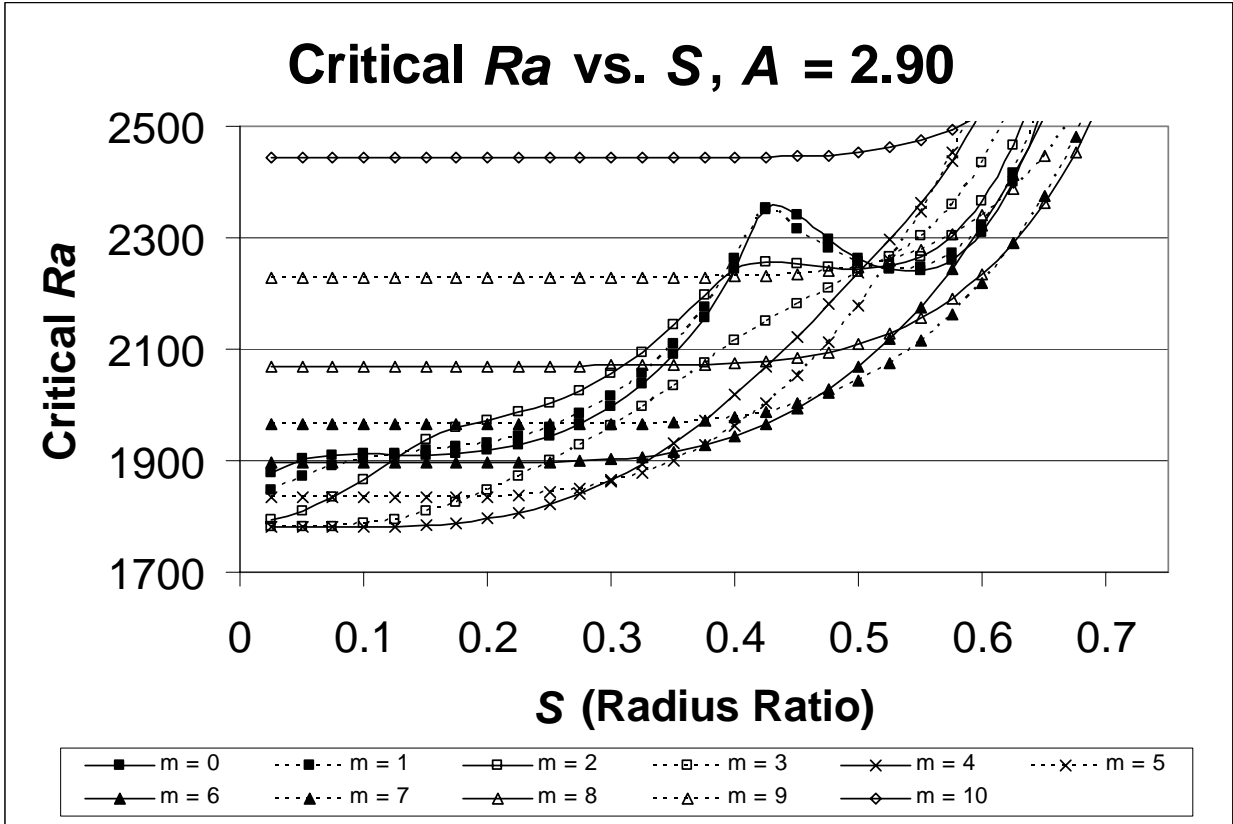


Figure 7-16. Constant viscosity computational results:  $Ra_{crit}$  vs.  $S$  for annular systems with  $A = 2.90$ .

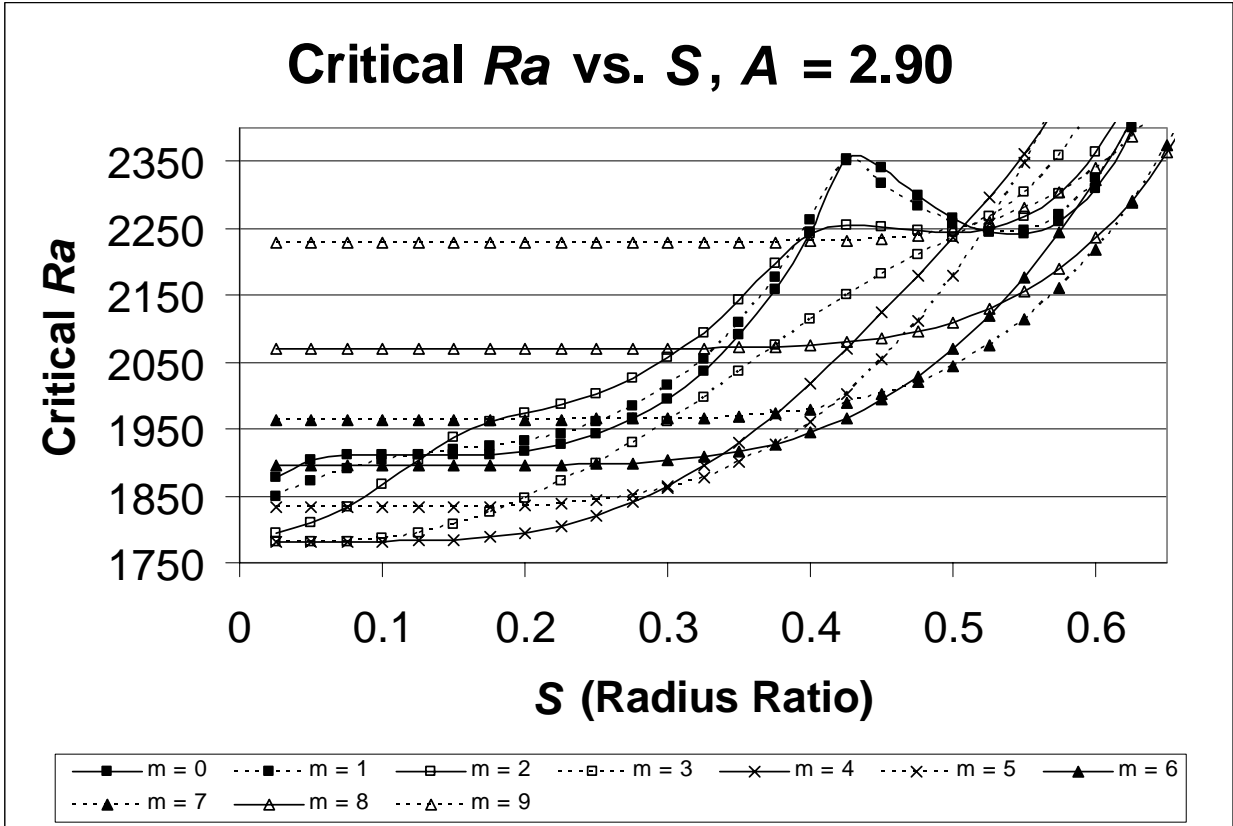


Figure 7-17. Constant viscosity computational results:  $Ra_{crit}$  vs.  $S$  for annular systems with  $A = 2.90$ , close-up view.

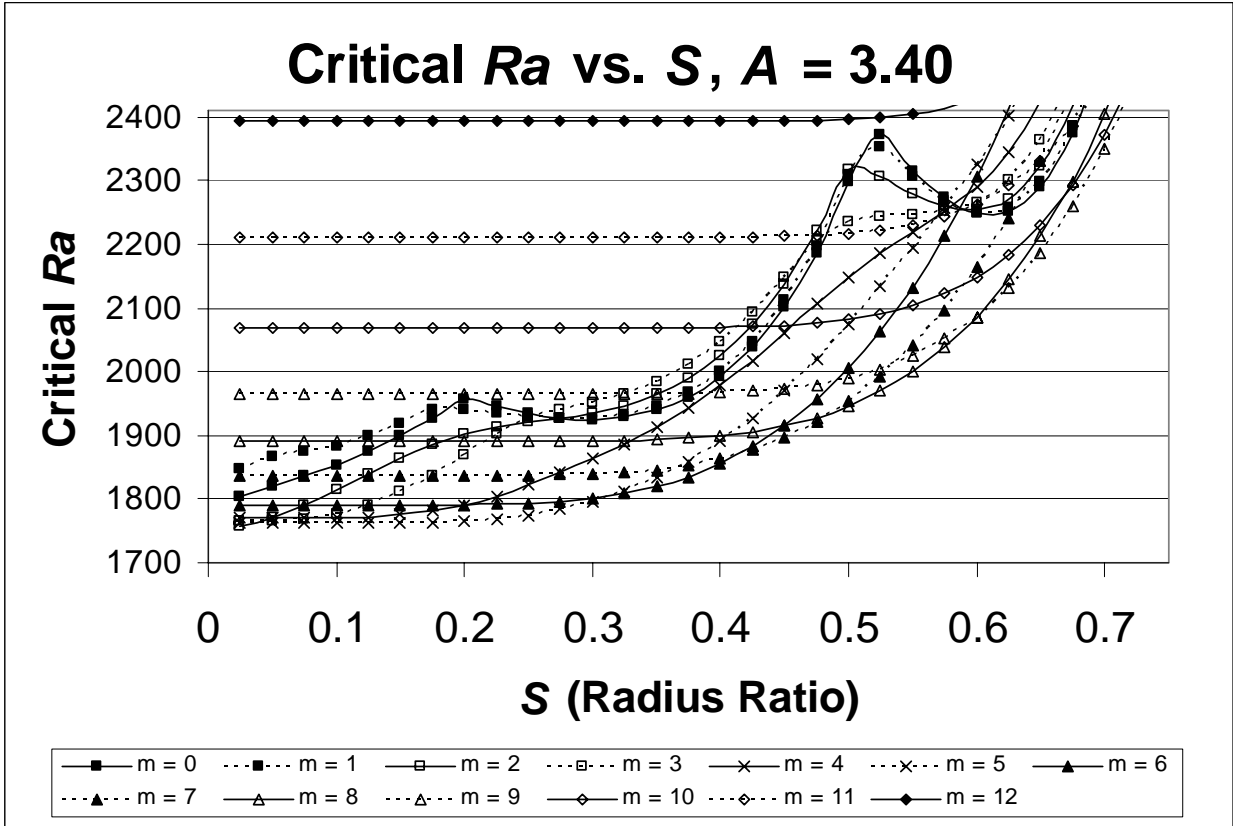


Figure 7-18. Constant viscosity computational results:  $Ra_{crit}$  vs.  $S$  for annular systems with  $A = 3.40$ .

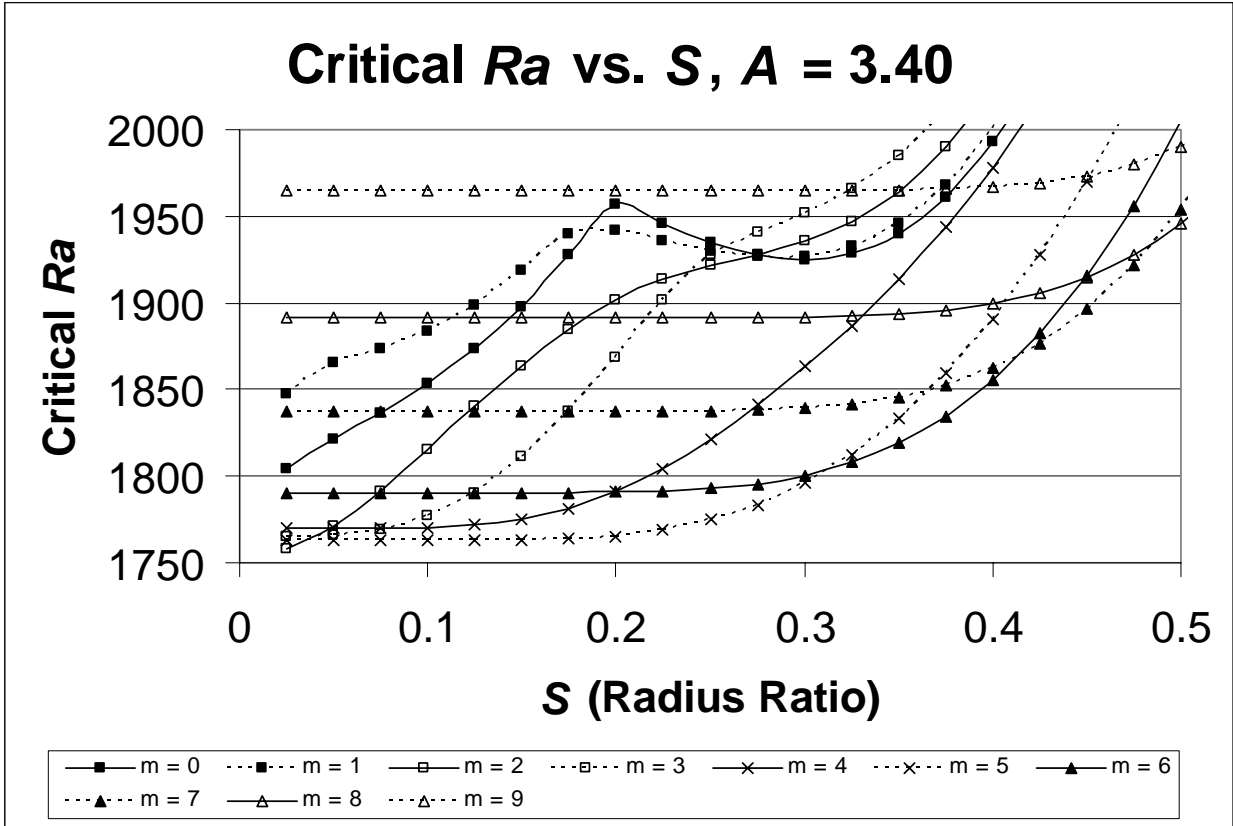


Figure 7-19. Constant viscosity computational results:  $Ra_{crit}$  vs.  $S$  for annular systems with  $A = 3.40$ , close-up view 1.

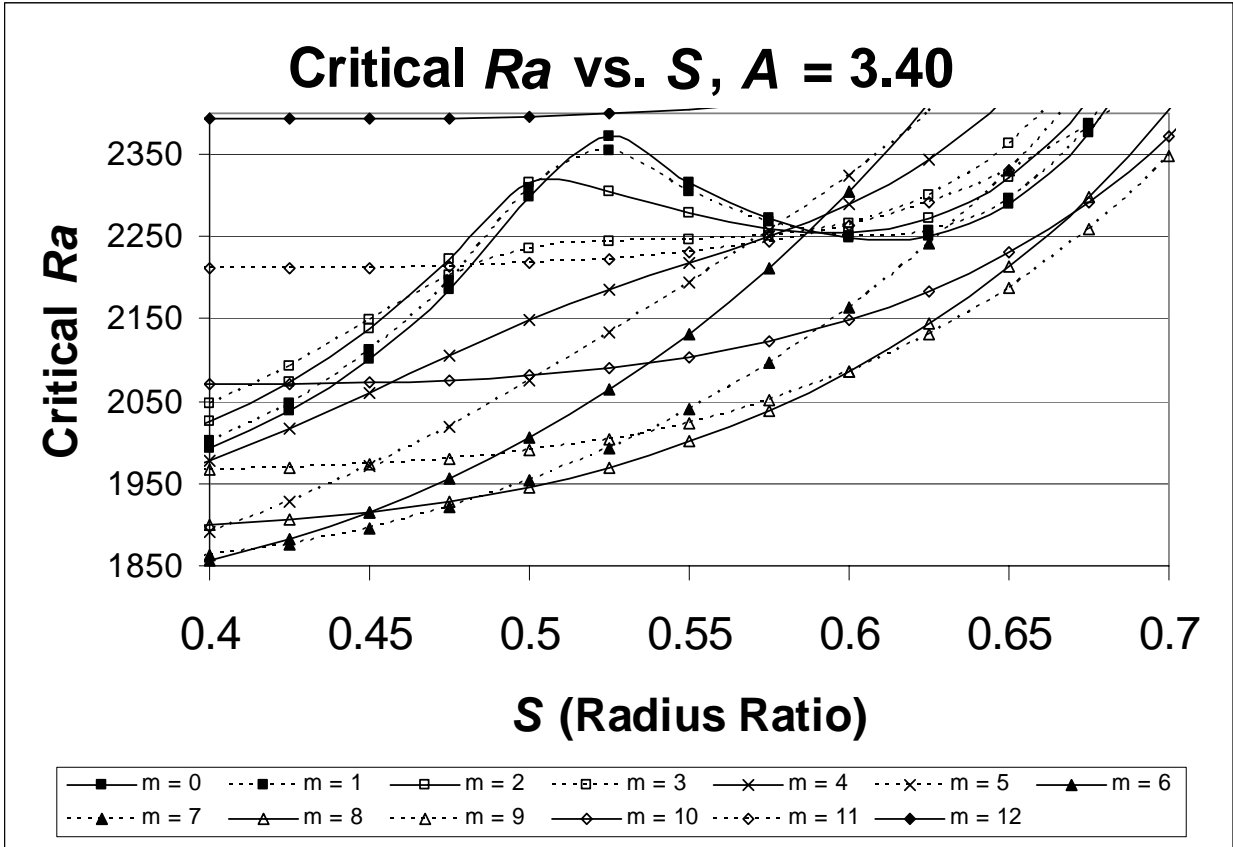


Figure 7-20. Constant viscosity computational results:  $Ra_{crit}$  vs.  $S$  for annular systems with  $A = 3.40$ , close-up view 2.

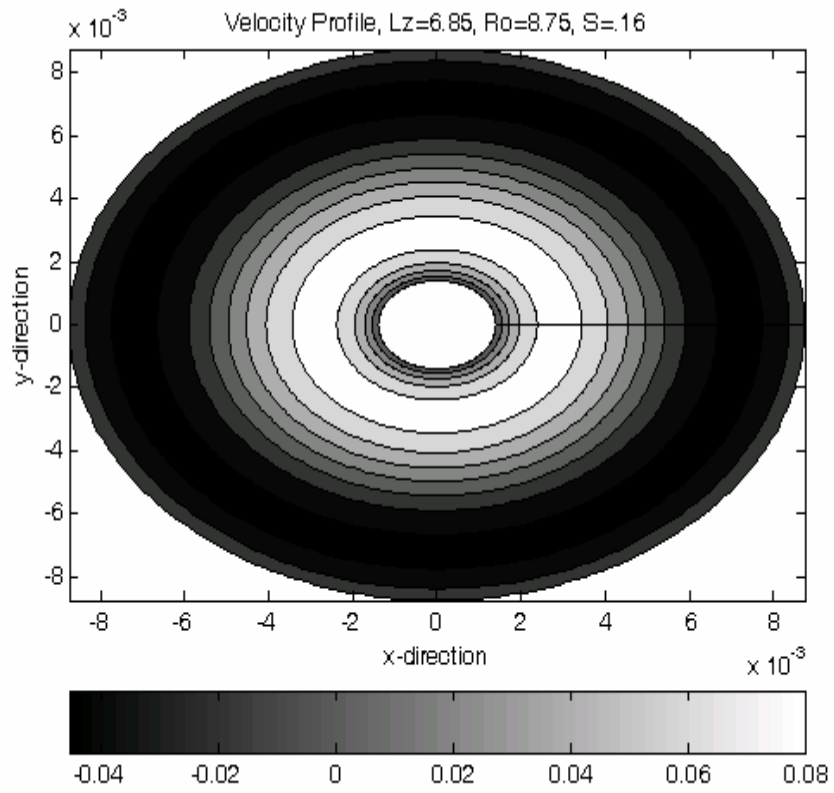


Figure 7-21. Computed velocity profile, cross-sectional view,  $L_z = 6.85$  mm,  $R_o = 8.75$  mm,  $S = .16$ ,  $m = 0:(0,1)$ ,  $[\Delta T]_{\text{crit}} = 7.08$  °C.

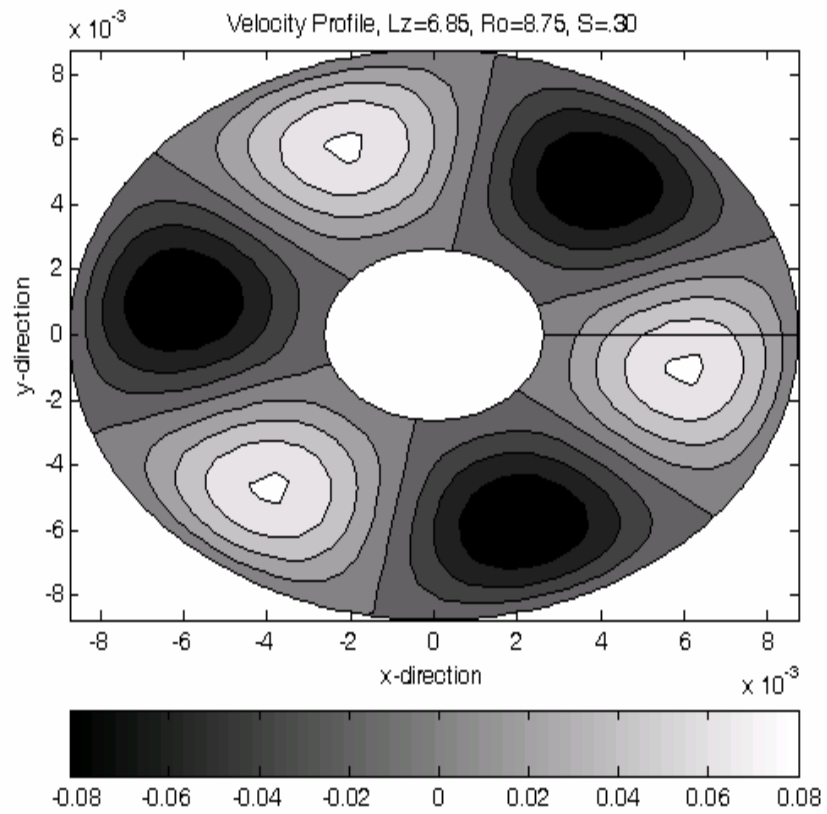


Figure 7-22. Computed velocity profile, cross-sectional view,  $L_z = 6.85$  mm,  $R_o = 8.75$  mm,  $S = .30$ ,  $m = 3:(3,0)$ ,  $[\Delta T]_{\text{crit}} = 7.67$  °C.

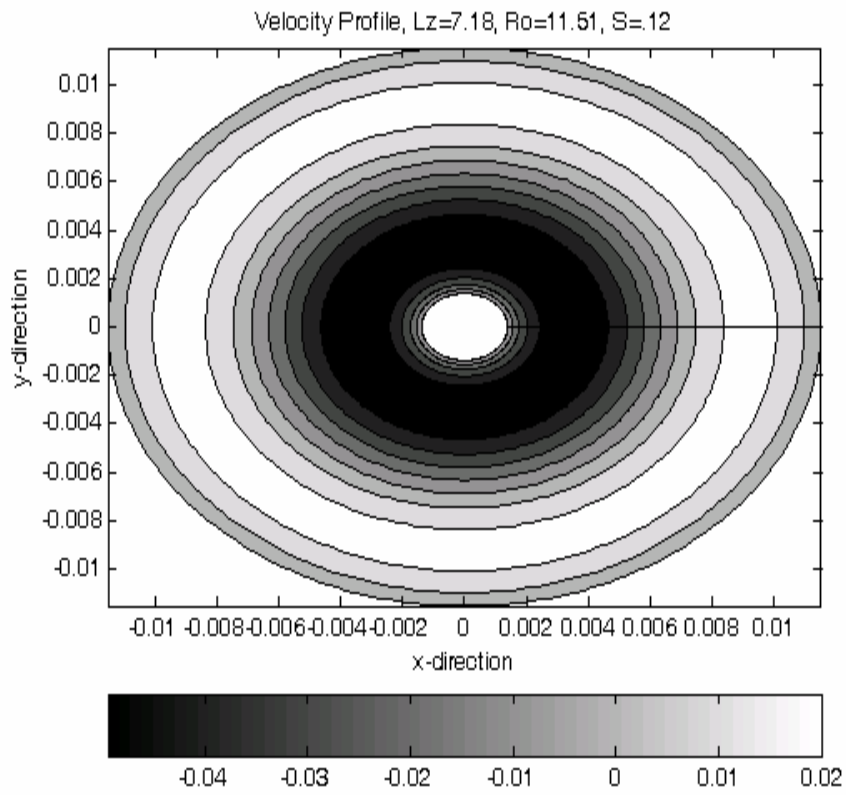


Figure 7-23. Computed velocity profile, cross-sectional view,  $L_z = 7.18$  mm,  $R_o = 11.51$  mm,  $S = .12$ ,  $m = 0:(0,1)$ ,  $[\Delta T]_{crit} = 5.57$  °C.

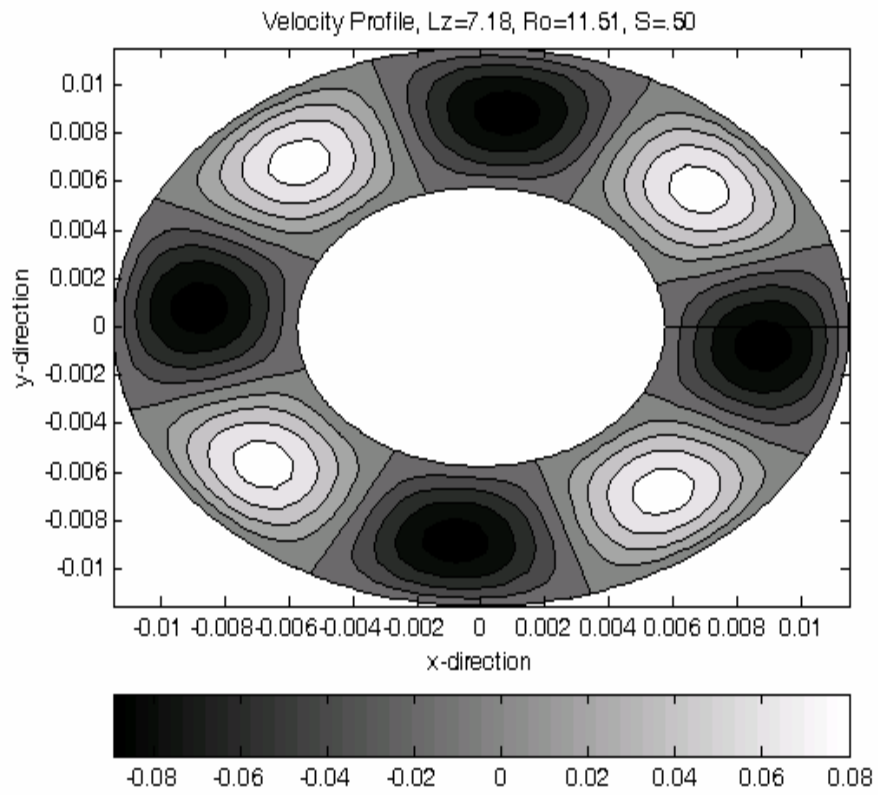


Figure 7-24. Computed velocity profile, cross-sectional view,  $L_z = 7.18$  mm,  $R_o = 11.51$  mm,  $S = .50$ ,  $m = 4:(4,0)$ ,  $[\Delta T]_{\text{crit}} = 7.09$  °C.

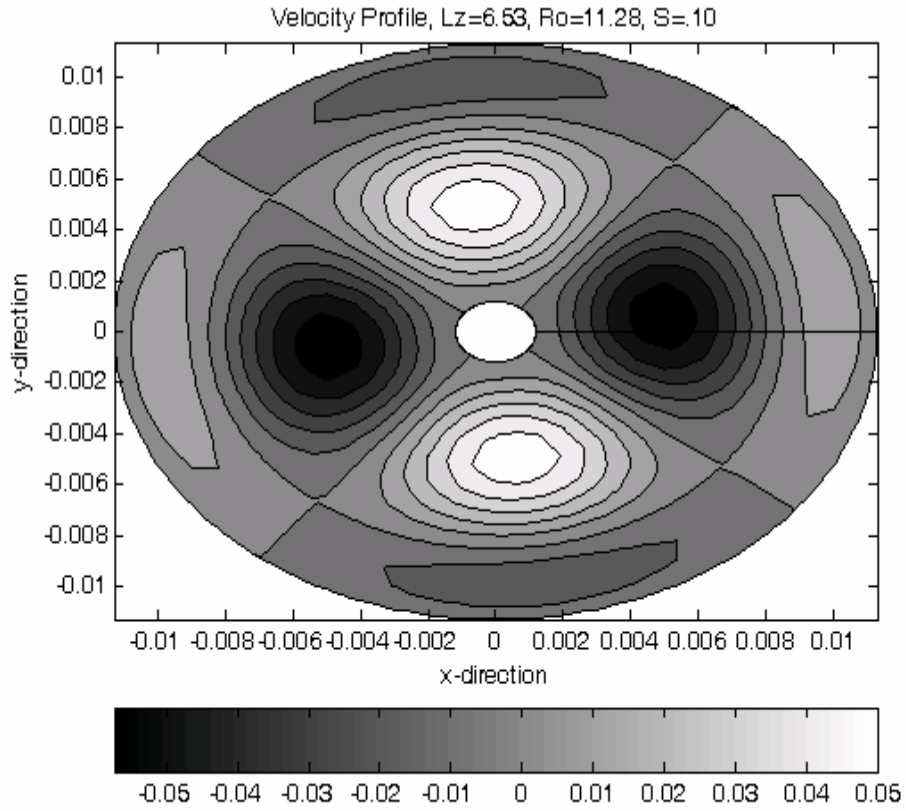


Figure 7-25. Computed velocity profile, cross-sectional view,  $L_z = 6.53$  mm,  $R_o = 11.28$  mm,  $S = .10$ ,  $m = 2:(2,1)$ ,  $[\Delta T]_{crit} = 7.21$  °C.

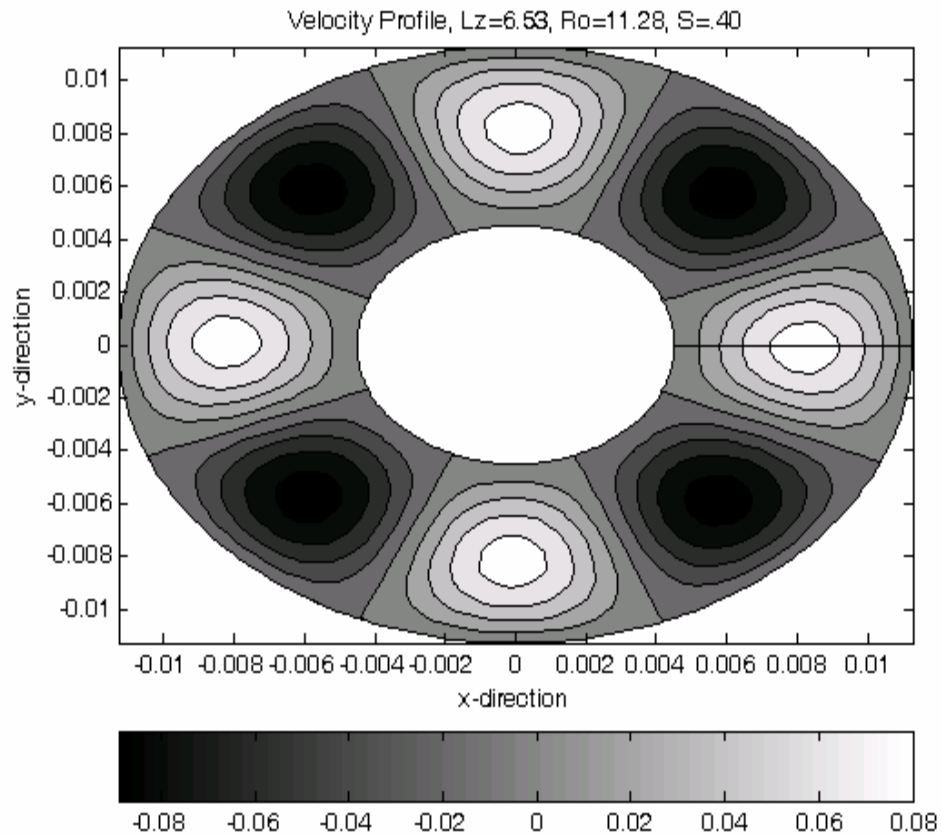


Figure 7-26. Computed velocity profile, cross-sectional view,  $L_z = 6.53$  mm,  $R_o = 11.28$  mm,  $S = .40$ ,  $m = 4:(4,0)$ ,  $[\Delta T]_{crit} = 8.07$  °C.

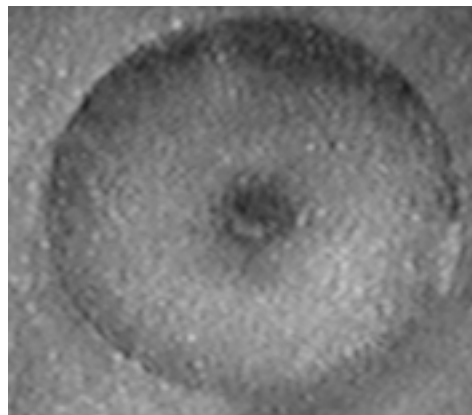


Figure 7-27. Photo of onset flow pattern,  $L_z = 6.85$  mm,  $R_o = 8.75$  mm,  $S = .16$ ,  $m = 0:(0,1)$ .

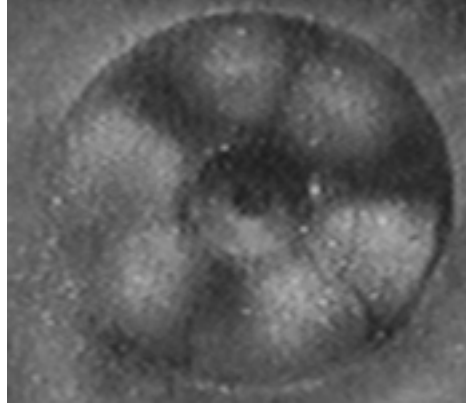


Figure 7-28. Photo of onset flow pattern,  $L_z = 6.85$  mm,  $R_o = 8.75$  mm,  $S = .30$ ,  $m = 3:(3,0)$ .

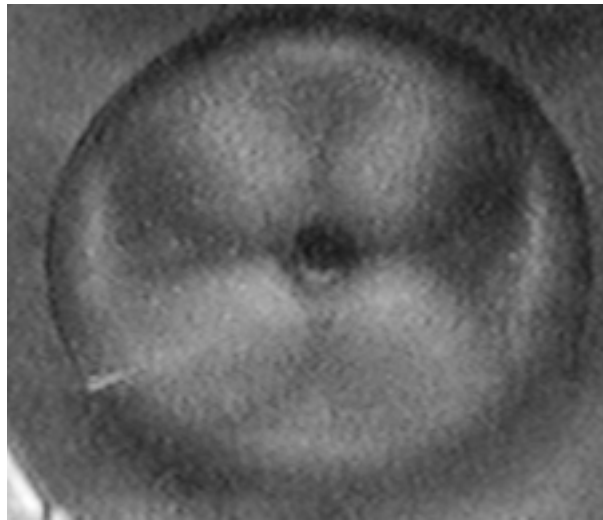


Figure 7-29. Photo of onset flow pattern,  $L_z = 7.18$  mm,  $R_o = 11.51$  mm,  $S = .12$ ,  $m = 2:(2,1)$ .

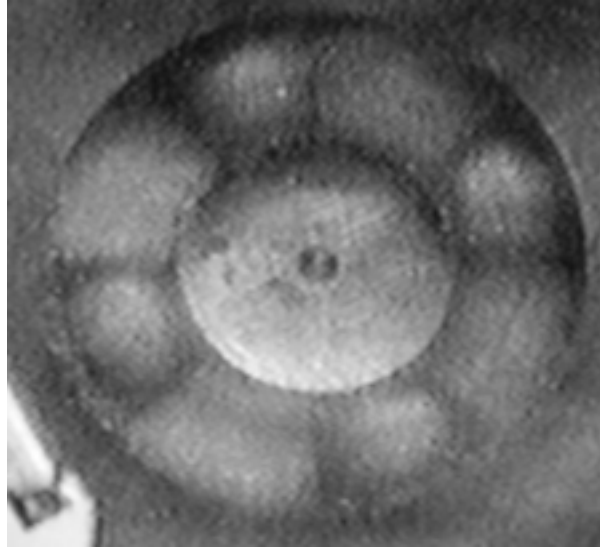


Figure 7-30. Photo of onset flow pattern,  $L_z = 7.18$  mm,  $R_o = 11.51$  mm,  $S = .50$ ,  $m = 4:(4,0)$ .

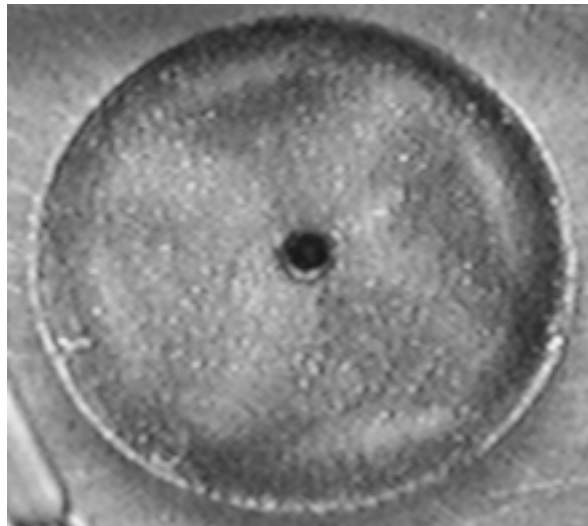


Figure 7-31. Photo of onset flow pattern,  $L_z = 6.53$  mm,  $R_o = 11.28$  mm,  $S = .10$ ,  $m = 2:(2,1)$ .

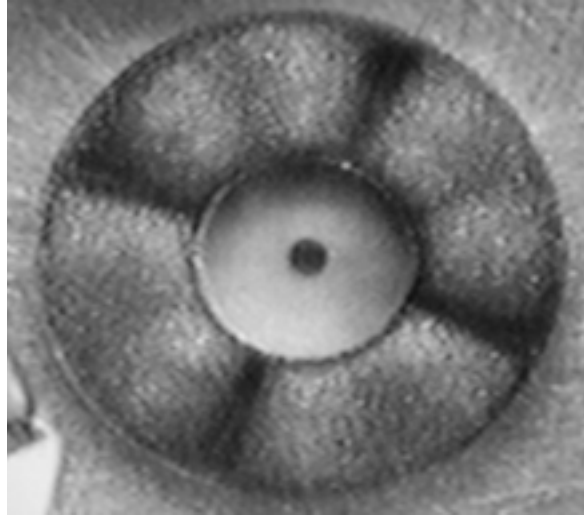


Figure 7-32. Photo of onset flow pattern,  $L_z = 6.53$  mm,  $R_o = 11.28$  mm,  $S = .40$ ,  $m = 4:(4,0)$ .

## CHAPTER 8 CONCLUSIONS AND POSSIBLE FUTURE STUDIES

This chapter will first summarize some important findings of this research, and will then mention some possible future work that could be done in this area.

### 8.1 Summary

The critical temperature differences determined by the non-constant viscosity computations were generally higher than those determined by the constant viscosity computations. As expected, since they more realistically model the experimental system, in all cylindrical and annular cases, the non-constant viscosity computations more closely match the experimental results than do the constant viscosity computations.

Carrying out computations for the critical conditions in cylindrical systems shows, also as expected, that the onset flow patterns in systems of larger aspect ratio include larger numbers of convective rolls so that they can spatially fill the test section in a more energetically favorable manner. Even though it was known already, it is notable that the relation between the aspect ratio and the critical Rayleigh number, for all azimuthal wave numbers, in constant viscosity cylindrical systems, is identical regardless of the exact dimensions of the system or the thermophysical properties of the system. The agreement between computations and experiments for cylindrical systems is very good in all cases considered.

The progression of onset flow patterns with changing system dimensions in the annular case is a bit more complex. Still, similar to what was seen in cylindrical systems, the relations between the radius ratio, the aspect ratio, and the critical Rayleigh number in constant viscosity annular systems are again identical, for all azimuthal wave numbers, regardless of the exact system dimensions or thermophysical properties. As explained, this is due to the time-independence of the system at the onset of convection.

In annular systems with small  $S$  values, as the center-block becomes very small in diameter, the onset flow pattern is the same as the onset pattern in the corresponding cylindrical system. In the cylindrical cases considered in this research, onset flow patterns of the azimuthal wave numbers  $m = 0, 1, \text{ and } 2$  are most common, and it is generally these onset patterns which are seen in the annular systems with very small  $S$  values. Onset flow patterns with higher azimuthal wave numbers generally occurred in systems with larger  $S$  values. In the annular systems considered in this research, the onset patterns with azimuthal wave numbers 0, 1, and 2 typically included radially aligned convective rolls as opposed to only azimuthally aligned rolls, and onset patterns with higher azimuthal wave numbers typically included only azimuthally aligned rolls. At high  $S$  values (greater than .30, for example), a higher  $S$  value generally corresponds to a higher azimuthal wave number.

The number of radially aligned convective rolls included in the onset flow pattern is generally lower at higher radius ratios (because at higher radius ratios, the annular gap width is smaller and there is not as much room for the radial motions of the radially aligned rolls). Changes in the number of radially aligned rolls present in the onset flow pattern for a given azimuthal wave number can be indicated by inflections in the curve for that azimuthal wave number on a stability diagram, though not all inflections indicate changes in the number of radially aligned rolls.

The numbers azimuthally and radially aligned convective rolls which form at onset in an annular system are also dependent upon the aspect ratio of the system. An annular system with a larger aspect ratio will, of course, tend to have onset flow patterns with larger numbers of azimuthally and radially aligned convective rolls because there is simply more space within which they may form and flow.

Better agreement between the critical temperature differences determined by computations and those determined by experiments is seen for the annular cases with smaller  $S$  values. The suspected reason for the poorer agreement when the annular center-block is larger is that slight imperfections in the centering of the annular center-block within the outer annular wall are having a significant stabilizing effect on the system. It is also suspected, then, that the strength of this stabilizing effect is dependent on the originally intended gap width in each case, and that the effect should be more pronounced when the gap width is smaller. The reasoning behind this is explained in Chapter 7, and, essentially, it is that the strong resistance to flow provided by the region of smallest annular gap width in an annular system with a slightly off-centered center-block stabilizes the entire system. The convective behavior of an annular system with a slightly off-centered center-block is very interesting from the standpoint of physics, and it is certainly a topic open to further interpretation and study. The experimental results agree with the hypothesis that stabilizing effect introduced to annular systems by slight off-centering of the center-block is stronger in cases for which the originally intended annular gap width is smaller. Also, in one case (see Table 7-8), the onset flow pattern predicted by computation was not the pattern seen experimentally. This is likely to be a consequence of either the off-centering effect just mentioned, or some other small experimental imperfection.

## **8.2 Future Studies**

Many parameters in an annular problem could be varied in order to examine their effects on the stability of the system. One of the most obvious parameters to investigate, which has become of particular interest based on the results of the experiments for this research, is the off-centering of the annular center-block. It is suspected that off-centering the annular center-block should increase the stability of the system to buoyancy-driven convection. It is not so easily

predictable, though, how this would affect the onset flow patterns, except that it would make axisymmetric onset patterns impossible.

It would also be interesting to run experiments on annular systems with extremely small center-blocks, to see just how close the critical conditions can get to those for corresponding open cylindrical systems.

Another great study would be to investigate Rayleigh convection in an annular system using a liquid metal as a test fluid. Such a study would better represent the thermophysical properties in a crystal growth system. This would simply require choosing a metal that is liquid within a range of temperatures that would be manageable from an experimental standpoint, and that has thermophysical properties that, in some way, are similar to those of an industrially important liquid metal. A study of Rayleigh and Marangoni convection in an annular system with multiple vertically-stacked fluid layers could be applied quite directly to crystal growth applications, as well.

Lastly, nonlinear calculations would provide valuable information about the convective behavior of an annular system that the linearized computations shown here simply cannot provide. They would allow the determination of supercritical flow behaviors, as well as the exact velocities in the system.

Hopefully some of these problems will be addressed, because they have potential to be very interesting and could be very useful in the crystal growth industry.

## APPENDIX A THERMOPHYSICAL PROPERTIES

As mentioned, the dependence of viscosity on temperature was determined using a Cole-Parmer<sup>®</sup> 98936 series viscometer. Essentially, what was involved in doing this was to measure the viscosity of the oil at a range of temperatures between approximately 20.0 °C and 50.0 °C, with increments of 1.0 °C near the middle of the range, and increments of 2.0 °C near the low and high ends of the range. Each measured viscosity value came from a measurement of the shearing effect created by rotating a metal spindle in a temperature-controlled chamber full of the silicone oil. The temperature of the oil chamber was regulated by circulating temperature-controlled water around it. The temperature of the circulating water was accurately controlled by the large NESLAB water bath.

Except for the viscosity values, the silicone oil properties in Table A-1 are based on information provided by Dow Corning. In this research, the density and viscosity are the only properties being assumed to vary significantly with temperature (for Dow Corning 200 1 Stoke silicone oil, the variation with temperature in the other thermophysical properties of interest is not significant). Thus, a temperature corresponding to the thermophysical property value is shown only for those properties.

Table A-1. Thermophysical properties.

Material Properties	Dow Corning 200 <sup>®</sup>			
	1 Stoke Silicone Oil	Lucite	Copper	Sapphire
Density (kg/m <sup>3</sup> ) at 25 °C	964	-----	-----	-----
Thermal Conductivity (W/(m*(°C)))	0.154808	0.17 <sup>+++</sup>	401 <sup>+++</sup>	36.8192 <sup>++++</sup>
Dynamic Viscosity (kg/(m*s)), (T in °C) <sup>+</sup>	$\mu (T) = .147105008 * e^{-.017975325 * T}$	-----	-----	-----
Kinematic Viscosity (m <sup>2</sup> /s) at 35 °C <sup>++</sup>	$8.134296 * 10^{-5}$	-----	-----	-----
Thermal Diffusivity (m <sup>2</sup> /s)	$1.09039 * 10^{-7}$	-----	-----	-----
Thermal Expansion Coefficient (°C <sup>-1</sup> )	$9.6 * 10^{-4}$	-----	-----	-----

<sup>+</sup>: The function for the dependence of dynamic viscosity on temperature is based on viscosity measurements taken by the author over a range of temperatures, using a Cole-Parmer<sup>®</sup> 98936 series viscometer. This is the varying viscosity which was used in calculations in which viscosity's variation with temperature was considered.

<sup>++</sup>: The kinematic viscosity value given here is based on viscosity measurements taken by the author over a range of temperatures, using a Cole-Parmer<sup>®</sup> 98936 series viscometer. This is the constant kinematic viscosity value which was used in calculations in which viscosity's variation with temperature was not considered.

<sup>+++</sup>: As shown in Duane Johnson's dissertation (Johnson 1997).

<sup>++++</sup>: As shown in the 1974 paper by Koschmieder's and Pallas (Koschmieder & Pallas 1974).

APPENDIX B  
ADDITIONAL EXPLANATION OF EQUATIONS

The following section provides further explanation of the modeling equations and some of the modifications made to them.

**B.1 Boussinesq Approximation**

Obviously, for Rayleigh convection to be possible in a fluid, the fluid cannot be strictly incompressible (density must vary with temperature). The Boussinesq approximation allows a fluid to be treated as incompressible in all terms of the momentum equation except those relating to buoyancy forces. The approximation requires that the variation of density with temperature be accounted for only in the terms in which density is multiplied by gravitational acceleration; this is because, in any other terms, the effect of this density variation will be incomparably small in magnitude. The Boussinesq approximation is applied to Equation 3.1, which is

$$\rho \frac{\partial \bar{v}}{\partial t} + \rho \bar{v} \cdot \nabla \bar{v} = -\nabla P + \rho \bar{g} + \nabla \cdot \bar{S}, \quad (3.1)$$

so that it becomes

$$\rho_R \frac{\partial \bar{v}}{\partial t} + \rho_R \bar{v} \cdot \nabla \bar{v} = -\nabla P + \rho_R \left(1 + \frac{1}{\rho_R} \frac{\partial \rho}{\partial T} \Big|_{T_R} (T - T_R)\right) \bar{g} + \nabla \cdot \bar{S}, \quad (B.1)$$

in which  $T_R$  and  $\rho_R$  are the reference temperature and density, respectively.

The density variation term in this equation can be simplified by introducing the volumetric thermal expansion coefficient,  $\alpha$ , which is

$$\alpha = -\frac{1}{\rho_R} \frac{\partial \rho}{\partial T} \Big|_{T_R}. \quad (B.2)$$

The volumetric thermal expansion coefficient is positive when the derivative of density with respect to temperature is negative. The momentum equation may then be written as

$$\rho_R \frac{\partial \bar{v}}{\partial t} + \rho_R \bar{v} \cdot \nabla \bar{v} = -\nabla P + \rho_R (1 - \alpha(T - T_R)) \bar{g} + \nabla \cdot \bar{S}. \quad (3.5)$$

Once the Boussinesq approximation has been applied, a valid solution can be obtained only if the magnitude of the product of  $\alpha$  and  $\Delta T$  is much smaller than one, where  $\Delta T$  is the temperature difference from one vertical boundary of the fluid layer to the other. It can be seen by examining the thermophysical properties of the test fluids used in this study, and considering the typical critical vertical temperature differences seen in this study, that the magnitude of  $\alpha$  is sufficiently small that  $\alpha * \Delta T$  will be much smaller than one. Also, to obtain a valid solution using the Boussinesq approximation, the magnitude of  $(\Delta \rho) / \rho_R$  must be much smaller than one, in which  $\Delta \rho$  is the difference in density from one vertical boundary of the fluid layer to the other. The system of equations is being solved to determine the critical temperature difference at the onset of convection, and at the onset of convection, the difference in density from one vertical boundary of the fluid layer to the other is quite small. An example of a situation in which the Boussinesq approximation is not valid is convection in stars. Stars convect inward due to their own gravitational forces and their values for the magnitude of  $(\Delta \rho) / \rho_R$  are not much smaller than one.

## **B.2 Nonlinearities in the Governing Equations**

For the system of Equations 3.2, 3.3, and 3.10 to have more solutions than the base state solution (motionless), a nonlinearity must be present. At that point, an important nonlinearity can be seen. As shown by Equation 3.10, velocity is a function of temperature. Thus, the  $\bar{v} \cdot \nabla T$  term in Equation 3.2 is nonlinear. Of course, the  $\bar{v} \cdot \nabla \bar{v}$  term in the momentum equation is nonlinear, as well. This nonlinearity is less important, though, because the system of equations is being solved for the critical temperature difference at the onset of convection and the

velocities are of very small magnitude at that time, making  $\bar{v} \cdot \nabla \bar{v}$  to be of negligibly small magnitude.

### **B.3 Characteristic Velocity and Characteristic Time**

In choosing which parameters are used to define the characteristic velocity ( $\bar{v}$ ) and characteristic time ( $\bar{t}$ ), the goal is to make the characteristic velocity as small as possible. This is done to ensure that all of the flow behavior of the system (even the smallest velocities) are mathematically captured. Thus, the characteristic velocity is chosen to be the ratio of the smaller of the kinematic viscosity and thermal diffusivity of the fluid phase to the largest depth (vertical height, annular gap width, or diameter) of the fluid phase. The characteristic time is then defined using the same parameters. The forms of the characteristic velocity and characteristic time are shown below, considering the example case that the fluid's thermal diffusivity ( $\kappa$ ) is smaller than its kinematic viscosity, and that the fluid is in a cylindrical container with a diameter ( $D$ ) larger than its vertical height; this situation was quite typical for the cylindrical cases considered during this research. The typical value for the characteristic velocity in the cylindrical cases in this research was

$$\bar{v} = \frac{\kappa}{D}, \tag{B.3}$$

and the typical value for the characteristic time in the cylindrical cases in this research was

$$\bar{t} = \frac{D^2}{\kappa}. \tag{B.4}$$

Since the characteristic time and velocity can be defined in several ways depending on the thermophysical properties and dimensions of the fluid phase, the parameters used to define them will not be specified here.

APPENDIX C  
DEVELOPMENT OF MATHEMATICAL MODEL FOR THE CONSTANT VISCOSITY  
CASE

This section of the appendix presents the mathematical development of the modeling equations for the case in which the viscosity of the fluid is assumed to be constant with respect to temperature. As mentioned earlier, the viscosity value used throughout the constant viscosity calculation is the value at 35.0 °C, which is given in Appendix A. The development shown here is parallel to what is given in Chapters 3 and 4, even though it is presented more concisely. Note that the symbols used here are defined and explained in Chapters 3 and 4.

**C.1 Nonlinear Equations**

For this case, the original set of domain equations appears the same as it did in Chapter 3. This original set of domain equations includes the momentum equation, the energy equation, and the continuity equation, which, respectively, are

$$\rho \frac{\partial \bar{v}}{\partial t} + \rho \bar{v} \cdot \nabla \bar{v} = -\nabla P + \rho \bar{g} + \nabla \cdot \bar{\bar{S}}, \quad (\text{C.1})$$

$$\rho C_v \frac{\partial T}{\partial t} + \rho C_v \bar{v} \cdot \nabla T = k \nabla^2 T, \quad (\text{C.2})$$

$$\frac{\partial \rho}{\partial t} = \nabla \cdot (\rho \bar{v}). \quad (\text{C.3})$$

Again, the stress tensor,  $\bar{\bar{S}}$ , can be expanded as

$$\bar{\bar{S}} = 2\mu \left[ \frac{\nabla \bar{v} + (\nabla \bar{v})^T}{2} \right]. \quad (\text{C.4})$$

Applying the Boussinesq approximation brings the momentum equation into the form

$$\rho_R \frac{\partial \bar{v}}{\partial t} + \rho_R \bar{v} \cdot \nabla \bar{v} = -\nabla P + \rho_R (1 - \alpha(T - T_R)) \bar{g} + \nabla \cdot \bar{\bar{S}}. \quad (\text{C.5})$$

The Boussinesq approximation results in the disappearance of the time-derivative term of the continuity equation, as well. Defining a modified pressure, which is

$$-\nabla p = -\nabla P + \rho_R \bar{g}, \quad (\text{C.6})$$

further simplifies the momentum equation so that it becomes

$$\rho_R \frac{\partial \bar{v}}{\partial t} + \rho_R \bar{v} \cdot \nabla \bar{v} = -\nabla p - \rho_R \alpha (T - T_R) \bar{g} + \nabla \cdot \bar{S}. \quad (\text{C.7})$$

Now, substituting the expansion of the stress tensor into the momentum equation, and considering a constant viscosity, brings the momentum equation into the following familiar form:

$$\rho_R \frac{\partial \bar{v}}{\partial t} + \rho_R \bar{v} \cdot \nabla \bar{v} = -\nabla p - \rho_R \alpha (T - T_R) \bar{g} + \mu \nabla^2 \bar{v}. \quad (\text{C.8})$$

Since this calculation does not include the variation of viscosity with temperature, the dynamic viscosity at the reference temperature may be used as the dynamic viscosity in all equations, meaning that

$$\mu = \mu_R. \quad (\text{C.9})$$

As explained in Chapter 3, a total of sixteen boundary conditions are needed for the annular system, while only twelve are needed for the cylindrical system. The unscaled forms of these boundary conditions are

$$v_r = v_\theta = v_z = 0 \text{ at } z = 0, \quad (\text{C.10})$$

$$T = T_b \text{ at } z = 0, \quad (\text{C.11})$$

$$v_r = v_\theta = v_z = 0 \text{ at } z = L_z, \quad (\text{C.12})$$

$$T = T_t \text{ at } z = L_z, \quad (\text{C.13})$$

$$v_r = v_\theta = v_z = 0 \text{ at } r = R_o, \quad (\text{C.14})$$

$$\frac{\partial T}{\partial r} = 0 \text{ at } r = R_o, \quad (\text{C.15})$$

and, if considering an annular system,

$$v_r = v_\theta = v_z = 0 \text{ at } r = R_i, \quad (\text{C.16})$$

$$\frac{\partial T}{\partial r} = 0 \text{ at } r = R_i. \quad (\text{C.17})$$

## C.2 Scaling

A list of the scaling relations used is given next. Dimensionless variables are marked using the “hat” symbol, while the “bar” indicates a characteristic value for a variable. The scaling relations are

$$\hat{v} = \frac{v}{\bar{v}}, \quad (\text{C.18})$$

$$\hat{T} = \frac{T - T_R}{\Delta T}, \quad (\text{C.19})$$

$$\Delta T = T_b - T_t, \quad (\text{C.20})$$

$$\hat{p} = \frac{p}{\bar{p}}, \quad (\text{C.21})$$

$$\bar{p} = \frac{\mu_R \bar{v}}{L_z}, \quad (\text{C.22})$$

$$\hat{t} = \frac{t}{\bar{t}}, \quad (\text{C.23})$$

$$\hat{\nabla} = L_z \nabla. \quad (\text{C.24})$$

In this simple case, which does not consider the variation of viscosity with temperature,  $T_R$  will be chosen as the temperature at the top boundary of the system ( $T_t$ ). Applying these

scalings to the domain equations yields the following dimensionless (though the “hat” symbol will now be discarded) equations:

$$\frac{\rho_R L_z^2}{\mu_R \bar{t}} \frac{\partial \bar{v}}{\partial t} + \frac{\rho_R L_z \bar{v}}{\mu_R} \bar{v} \cdot \nabla \bar{v} = -\nabla p - \frac{\alpha L_z^2 \bar{g} (\Delta T)}{\nu \bar{v}} T + \nabla^2 \bar{v}, \quad (\text{C.25})$$

$$\frac{L_z^2}{\kappa \bar{t}} \frac{\partial T}{\partial t} + \frac{L_z \bar{v}}{\kappa} \bar{v} \cdot \nabla T = \nabla^2 T, \quad (\text{C.26})$$

$$0 = \nabla \cdot \bar{v}. \quad (\text{C.27})$$

As in Chapter 3, all thermophysical properties in these equations are at the reference temperature unless otherwise noted. The subscript “R” is not included on the symbols for all of these properties. It is, however, left on the symbols  $\rho_R$  and  $\mu_R$  in order to better imitate the procedure shown in Chapter 3.

Scaling leaves all boundary conditions on velocity, as well as the boundary conditions on temperature at the radial walls, unchanged. Scaling of the boundary conditions also leads to a simplification of the conditions on temperature at the top and bottom walls. Since the variation of viscosity with temperature is not being considered,  $T_R$  has simply been chosen as  $T_t$ , and it is this which allows a simplification. The simplified conditions on temperature at the top and bottom walls are

$$T = 1 \text{ at } z = 0, \quad (\text{C.28})$$

$$T = 0 \text{ at } z = L_z \quad (\text{C.29})$$

The reasoning for linearizing the system of modeling equations, and removing their time dependence, is explained thoroughly in Chapter 3. Here, this explanation is omitted and the focus is simply on the mathematical progression.

### C.3 Linearization

The form of the linearization expansion to be used is the same whether the variation of viscosity with temperature is being considered or not. Again, the system is linearized around its motionless base state. The form of the expansion, considering the example case of expanding the velocity, is

$$\begin{aligned} \bar{v} = & \left[ \bar{v} \Big|_{\varepsilon=0} \right] + \varepsilon \left[ \frac{\partial \bar{v}}{\partial \varepsilon} \Big|_{\varepsilon=0} \right] + \frac{1}{2!} \varepsilon^2 \left[ \frac{\partial^2 \bar{v}}{\partial \varepsilon^2} \Big|_{\varepsilon=0} \right] + \\ & \frac{1}{3!} \varepsilon^3 \left[ \frac{\partial^3 \bar{v}}{\partial \varepsilon^3} \Big|_{\varepsilon=0} \right] + \dots, \end{aligned} \quad (\text{C.30})$$

which may be rewritten as

$$\bar{v} = \bar{v}_0 + \varepsilon \bar{v}_1 + \frac{1}{2!} \varepsilon^2 \bar{v}_2 + \frac{1}{3!} \varepsilon^3 \bar{v}_3 + \dots \quad (\text{C.31})$$

The subscript “0” indicates values pertaining to the motionless base state, in which heat is transferred only in the vertical direction by conduction, and so the modeling equations may be simplified by the fact that  $\bar{v}_0$  is equal to zero. Applying this expansion to the modeling equations (which is actually the process of mathematically perturbing the equations with a small disturbance of magnitude  $\varepsilon$ ) results in the following set of linearized domain equations:

$$\frac{\rho_R L_z^2}{\mu_R \bar{t}} \frac{\partial \bar{v}_1}{\partial t} = -\nabla p_1 - \frac{\alpha L_z^2 \bar{g} (\Delta T)}{\nu \bar{v}} T_1 + \nabla^2 \bar{v}_1, \quad (\text{C.32})$$

$$\frac{L_z^2}{\kappa \bar{t}} \frac{\partial T_1}{\partial t} + \frac{L_z \bar{v}}{\kappa} \frac{\partial T_0}{\partial z} v_{1z} = \nabla^2 T_1, \quad (\text{C.33})$$

$$0 = \nabla \cdot \bar{v}_1. \quad (\text{C.34})$$

Linearizing the boundary conditions does not greatly change their appearance. The linearized boundary conditions are

$$v_{1r} = v_{1\theta} = v_{1z} = 0 \text{ at } z = 0, \quad (\text{C.35})$$

$$T_1 = 0 \text{ at } z = 0, \quad (\text{C.36})$$

$$v_{1r} = v_{1\theta} = v_{1z} = 0 \text{ at } z = L_z, \quad (\text{C.37})$$

$$T_1 = 0 \text{ at } z = L_z, \quad (\text{C.38})$$

$$v_{1r} = v_{1\theta} = v_{1z} = 0 \text{ at } r = R_o, \quad (\text{C.39})$$

$$\frac{\partial T_1}{\partial r} = 0 \text{ at } r = R_o, \quad (\text{C.40})$$

and, if considering an annular system,

$$v_{1r} = v_{1\theta} = v_{1z} = 0 \text{ at } r = R_i, \quad (\text{C.41})$$

$$\frac{\partial T_1}{\partial r} = 0 \text{ at } r = R_i. \quad (\text{C.42})$$

Now, the momentum equation (Equation C.32) will be rewritten as its component equations in the  $r$ ,  $\theta$ , and  $z$  directions. The  $\nabla$  operators will also be expanded in cylindrical coordinates. The components of the momentum equation are

$$\frac{L_z^2}{\nu \bar{t}} \frac{\partial v_{1r}}{\partial t} = -\frac{\partial p_1}{\partial r} + \left[ \left[ \frac{\partial^2}{\partial r^2} + \frac{1}{r} \frac{\partial}{\partial r} + \frac{1}{r^2} \frac{\partial^2}{\partial \theta^2} + \frac{\partial^2}{\partial z^2} - \frac{1}{r^2} \right] v_{1r} - \left[ \frac{2}{r^2} \frac{\partial}{\partial \theta} \right] v_{1\theta} \right], \quad (\text{C.43})$$

$$\frac{L_z^2}{\nu \bar{t}} \frac{\partial v_{1\theta}}{\partial t} = -\frac{1}{r} \frac{\partial p_1}{\partial \theta} + \left[ \left[ \frac{\partial^2}{\partial r^2} + \frac{1}{r} \frac{\partial}{\partial r} + \frac{1}{r^2} \frac{\partial^2}{\partial \theta^2} + \frac{\partial^2}{\partial z^2} - \frac{1}{r^2} \right] v_{1\theta} + \left[ \frac{2}{r^2} \frac{\partial}{\partial \theta} \right] v_{1r} \right], \quad (\text{C.44})$$

$$\frac{L_z^2}{\nu \bar{t}} \frac{\partial v_{1z}}{\partial t} = -\frac{\partial p_1}{\partial z} + \left[ \left[ \frac{\partial^2}{\partial r^2} + \frac{1}{r} \frac{\partial}{\partial r} + \frac{1}{r^2} \frac{\partial^2}{\partial \theta^2} + \frac{\partial^2}{\partial z^2} \right] v_{1z} \right] + \frac{\alpha L_z^2 g(\Delta T)}{\nu \bar{v}} T_1. \quad (\text{C.45})$$

#### C.4 Expansion into Normal Modes

The variables will now be expanded into modes. In the example expansion below, the new variable representing only the r-direction and z-direction dependencies is marked with a “prime” symbol. The exponential time dependence which each variable is assumed to possess is governed by an inverse time constant, called  $\sigma$ . The form of the expansion, considering, for example, the expansion of pressure, is

$$p_1 = p'_1(r, z) e^{im\theta + \sigma t}. \quad (\text{C.46})$$

At the onset of convection, the system is independent of time and the value of  $\sigma$  is 0. Thus, all time-derivative terms in the modeling equations may be eliminated once this expansion is applied. The final forms of the modeling equations for the case in which viscosity is considered constant with respect to temperature, with this expansion applied, and with the “prime” symbols dropped from the newly defined variables, are

$$0 = -\frac{\partial p_1}{\partial r} + \left[ \begin{array}{l} \left[ \frac{\partial^2}{\partial r^2} + \frac{1}{r} \frac{\partial}{\partial r} + \frac{\partial^2}{\partial z^2} - \frac{(m^2 + 1)}{r^2} \right] v_{1r} - \\ \left[ \frac{2im}{r^2} \right] v_{1\theta} \end{array} \right], \quad (\text{C.47})$$

$$0 = -\frac{im}{r} p_1 + \left[ \begin{array}{l} \left[ \frac{\partial^2}{\partial r^2} + \frac{1}{r} \frac{\partial}{\partial r} + \frac{\partial^2}{\partial z^2} - \frac{(m^2 + 1)}{r^2} \right] v_{1\theta} + \\ \left[ \frac{2im}{r^2} \right] v_{1r} \end{array} \right], \quad (\text{C.48})$$

$$0 = -\frac{\partial p_1}{\partial z} + \left[ \begin{array}{l} \left[ \frac{\partial^2}{\partial r^2} + \frac{1}{r} \frac{\partial}{\partial r} - \frac{m^2}{r^2} + \frac{\partial^2}{\partial z^2} \right] v_{1z} \end{array} \right] + \frac{\alpha L_z^2 g(\Delta T)}{\nu \bar{v}} T_1, \quad (\text{C.49})$$

$$0 = -\frac{L_z \bar{v}}{\kappa} \frac{\partial T_0}{\partial z} \bar{v}_1 + \left[ \frac{\partial^2}{\partial r^2} + \frac{1}{r} \frac{\partial}{\partial r} + \frac{\partial^2}{\partial z^2} - \frac{m^2}{r^2} \right] T_1, \quad (\text{C.50})$$

$$0 = \left[ \frac{\partial}{\partial r} + \frac{1}{r} \right] v_{1r} + \left[ \frac{im}{r} \right] v_{1\theta} + \left[ \frac{\partial}{\partial z} \right] v_{1z}, \quad (\text{C.51})$$

$$v_{1r} = v_{1\theta} = v_{1z} = 0 \text{ at } z = 0, \quad (\text{C.52})$$

$$T_1 = 0 \text{ at } z = 0, \quad (\text{C.53})$$

$$v_{1r} = v_{1\theta} = v_{1z} = 0 \text{ at } z = L_z, \quad (\text{C.54})$$

$$T_1 = 0 \text{ at } z = L_z, \quad (\text{C.55})$$

$$v_{1r} = v_{1\theta} = v_{1z} = 0 \text{ at } r = R_o, \quad (\text{C.56})$$

$$\frac{\partial T_1}{\partial r} = 0 \text{ at } r = R_o, \quad (\text{C.57})$$

and, if considering an annular system,

$$v_{1r} = v_{1\theta} = v_{1z} = 0 \text{ at } r = R_i, \quad (\text{C.58})$$

$$\frac{\partial T_1}{\partial r} = 0 \text{ at } r = R_i. \quad (\text{C.59})$$

This completes the presentation of the modeling equations for the case in which viscosity is considered constant with respect to temperature. These equations can be numerically solved on a computer as an eigenvalue problem, for the eigenvalue  $\Delta T$ , as explained in Chapter 5.

APPENDIX D  
MATLAB<sup>®</sup> PROGRAM GENERAL FLOW-DIAGRAM

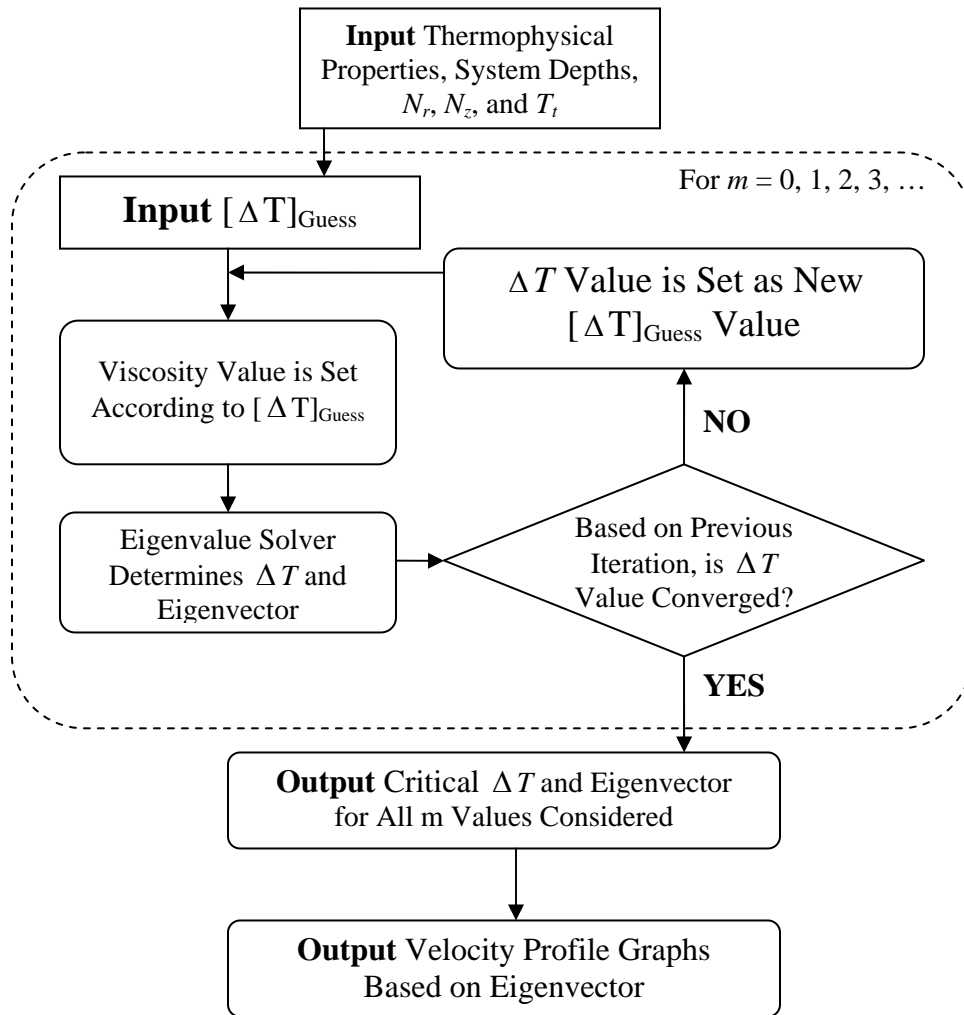


Figure D-1. MATLAB<sup>®</sup> program general flow-diagram.

## APPENDIX E EXAMPLE MATLAB<sup>®</sup> PROGRAMS

This appendix presents, in their full form, some examples of the MATLAB<sup>®</sup> programs used for calculations in this research. Note that the programming done in MATLAB<sup>®</sup> for this research was done with MATLAB<sup>®</sup> 7 (Version 7.0.4.365, R14, Service Pack 2). The main program used when solving for the critical vertical temperature difference and onset flow pattern for an annular system, including the variation of viscosity with temperature, is presented third. The first and second programs presented are simply files containing physical properties and depths, respectively, which are called upon by the main program.

### E.1 Physical Properties

```
% PHYSICAL PROPERTIES
% silicone oil

disp('The physical properties of silicone oil (lower phase) will now be used.')
```

## E.2 Depths for Annular System

```
% DEPTHS

disp('The dimensions being used.')

%Vertical Phase Depth
Lz=.00685292

%Inner Radius for Annulus
Rin=.0175006/2*.17

%Outer Radius for Annulus
Rout=.0175006/2

%Annular Gap Width
Lr=Rout-Rin

disp('Scaled depths:')

%Set characteristic length. Unlike what is done in the written development of the equations, here Lchar is
not simply replaced with Lz. The equations are left in a more general form, still containing "Lchar". The
particular value to be used for Lchar is set here.
Lchar=Lr
%Note, usually I have used Lr as Lchar even though Lz is usually used as Lchar in the written derivation

%Scaled values for Rin, Rout, Lz, and Lr
Rinscaled=Rin/Lchar
Routscaled=Rout/Lchar
Lzscaled=Lz/Lchar
Lrscaled=Lr/Lchar

%Actual span in non-spectral space of the r-direction and z-direction (spectral space spans from -1 to 1 in
r-direction and z-direction when considering annulus)

ro_leftboundary=Rin;
ro_rightboundary=Rout;

zo_lowerboundary=0;
zo_upperboundary=Lz;
```

## E.3 Main Program: Annular System with Temperature-Dependent Viscosity

```
clear all

m=[];
output_ann_usv=[];
output_ann_usv_crit=[];
warningsmatrix=[];
Smin_dataset=[];

%Calling on other files for physical properties and depths
propssiliconeoil35C_newoil
```

dannsiliconeoil

%In degrees Celsius:  
Tcold=30

%Singular value tolerances to later be used in removing spurious values. The tolerance choice is %kept at a fixed value (the value specified here) if desired. Also, a self-adjusting tolerance %can be set later. To choose a fixed tolerance, set tolchoice=1, and to choose an adjusting %tolerance, set tolchoice=2:  
tol1=1e-10;  
tolchoice=1;

%What happens if an eigenvalue in the result has a very large imaginary part?  
%LIRT = 1 - Stop Calculation, LIRT = 2 - Warning Only  
LIRT=1;

%The case for which it is desired to plot a velocity profile  
Nrforplot=13;  
Nzforplot=13;  
mforplot=3;

%Tolerance for convergence of critical temperature difference result with %respect to last iteration of viscosity's variation with temperature  
Tvcortol=1e-5

%Loops for N's  
for Nr=13  
for Nz=13

%Loop for m's  
for m=0:15

%Guess Value for deltaT  
deltaTguess=7.3531;  
%Set initial value for the indicator of the convergence of critical temperature difference result with %respect to last iteration of viscosity's variation with temperature (Tvcorr)  
Tvcorr=1;

%Loop for viscosity variation with respect to temperature  
while Tvcorr>=Tvcortol

%Information for scaling original r coordinates ("ro") to Chebyshev space ([-1:r:1])  
%Lr=xo\_upperboundary-xo\_lowerboundary;  
%rchebyshev ("r") as a function of ro, in the form  $r=rm*ro+rb$   
rmscaled=2/(Routscaled-Rinscaled);  
rm=2/(Rout-Rin);  
rb=-(Rin+Rout)/(Rout-Rin);  
%ro as a function of r=rchebyshev, in the form  $ro=rom*r+rob$   
rom=1/rm;  
rob=-rb/rm;  
%Chebyshev scale factors for differentiations of orders 1-2  
rcsf1=rmscaled; rcsf2=rmscaled^2;

%Generate grid points and differentiation matrix, r-direction

```

%(Gauss-Lobatto points)
if Nr==0, Dr=0; r=1; return, end
r=cos(pi*(0:Nr)/Nr)';
r=flipud(r);
c=[2; ones(Nr-1,1); 2].*(-1).^(0:Nr)';
R=repmat(r,1,Nr+1);
dR=R-R';
Dr=(c*(1./c')./(dR+(eye(Nr+1)))); %off-diagonal entries
Dr=sparse(Dr-diag(sum(Dr'))); %diagonal entries
Dr=rcof1*Dr; %Dr matrix with Chebyshev scaling factor included
Dr2=Dr^2;
ro=rom*r+rob;

%Information for scaling original z coordinates ("zo") to Chebyshev space ([-1:z:1])
%Lz=zo_upperboundary-zo_lowerboundary;
%zchebyshev ("z") as a function of zo, in the form z=zm*zo+zb
zmscaled=2/Lzscaled;
zm=2/Lz;
zb=1-zm*zo_upperboundary;
%zo as a function of z=zchebyshev, in the form zo=zom*z+zob
zom=1/zm;
zob=-zb/zm;
%Chebyshev scale factors for differentiations of orders 1-2
zcsf1=zmscaled; zcsf2=zmscaled^2;

%Generate grid points and differentiation matrix, z-direction
if Nz==0, Dz=0; z=1; return, end
z=cos(pi*(0:Nz)/Nz)';
z=flipud(z);
c=[2; ones(Nz-1,1); 2].*(-1).^(0:Nz)';
Z=repmat(z,1,Nz+1);
dZ=Z-Z';
Dz=(c*(1./c')./(dZ+(eye(Nz+1)))); %off-diagonal entries
Dz=sparse(Dz-diag(sum(Dz'))); %diagonal entries
Dz=zcof1*Dz; %Dz matrix with Chebyshev scaling factor included
Dz2=Dz^2;
zo=zom*z+zob;
zoscaled=zo./Lchar;

%Setting Thot based on Tcold and deltaTguess
Thot=Tcold+deltaTguess;

%Determining the original (pre-onset) temperature profile in the system in the z-direction
T0_zdir=(Thot-Tcold)/(Lz)*zo+Tcold;

%Variation of viscosity with temperature for silicone oil
vfluid='silicone oil';
%Viscosity-Temperature curve determined by my measurements with a viscometer
A0visc=.147105008294588;
B0visc=-.0179753249042257;
Bvisc=B0visc;
%The viscosity at each location along the z-direction (prior to onset) in exponential form
vv=A0visc*exp(B0visc*T0_zdir);
%Finding the reference viscosity and reference temperature
tempviscmat=[T0_zdir,vv];

```

```

viscmean=mean(tempviscmat(:,2));
viscref=viscmean;
%Now I will use viscref and any pair of vv(j), T0_zdir(j) to solve for Tref
Tref=log(viscref/vv(1))/(B0visc)+T0_zdir(1);
%Scaled vector of base state temperatures (prior to onset) along the z-direction
T0_zdir_scaled=(T0_zdir-Tref)/(deltaTguess);
%To be consistent with the [-1:z:1] and [0:zo:Lz] (zo is z_original, which is z in original %coordinates)
arrangement, I %should have the temperature and viscosity values corresponding %to z=Lz at the bottom
of the viscosity vectors/matrices and those corresponding to z=0 at the %top.
T0_zdir_scaled=flipud(T0_zdir_scaled);
%Convert to matrix form for use later
T0_zdir_scaled_full=kron(T0_zdir_scaled,ones(Nr+1,1));

%Top temperature, bottom temperature, and dT/dz in terms of scaled lengths:
Tbottomscaled=(Thot-Tref)/(Thot-Tcold);
Ttopscaled=(Tcold-Tref)/(Thot-Tcold);
dT0dz=(Ttopscaled-Tbottomscaled)/Lzscaled;
%Reference kinematic viscosity
kvref=viscref/dens;
%Characteristic velocity (m/s) and characteristic time (s):
props=[kvref td];
depths=[Lr Lz];
vchar=min(props)/max(depths);
tchar=(max(depths))^2/min(props)
%Gravity in m/s^2:
g=9.807;

%Domain Equations

%All variables shown in the following matrices are 1st order in epsilon
%unless indicated as being base state variables by subscript "0"

%Construct matrix operator, LHS (left-hand-side). Excluding boundary conditions.

%Creating combination matrices including the reciprocal factors of r for use in the cylindrical %coordinate
system equations
roscaled=ro./Lchar;
Dr2comb1=[]; eyercomb1=[]; eyercomb2=[];
eyematr=speye(Nr+1);
for kk=1:(Nr+1), p=roscaled.^(-1); p2=roscaled.^(-2); Dr2comb1(kk,:)=Dr2(kk,:)+p(kk)*Dr(kk,:);
eyercomb1(kk,:)=p2(kk)*eyematr(kk,:); eyercomb2(kk,:)=p(kk)*eyematr(kk,:); end

%NOTE ABOUT BC's: so, the way I have z set up, z=-1 is at the bottom (zo=0)
%and z=1 is at the top (zo=Lz)

%Motion r-dir
%Rows will later be cut out of this matrix for the following BCs:
%vr(r=Rin)=0,vr(r=Rout)=0,vr(z=0)=0,vr(z=Lz)=0

expterm=exp(Bvisc*deltaTguess*T0_zdir_scaled_full);

%The coefficient of vr in the motion equation's r-direction-component
motr_vr=[(kron(speye(Nz+1),Dr2comb1)+kron(Dz2,speye(Nr+1))-
((m^2+1)*kron(speye(Nz+1),eyercomb1)))+Bvisc*deltaTguess*dT0dz*kron(Dz,speye(Nr+1))];

```

```

for j=1:size(motr_vr,1), motr_vr(j,:)=motr_vr(j,:)*exp term(j);end
%The coefficient of vtheta in the motion equation's r-direction-component
motr_vtheta=[(-2*i*m*kron(speye(Nz+1),eyercomb1))];
for j=1:size(motr_vtheta), motr_vtheta(j,:)=motr_vtheta(j,:)*exp term(j);end
%The coefficient of vz in the motion equation's r-direction-component
motr_vz=[Bvisc*deltaTguess*dT0dz*kron(speye(Nz+1),Dr)];
for j=1:size(motr_vz), motr_vz(j,:)=motr_vz(j,:)*exp term(j);end
%The coefficient of T in the motion equation's r-direction-component
motr_T=[sparse((Nr+1)*(Nz+1),(Nr+1)*(Nz+1))];
%The coefficient of P in the motion equation's r-direction-component
motr_P=[-kron(speye(Nz+1),Dr)];

%Motion theta-dir
%Rows will later be cut out of this matrix for the following BCs:
%vtheta(r=Rin)=0,vtheta(r=Rout)=0,vtheta(z=0)=0,vtheta(z=Lz)=0

mottheta_vr=[(2*i*m*kron(speye(Nz+1),eyercomb1))];
for j=1:size(mottheta_vr), mottheta_vr(j,:)=mottheta_vr(j,:)*exp term(j);end
mottheta_vtheta=[(kron(speye(Nz+1),Dr2comb1)+kron(Dz2,speye(Nr+1))-
((m^2+1)*kron(speye(Nz+1),eyercomb1)))+Bvisc*deltaTguess*dT0dz*kron(Dz,speye(Nr+1))];
for j=1:size(mottheta_vtheta), mottheta_vtheta(j,:)=mottheta_vtheta(j,:)*exp term(j);end
mottheta_vz=[Bvisc*deltaTguess*dT0dz*i*m*kron(speye(Nz+1),eyercomb2)];
for j=1:size(mottheta_vz), mottheta_vz(j,:)=mottheta_vz(j,:)*exp term(j);end
mottheta_T=[sparse((Nr+1)*(Nz+1),(Nr+1)*(Nz+1))];
mottheta_P=[-i*m*kron(speye(Nz+1),eyercomb2)];

%Motion z-dir
%Rows will later be cut out of this matrix for the following BCs:
%vz(r=Rin)=0,vz(r=Rout)=0,vz(z=0)=0,vz(z=Lz)=0
motz_vr=[sparse((Nr+1)*(Nz+1),(Nr+1)*(Nz+1))];
motz_vtheta=[sparse((Nr+1)*(Nz+1),(Nr+1)*(Nz+1))];
motz_vz=[(kron(speye(Nz+1),Dr2comb1)+kron(Dz2,speye(Nr+1))-
(m^2*kron(speye(Nz+1),eyercomb1)))+Bvisc*deltaTguess*dT0dz*2*kron(Dz,speye(Nr+1))];
for j=1:size(motz_vz), motz_vz(j,:)=motz_vz(j,:)*exp term(j);end
motz_T=[sparse((Nr+1)*(Nz+1),(Nr+1)*(Nz+1))];
motz_P=[-kron(Dz,speye(Nr+1))];
motz=[motz_vr,motz_vtheta,motz_vz,motz_T,motz_P];

%Energy
%Rows will later be cut out of this matrix for the following BCs:
%dT/dr(r=Rin)=0,dT/dr(r=Rout)=0,T(z=0)=0,T(z=Lz)=0
ener_vr=[sparse((Nr+1)*(Nz+1),(Nr+1)*(Nz+1))];
ener_vtheta=[sparse((Nr+1)*(Nz+1),(Nr+1)*(Nz+1))];
ener_vz=[-Lchar*vchar/td*dT0dz*kron(speye(Nz+1),speye(Nr+1))];
ener_T=[kron(speye(Nz+1),Dr2comb1)+kron(Dz2,speye(Nr+1))-(m^2*kron(speye(Nz+1),eyercomb1))];
ener_P=[sparse((Nr+1)*(Nz+1),(Nr+1)*(Nz+1))];

%Continuity
cont_vr=[kron(speye(Nz+1),Dr)+kron(speye(Nz+1),eyercomb2)];
cont_vtheta=[i*m*kron(speye(Nz+1),eyercomb2)];
cont_vz=[kron(Dz,speye(Nr+1))];
cont_T=[sparse((Nr+1)*(Nz+1),(Nr+1)*(Nz+1))];
cont_P=[sparse((Nr+1)*(Nz+1),(Nr+1)*(Nz+1))];

%Boundary Conditions

```

```

%BC1: vr(r=Rin)=0
preBC1=[sparse(1,Nr),1];
BC1=[sparse((Nz-1),Nr+1),kron(speye(Nz-1),preBC1),sparse((Nz-1),(Nr+1)),sparse((Nz-1),4*(Nr+1)*(Nz+1)));

%BC2: vr(r=Rout)=0
preBC2=[1,sparse(1,Nr)];
BC2=[sparse((Nz-1),Nr+1),kron(speye(Nz-1),preBC2),sparse((Nz-1),(Nr+1)),sparse((Nz-1),4*(Nr+1)*(Nz+1)));

%BC3: vr(z=0)=0
BC3=[speye(Nr+1),sparse(Nr+1,(Nz)*(Nr+1)),sparse(Nr+1,4*(Nr+1)*(Nz+1)));

%BC4: vr(z=Lz)=0
BC4=[sparse(Nr+1,(Nz)*(Nr+1)),speye(Nr+1),sparse(Nr+1,4*(Nr+1)*(Nz+1)));

%BC5: vtheta(r=Rin)=0
BC5=[sparse((Nz-1),(Nr+1)*(Nz+1)),sparse((Nz-1),Nr+1),kron(speye(Nz-1),preBC1),sparse((Nz-1),(Nr+1)),sparse((Nz-1),3*(Nr+1)*(Nz+1)));

%BC6: vtheta(r=Rout)=0
BC6=[sparse((Nz-1),(Nr+1)*(Nz+1)),sparse((Nz-1),Nr+1),kron(speye(Nz-1),preBC2),sparse((Nz-1),(Nr+1)),sparse((Nz-1),3*(Nr+1)*(Nz+1)));

%BC7: vtheta(z=0)=0
BC7=[sparse(Nr+1,(Nr+1)*(Nz+1)),speye(Nr+1),sparse(Nr+1,(Nz)*(Nr+1)),sparse(Nr+1,3*(Nr+1)*(Nz+1)));

%BC8: vtheta(z=Lz)=0
BC8=[sparse(Nr+1,(Nr+1)*(Nz+1)),sparse(Nr+1,(Nz)*(Nr+1)),speye(Nr+1),sparse(Nr+1,3*(Nr+1)*(Nz+1)));

%BC9: vz(r=Rin)=0
BC9=[sparse((Nz-1),2*(Nr+1)*(Nz+1)),sparse((Nz-1),Nr+1),kron(speye(Nz-1),preBC1),sparse((Nz-1),(Nr+1)),sparse((Nz-1),2*(Nr+1)*(Nz+1)));

%BC10: vz(r=Rout)=0
BC10=[sparse((Nz-1),2*(Nr+1)*(Nz+1)),sparse((Nz-1),Nr+1),kron(speye(Nz-1),preBC2),sparse((Nz-1),(Nr+1)),sparse((Nz-1),2*(Nr+1)*(Nz+1)));

%BC11: vz(z=0)=0
BC11=[sparse(Nr+1,2*(Nr+1)*(Nz+1)),speye(Nr+1),sparse(Nr+1,(Nz)*(Nr+1)),sparse(Nr+1,2*(Nr+1)*(Nz+1)));

%BC12: vz(z=Lz)=0
BC12=[sparse(Nr+1,2*(Nr+1)*(Nz+1)),sparse(Nr+1,(Nz)*(Nr+1)),speye(Nr+1),sparse(Nr+1,2*(Nr+1)*(Nz+1)));

%BC13: dT/dr(r=Rin)=0
preBC13=[Dr(Nr+1,:);
BC13=[sparse((Nz-1),3*(Nr+1)*(Nz+1)),sparse((Nz-1),(Nr+1)),kron(speye(Nz-1),preBC13),sparse((Nz-1),(Nr+1)),sparse((Nz-1),(Nr+1)*(Nz+1)));

%BC14: dT/dr(r=Rout)=0

```

```

preBC14=[Dr(1,:);
BC14=[sparse((Nz-1),3*(Nr+1)*(Nz+1)),sparse((Nz-1),(Nr+1)),kron(speye(Nz-1),preBC14),sparse((Nz-1),(Nr+1)),sparse((Nz-1),(Nr+1)*(Nz+1))];

%BC15: T(z=0)=0
BC15=[sparse(Nr+1,3*(Nr+1)*(Nz+1)),speye(Nr+1),sparse(Nr+1,(Nr+1)*(Nz)),sparse(Nr+1,(Nr+1)*(Nz+1))];

%BC16: T(z=Lz)=0
BC16=[sparse(Nr+1,3*(Nr+1)*(Nz+1)),sparse(Nr+1,(Nr+1)*(Nz)),speye(Nr+1),sparse(Nr+1,(Nr+1)*(Nz+1))];

%Now I will enforce the boundary conditions in each equation by replacing rows in the domain %equation matrices:

%motr: vr(r=Rin)=0,vr(r=Rout)=0,vr(z=0)=0,vr(z=Lz)=0
motr(1:(Nr+1),:)=BC3;
motr((Nr+1)*(Nz+1)-(Nr+1)+1:(Nr+1)*(Nz+1),:)=BC4;
jj=0; iii=[];
for ii=((Nr+1)+1):(Nr+1):((Nr+1)*(Nz+1)-2*(Nr+1)+1)
    iii=ii+Nr;
    jj=jj+1;
    motr(ii,:)=BC1(jj,:);
    motr(iii,:)=BC2(jj,:);
end

%mottheta: vtheta(r=Rin)=0,vtheta(r=Rout)=0,vtheta(z=0)=0,vtheta(z=Lz)=0
mottheta(1:(Nr+1),:)=BC7;
mottheta((Nr+1)*(Nz+1)-(Nr+1)+1:(Nr+1)*(Nz+1),:)=BC8;
jj=0; iii=[];
for ii=((Nr+1)+1):(Nr+1):((Nr+1)*(Nz+1)-2*(Nr+1)+1)
    iii=ii+Nr;
    jj=jj+1;
    mottheta(ii,:)=BC5(jj,:);
    mottheta(iii,:)=BC6(jj,:);
end

%motz: vz(r=Rin)=0,vz(r=Rout)=0,vz(z=0)=0,vz(z=Lz)=0
motz(1:(Nr+1),:)=BC11;
motz((Nr+1)*(Nz+1)-(Nr+1)+1:(Nr+1)*(Nz+1),:)=BC12;
jj=0; iii=[];
for ii=((Nr+1)+1):(Nr+1):((Nr+1)*(Nz+1)-2*(Nr+1)+1)
    iii=ii+Nr;
    jj=jj+1;
    motz(ii,:)=BC9(jj,:);
    motz(iii,:)=BC10(jj,:);
end

%ener: dT/dr(r=Rin)=0,dT/dr(r=Rout)=0,T(z=0)=0,T(z=Lz)=0
ener(1:(Nr+1),:)=BC15;
ener((Nr+1)*(Nz+1)-(Nr+1)+1:(Nr+1)*(Nz+1),:)=BC16;
jj=0; iii=[];
for ii=((Nr+1)+1):(Nr+1):((Nr+1)*(Nz+1)-2*(Nr+1)+1)
    iii=ii+Nr;
    jj=jj+1;

```

```

ener(ii,:)=BC13(jj,:);
ener(iii,:)=BC14(jj,:);
end

%Final form of LHS matrix
LHS=[motr;mottheta;motz;ener;cont];

%Form RHS (right-hand-side) matrix
motrRHS=[sparse((Nr+1)*(Nz+1),5*(Nr+1)*(Nz+1))];
motthetaRHS=[sparse((Nr+1)*(Nz+1),5*(Nr+1)*(Nz+1))];
motzRHS=[sparse((Nr+1)*(Nz+1),3*(Nr+1)*(Nz+1)),
((tec*g*Lchar^2)/(kvref*vchar))*kron(speye(Nz+1),speye(Nr+1)),sparse((Nr+1)*(Nz+1),(Nr+1)*(Nz+1))];
enerRHS=[sparse((Nr+1)*(Nz+1),5*(Nr+1)*(Nz+1))];
contRHS=[sparse((Nr+1)*(Nz+1),5*(Nr+1)*(Nz+1))];

%Now I will enforce the boundary conditions in each equation in the RHS:

%motr: vr(r=Rin)=0,vr(r=Rout)=0,vr(z=0)=0,vr(z=Lz)=0
motrRHS(1:(Nr+1),:)=sparse(Nr+1,5*(Nr+1)*(Nz+1));
motrRHS((Nr+1)*(Nz+1)-(Nr+1)+1:(Nr+1)*(Nz+1),:)=sparse(Nr+1,5*(Nr+1)*(Nz+1));
jj=0; iii=[];
for ii=((Nr+1)+1):(Nr+1):((Nr+1)*(Nz+1)-2*(Nr+1)+1)
    iii=ii+Nr;
    jj=jj+1;
    motrRHS(ii,:)=sparse(1,5*(Nr+1)*(Nz+1));
    motrRHS(iii,:)=sparse(1,5*(Nr+1)*(Nz+1));
end

%mottheta: vtheta(r=Rin)=0,vtheta(r=Rout)=0,vtheta(z=0)=0,vtheta(z=Lz)=0
motthetaRHS(1:(Nr+1),:)=sparse(Nr+1,5*(Nr+1)*(Nz+1));
motthetaRHS((Nr+1)*(Nz+1)-(Nr+1)+1:(Nr+1)*(Nz+1),:)=sparse(Nr+1,5*(Nr+1)*(Nz+1));
jj=0; iii=[];
for ii=((Nr+1)+1):(Nr+1):((Nr+1)*(Nz+1)-2*(Nr+1)+1)
    iii=ii+Nr;
    jj=jj+1;
    motthetaRHS(ii,:)=sparse(1,5*(Nr+1)*(Nz+1));
    motthetaRHS(iii,:)=sparse(1,5*(Nr+1)*(Nz+1));
end

%motz: vz(r=Rin)=0,vz(r=Rout)=0,vz(z=0)=0,vz(z=Lz)=0
motzRHS(1:(Nr+1),:)=sparse(Nr+1,5*(Nr+1)*(Nz+1));
motzRHS((Nr+1)*(Nz+1)-(Nr+1)+1:(Nr+1)*(Nz+1),:)=sparse(Nr+1,5*(Nr+1)*(Nz+1));
jj=0; iii=[];
for ii=((Nr+1)+1):(Nr+1):((Nr+1)*(Nz+1)-2*(Nr+1)+1)
    iii=ii+Nr;
    jj=jj+1;
    motzRHS(ii,:)=sparse(1,5*(Nr+1)*(Nz+1));
    motzRHS(iii,:)=sparse(1,5*(Nr+1)*(Nz+1));
end

%ener: dT/dr(r=Rin)=0,dT/dr(r=Rout)=0,T(z=0)=0,T(z=Lz)=0
enerRHS(1:(Nr+1),:)=sparse(Nr+1,5*(Nr+1)*(Nz+1));
enerRHS((Nr+1)*(Nz+1)-(Nr+1)+1:(Nr+1)*(Nz+1),:)=sparse(Nr+1,5*(Nr+1)*(Nz+1));
jj=0; iii=[];

```

```

for ii=((Nr+1)+1):(Nr+1):((Nr+1)*(Nz+1)-2*(Nr+1)+1)
    iii=ii+Nr;
    jj=jj+1;
    enerRHS(ii,:)=sparse(1,5*(Nr+1)*(Nz+1));
    enerRHS(iii,:)=sparse(1,5*(Nr+1)*(Nz+1));
end

%Final form of RHS matrix
RHS=[motrRHS;motthetaRHS;motzRHS;enerRHS;contRHS];

%Use singular value decomposition on LHS matrix to make it easier to work with/deal with %spurious
values
U=[]; S=[]; V=[];
[U,S,V]=svd(full(LHS));
Ssort=sort(diag(S));

%Examining and sorting singular values
for ii=1 : ((Nr+1)*(Nz+1)*5)
if abs(imag(Ssort(ii))) >= 1e-9, disp('Error: Large imaginary part in singular value'), return, else, end
end
Smin=Ssort(1:20);
Smin_dataset=[Smin_dataset;Nr;Nz;m;Smin];
save S.mat S; save U.mat U; save V.mat V; save Smin.mat Smin

%Eigenvalue calculation, taking into account the singular value tolerance specified earlier

%Inverting the singular values, but filtering out those singular values which are smaller than the %singular
value tolerance specified earlier.
Sinv1=[];
if tolchoice==1;
for ii=1 : ((Nr+1)*(Nz+1)*5)
if abs(real(S(ii,ii))) <= tol1 ;Sinv1(ii,ii) = 0;
else, Sinv1(ii,ii) = 1/S(ii,ii);end,end,else,end
if tolchoice==2;
for ii=1 : ((Nr+1)*(Nz+1)*5)
if abs(real(S(ii,ii))) <= tolmod ;Sinv1(ii,ii) = 0;
else, Sinv1(ii,ii) = 1/S(ii,ii);end,end,else,end

%Creating modified RHS matrix by multiplying by the inverse of matrices created in the singular value
decomposition of the LHS matrix
RHSmod1=Sinv1*inv(U)*full(RHS);

%Solving the original generalized eigenvalue problem using matrices created and modified according to
the singular value decomposition of the original LHS matrix
[result1evec,result1]=eig(V',RHSmod1);
result1=diag(result1);

%"result1" are the eigenvalues. The following section examines them.
result1real=real(result1);
result1posrealmod=[];
jj=0; %%
%Setting non-positive eigenvalues equal to infinity so that they are not considered when sorting %the
eigenvalues
for kk=1:length(result1); %%
if result1real(kk)<=0; result1posrealmod(kk)=inf; else result1posrealmod(kk)=result1real(kk); end, end

```

```

%Sorting the eigenvalues and finding the critical eigenvalue
[sortresult1mod,sortresult1modindex]=sort(result1posrealmod);
locrcrit=sortresult1modindex(1);

%Obtaining the eigenvector which corresponds to the critical eigenvalue
result1eveccrit=result1evec(:,locrcrit);

%Obtaining the vr, vtheta, vz, and T portions of the critical eigenvector
vr=result1eveccrit(1:((Nr+1)*(Nz+1)));
vtheta=result1eveccrit((Nr+1)*(Nz+1)+1:(2*(Nr+1)*(Nz+1)));
vz=result1eveccrit(2*(Nr+1)*(Nz+1)+1:(3*(Nr+1)*(Nz+1)));
T=result1eveccrit(3*(Nr+1)*(Nz+1)+1:(4*(Nr+1)*(Nz+1)));

%Renaming the critical value
resultmin1=sortresult1mod(1);
deltaTcrit=resultmin1;

%Creating a compact and clear display of the output of the calculation with its corresponding %input
parameters
output_ann_usv=[output_ann_usv; [m Nr Nz deltaTguess deltaTcrit]];
[m Nr Nz deltaTguess deltaTcrit]

%Indicator of the convergence of critical temperature difference result with
%respect to last iteration of viscosity's variation with temperature
Tvcorr=abs((deltaTcrit-deltaTguess)/deltaTguess)

%Setting the new value of deltaTguess for iteration
deltaTguess=deltaTcrit;

%For use in possible text displays
Nrstring=num2str(Nr);
Nzstring=num2str(Nz);
mstring=num2str(m);
deltaTstring=num2str(deltaTcrit);

%If the critical temperature difference value is converged with respect to changes in viscosity due to its
temperature-dependence:
if Tvcorr<Tvcortol,

%Procedure to be executed in the event that the critical temperature difference calculated has a %large
imaginary part
if LIRT==1,
if abs(imag(resultmin1))>=1e-7, disp('Error: Large imaginary part in critical value. '), return, else, %%
else, end
if LIRT==2,
if abs(imag(resultmin1))>=1e-7, warningstr=['Large imaginary part in critical value: Nr=',Nrstring,',
Nz=',Nzstring,', m=',mstring,', deltaT=',deltaTstring,' filler: ']; strszedeficiency=90-size(warningstr,2);
filler=zeros(1,strszedeficiency); warningstr=[warningstr,filler],
warningsmatrix=[warningsmatrix;warningstr]; else, end,%%
else, end

%Output display including all outputs calculated for each input m, Nr, Nz
output_ann_usv_crit=[output_ann_usv_crit; [m Nr Nz deltaTcrit]];
output_ann_usv_crit

%If this is the case for which it is desired to plot a velocity profile, then the following procedure begins

```

```

if Nr==Nrforplot & Nz==Nzforplot & m==mforplot,

theta=[0:2*pi/64:2*pi]';
halfNz=round((Nz+1)/2);
rgrid=[kron(ones(Nz+1,1),kron(ro',ones(1,length(theta))))];
thetagrid=[kron(ones(Nz+1,1),kron(ones(1,length(r)),theta'))];
zgrid=[kron(z0,ones(1,(Nr+1)*length(theta)))];
xcartgrid=[]; ycartgrid=[]; zcartgrid=[];
for j=1:(Nz+1)
    for k=1:((Nr+1)*length(theta))
xcartgrid(j,k)=rgrid(j,k)*cos(thetagrid(j,k));
ycartgrid(j,k)=rgrid(j,k)*sin(thetagrid(j,k));
zcartgrid(j,k)=zgrid(j,k);
    end
end

vrfull=2*real(kron(vr,exp(i*m*theta)));
vthetafull=2*real(kron(vtheta,exp(i*m*theta)));
vzfull=2*real(kron(vz,exp(i*m*theta)));
Tfull=2*real(kron(T,exp(i*m*theta)));

vrmatrix=reshape(vrfull,(Nr+1)*length(theta),Nz+1)';
vthetamatrix=reshape(vthetafull, (Nr+1)*length(theta),Nz+1)';
vzmatrix=reshape(vzfull,(Nr+1)*length(theta),Nz+1)';
Tmatrix=reshape(Tfull,(Nr+1)*length(theta),Nz+1)';

vxcartmatrix=[]; vycartmatrix=[]; vzcartmatrix=[]; Tcartmatrix=[];
for j=1:(Nz+1)
    for k=1:((Nr+1)*length(theta))
vxcartmatrix(j,k)=vrmatrix(j,k)*cos(thetagrid(j,k))-vthetamatrix(j,k)*sin(thetagrid(j,k));
vycartmatrix(j,k)=vrmatrix(j,k)*sin(thetagrid(j,k))+vthetamatrix(j,k)*cos(thetagrid(j,k));
vzcartmatrix(j,k)=vzmatrix(j,k);
Tcartmatrix(j,k)=Tmatrix(j,k);
    end
end

%Three-dimensional plot of velocity vectors
quiver3(xcartgrid,ycartgrid,zcartgrid,vxcartmatrix,vycartmatrix,vzcartmatrix)
title(['Velocity Profile, at deltaTcrit= ',deltaTstring,' degrees C'])
xlabel('x')
ylabel('y')
zlabel('z')
rotate3d on

%Two-dimensional plot of cross-section of velocity profile (this graph is generally the most %helpful)
vzcrosssection=vzmatrix(halfNz,:);
Tcrosssection=Tmatrix(halfNz,:);
vzcrosssectionmatrix=reshape(vzcrosssection,length(theta),Nr+1)';
Tcrosssectionmatrix=reshape(Tcrosssection,length(theta),Nr+1)';
xcartgridcrosssectionmatrix=[]; ycartgridcrosssetionmatrix=[];
xcartgridcrosssection=xcartgrid(halfNz,:);
ycartgridcrosssection=ycartgrid(halfNz,:);
xcartgridcrosssectionmatrix=reshape(xcartgridcrosssection,length(theta),Nr+1)';
ycartgridcrosssectionmatrix=reshape(ycartgridcrosssection,length(theta),Nr+1)';
figure

```

```
contourf(xcartgridcrosssectionmatrix,ycartgridcrosssectionmatrix,vzcrosssectionmatrix)
colorbar('southoutside')
```

```
%NOTE: The velocities determined and plotted up to this point are dimensionless.
```

```
%To recover the dimensional, unscaled velocity values, must simply
```

```
%multiply scaled velocity results by the characteristic velocity, vchar.
```

```
%This will simply change the magnitudes of the velocity values, but the
```

```
%flow pattern will, of course, be the same. The unscaled velocities could
```

```
%be plotted in exactly the same way that the scaled values are.
```

```
vmatrix_unscaled=vmatrix.*vchar;
```

```
vthetamatrix_unscaled=vthetamatrix.*vchar;
```

```
vzmatrix_unscaled=vzmatrix.*vchar;
```

```
vxcartmatrix_unscaled=vxcartmatrix.*vchar;
```

```
vycartmatrix_unscaled=vycartmatrix.*vchar;
```

```
vzcartmatrix_unscaled=vzcartmatrix.*vchar;
```

```
vzcrosssectionmatrix_unscaled=vzcrosssectionmatrix.*vchar;
```

```
%Ending of if loops
```

```
else, end, else, end
```

```
%Ending of while loop for viscosity variation
```

```
end
```

```
%Ending of m loop
```

```
end
```

```
%Ending of Nz loop
```

```
end
```

```
%Ending of Nr loop
```

```
end
```

```
%Final output display
```

```
output_ann_usv_crit
```

```
warningsmatrix
```

APPENDIX F  
LabVIEW™ PROGRAM GENERAL FLOW-DIAGRAM

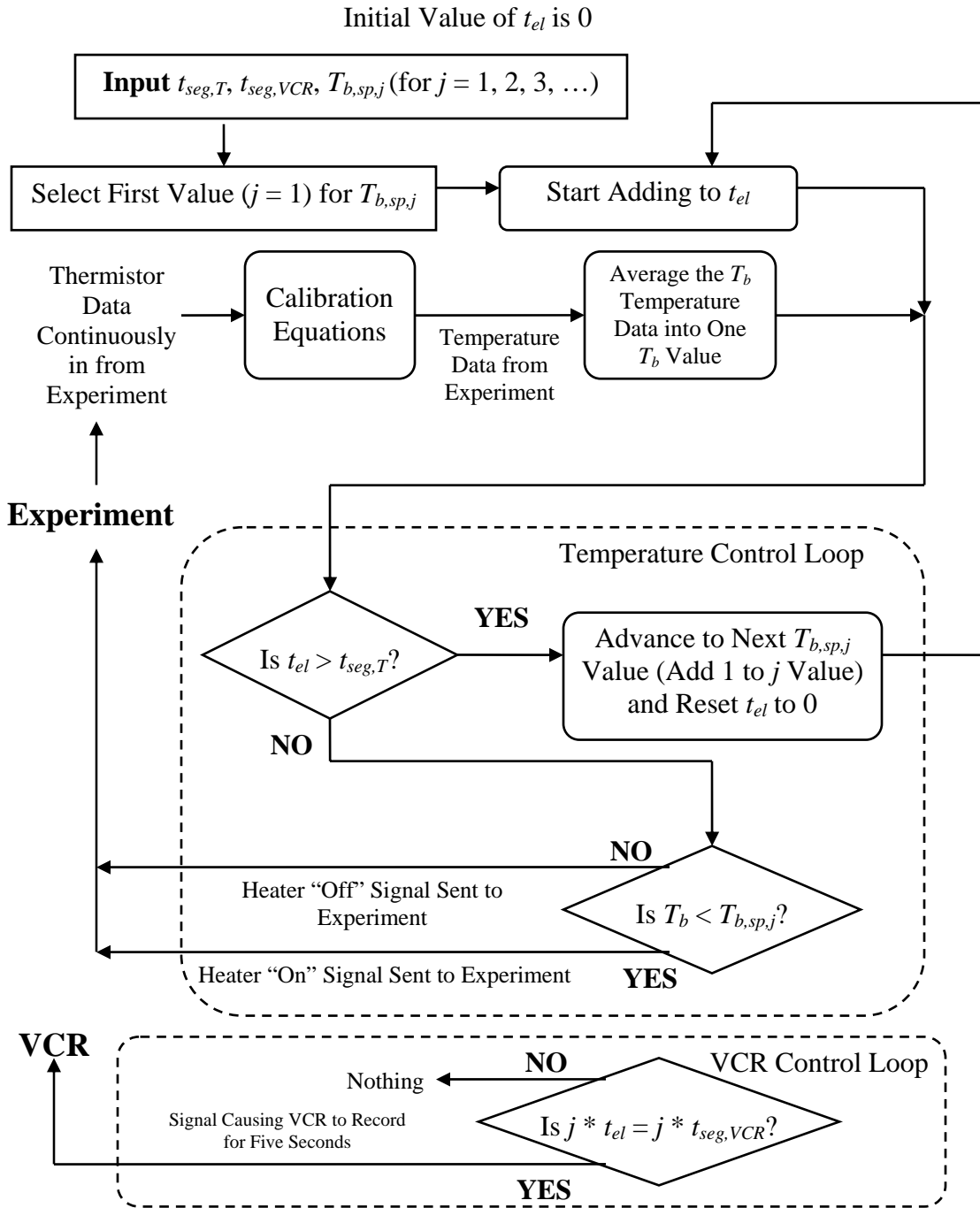


Figure F-1. LabVIEW™ program general flow-diagram.

## REFERENCES

- BÉNARD, H. 1900 *Rev. Gen. Sci. Pure Appl.* **11**, 1261, 1309.
- BENSIMON, D. 1988 *Physical Review A* **37** (1), 200.
- BLOCK, M. J. 1956 *Nature* (London) **178**, 650.
- CHANDRASEKHAR, S. 1961 *Hydrodynamic and Hydromagnetic Stability* Dover Publications, Inc., New York.
- CHARLSON, G. S., & SANI, R. L. 1970 *Int. J. Heat and Mass Transfer* **13**, 1479.
- CHARLSON, G. S., & SANI, R. L. 1971 *Int. J. Heat and Mass Transfer* **14**, 2157.
- CILIBERTO, S., BAGNOLI, F., & CAPONERI, M. 1990 *Il Nuovo Cimento* **12 D** (N. 6), 781.
- DAUBY, P. C., & LEBON, G. 1996 *J. Fluid Mech.* **329**, 25.
- DAVIS, S. H. 1967 *J. Fluid Mech.* **30** (part 3), 465.
- FERM, E. N., & WOLLKIND, D. J. 1982 *J. Non-Equilib. Thermodyn.* **7**, 169.
- HARDIN, G. R., SANI, R. L., HENRY, D., & ROUX, B. 1990 *International J. Num. Methods in Fluids* **10**, 79.
- JOHNS, L. E., & NARAYANAN, R. 2002 *Interfacial Instability* Springer, New York.
- JOHNSON, D. 1997 Geometric Effects on Bilayer Convection in Cylindrical Containers. Ph.D. Dissertation, University of Florida, Gainesville, Florida.
- JOHNSON, D., & NARAYANAN, R. 1999 *CHAOS* **9**, 124.
- KATS-DEMYANETS, V., ORON, A., & NEPOMNYASHCHY, A. A. 1997 *European Journal of Mechanics, B/Fluids* **16**, No. 1, 49.
- KOSCHMIEDER, E. L. 1967 *J. Fluid Mech.* **30** (part 1), 9.
- KOSCHMIEDER, E. L., & PALLAS, S. G. 1974 *Int. J. Heat and Mass Transfer* **17**, 991.
- KOSCHMIEDER, E. L., & PRAHL, S. A. 1990 *J. Fluid Mech.* **215**, 571.
- KOSCHMIEDER, E. L., & SWITZER, D. W. 1992 *J. Fluid Mech.* **240**, 533.
- LABROSSE, G. 1993 *Computer Methods in Applied Mechanics and Engineering* **106**, 353.

- LITTLEFIELD, D. L., & DESAI, P. V. 1990 *J. Heat Transfer* **112**, 959.
- PEARSON, J. R. A. 1958 *J. Fluid Mech.* **4**, 489.
- RAYLEIGH, LORD 1916 *Phil. Mag.* **52**, 529.
- SCHMIDT, R. J., & MILVERTON, S. W. 1935 *Proc. Roy. Soc. (London) A* **152**, 586.
- SCRIVEN, L. E., & STERNLING, C. V. 1964 *J. Fluid Mech.* **19**, 321.
- SILVESTON, P. L. 1958 *Forsch. Ing. Wes.* **24**, 29, 59.
- STERNLING, C. V., & SCRIVEN, L. E. 1959 *A.I.Ch.E. Journal* **5** (4), 514.
- STORK, K., & MÜLLER, U. 1972 *J. Fluid Mech.* **54** (part 4), 599.
- STORK, K., & MÜLLER, U. 1974 *J. Fluid Mech.*, **71**, 231.
- TREFETHEN, L. N. 2000 *Spectral Methods in MATLAB* S.I.A.M., Philadelphia.
- ZEREN, R. W., & REYNOLDS, W. C. 1972 *J. Fluid Mech.* **53**, 305.
- ZHAO, A. X., MOATES, F. C., & NARAYANAN, R. 1995 *Phys. Fluids* **7** (7), 1576.
- ZHAO, A. X., WAGNER, C., NARAYANAN, R., & FRIEDRICH, R. 1995 *Proceedings: Mathematical and Physical Sciences* **451**, No. 1942, 487.

## BIOGRAPHICAL SKETCH

The author was born on August 28, 1980 at Langley Air Force Base in Virginia. He received a B.S. in chemical engineering at Louisiana Tech University in 2002. After this, he attended the University of Florida from 2002 to 2006 to earn a Ph.D. in chemical engineering. During his time in graduate school, he was awarded a fellowship by N.A.S.A. through the Graduate Student Researchers Program.